Applications of MXenes in human-like sensors and actuators

Jinbo Pang[1,§] (✉), Songang Peng[6,7,§], Chongyang Hou[1,§], Xiao Wang[8], Ting Wang[9,10], Yu Cao[11,12], Weijia Zhou[1], Ding Sun[14], Kai Wang[13], Mark H. Rümmeli[15,16,17,18,19] (✉), Gianaurelio Cuniberti[2,3,4,5], and Hong Liu[1,20] (✉)

[1] Institute for Advanced Interdisciplinary Research (iAIR), Collaborative Innovation Center of Technology and Equipment for Biological Diagnosis and Therapy in Universities of Shandong, University of Jinan, Jinan 250022, China

[2] Institute for Materials Science and Max Bergmann Center of Biomaterials, Technische Universität Dresden, Dresden 01069, Germany

[3] Center for Advancing Electronics Dresden, Technische Universität Dresden, Dresden 01069, Germany

[4] Dresden Center for Computational Materials Science, Technische Universität Dresden, Dresden 01062, Germany

[5] Dresden Center for Intelligent Materials (GCL DCIM), Technische Universität Dresden, Dresden 01062, Germany

[6] High-Frequency High-Voltage Device and Integrated Circuits R&D Center, Institute of Microelectronics, Chinese Academy of Sciences, Beijing 100029, China

[7] Key Laboratory of Microelectronic Devices & Integrated Technology, Institute of Microelectronics, Chinese Academy of Sciences, Beijing 100029, China

[8] Shenzhen Key Laboratory of Nanobiomechanics, Shenzhen Institute of Advanced Technology, Chinese Academy of Sciences, Shenzhen 518055, China

[9] State Key Laboratory of Biobased Material and Green Papermaking, Qilu University of Technology, Shandong Academy of Sciences, Jinan 250353, China

[10] School of Bioengineering, Qilu University of Technology, Shandong Academy of Science, Jinan 250353, China

[11] Key Laboratory of Modern Power System Simulation and Control & Renewable Energy Technology (Ministry of Education), Northeast Electric Power University, Jilin 132012, China

[12] School of Electrical Engineering, Northeast Electric Power University, Jilin 132012, China

[13] School of Electrical Engineering, Weihai Innovation Research Institute, Qingdao University, Qingdao 266000, China

[14] School of Electrical and Computer Engineering, Jilin Jianzhu University, Changchun 130118, China

[15] Institute for Complex Materials, Leibniz Institute for Solid State and Materials Research Dresden (IFW Dresden), 20 Helmholtz Strasse, Dresden 01069, Germany

[16] College of Energy, Soochow Institute for Energy and Materials Innovations Soochow University, Suzhou 215006, China

[17] Key Laboratory of Advanced Carbon Materials and Wearable Energy Technologies of Jiangsu Province, Soochow University, Suzhou 215006, China

[18] Centre of Polymer and Carbon Materials, Polish Academy of Sciences, M. Curie Sklodowskiej 34, Zabrze 41-819, Poland

[19] Center for Energy and Environmental Technologies, VŠB-Technical University of Ostrava, 17. Listopadu 15, Ostrava 708 33, Czech Republic

[20] State Key Laboratory of Crystal Materials, Center of Bio & Micro/Nano Functional Materials, Shandong University, Jinan 250100, China

§ Jinbo Pang, Songang Peng, and Chongyang Hou contributed equally to this work.

ABSTRACT

Human beings perceive the world through the senses of sight, hearing, smell, taste, touch, space, and balance. The first five senses are prerequisites for people to live. The sensing organs upload information to the nervous systems, including the brain, for interpreting the surrounding environment. Then, the brain sends commands to muscles reflexively to react to stimuli, including light, gas, chemicals, sound, and pressure. MXene, as an emerging two-dimensional material, has been intensively adopted in the applications of various sensors and actuators. In this review, we update the sensors to mimic five primary senses and actuators for stimulating muscles, which employ MXene-based film, membrane, and composite with other functional materials. First, a brief introduction is delivered for the structure, properties, and synthesis methods of MXenes. Then, we feed the readers the recent reports on the MXene-derived image sensors as artificial retinas, gas sensors, chemical biosensors, acoustic devices, and tactile sensors for electronic skin. Besides, the actuators of MXene-based composite are introduced. Eventually, future opportunities are given to MXene research based on the requirements of artificial intelligence and humanoid robot, which may induce prospects in accompanying healthcare and biomedical engineering applications.

KEYWORDS

MXenes, sensors, actuators, gas sensors, biosensors, tactile sensors, sound sensors, artificial retina

1   Introduction

To perceive the surroundings, humans receive five types of senses, including sight, sound, taste, smell, and touch. These sensings (Fig. 1) are correlated to the information perception by the eyes, ears, tongue, nose, and skin. The degradation or diseases of sensory
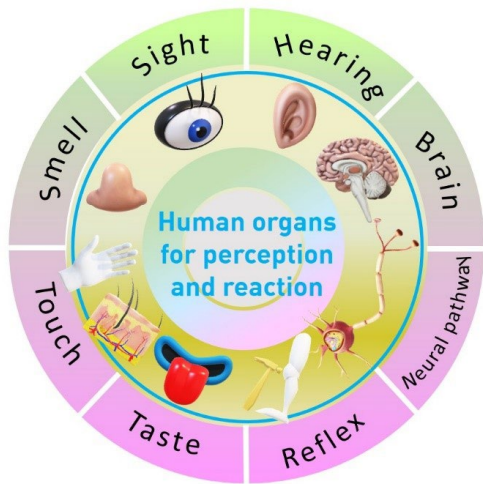
Figure 1 The five sensory organs of humans and their communication with brains.

organs may decrease the happiness of human beings. The development of artificial sensors, which mimic the five sensory organs, tends to bring back a clear perception of the outside world.

MXenes remain the rising-star low-dimensional materials [1–4] after its discovery one decade ago [5–7]. MXenes possess extraordinary mechanical [8, 9], electrical [10, 11], optical[12, 13], magnetic [14, 15], and thermal [16, 17] properties. First, the MXenes have been fabricated in devices of electronics and optoelectronics, e.g., electromagnetic shielding [18, 19], conducting electrodes [20, 21], chemiresistors, transistors [22], photodetectors [23, 24], and solar cells [25]. MXene, as a saturable absorber, shows pulsed laser applications [26, 27]. The MXene-based composites have been employed as thermal conductive pads [28]. The spin regulation by magnetic field leads to spintronics [29]. The surface chemistry of MXenes [30] has provided active sites for catalysis [31], water remediation [32], hydrogen storage [33], sensing and antibacterial treatment [34], as well as wound healing [35]. The large interlayer spacing accommodates lithium ions' intercalation and deintercalation for energy storage batteries [36–38] and capacitors.

To understand the advantages of MXenes, we compare the differences between MXenes and other two-dimensional (2D) materials. Zhang et al. summarized the difference between MXene and other two-dimensional materials according to their optical properties [26]. The dominant features of typical two-dimensional materials are listed in Table 1. Compared with traditional bulk materials, two-dimensional materials [39, 40] are more suitable for human-like sensing applications because of their large surface area [41], high carrier mobility [42, 43], and flexibility [44, 45].

In brief, their differences are depicted as follows. In ultrafast photonics, the low modulation depth of graphene due to atomic-layer thickness has limited its applications. Although topological insulators can achieve nonlinear broadband response, their manufacturing process is complicated, which leads to high costs [56]. When the thickness is fixed, two-dimensional transition metal chalcogenides have certain bandgaps, limiting the optical absorption in the mid-infrared region. Black phosphorus shows continuously tunable bandgaps by changing its thickness; however, phosphorene suffers from weak air stability. Other monoelemental 2D materials remain less intensively investigated, requiring more groups' participation. In contrast, MXene has the features of both adjustable bandgap and good stability, which makes it highly competitive in ultrafast photonics applications.

First of all, we introduce the progress of MXene synthesis. First is top-down such as etching of A layer from bulk MAX phases

and delamination; another is bottom-up, including the direct chemical vapor deposition, as well as the sputtering reaction of Ti, Al, and C for epitaxial MAX film formation, followed by the etching of A layer for remaining MXene film over the supporting substrate. Four reprehensive approaches are listed in Fig. 2. The emerging trends of MXene synthesis include mild synthesis conditions such as alternative etchants other than HF.

One can refer to comprehensive reviews for the most recent advances in MXene synthesis, including the solution processing for obtaining MXene nanosheets [91, 92], additive-mediated intercalation [93], HF-free etching of MAX [26], electrochemical etching [94], anti-oxidation strategies [95, 96], and surface engineering [97–99]. Besides, the posttreatment lead to various types of MXenes, such as MXene quantum dots [100, 101], MXene/polymer composites [16, 102], MXene inks for printed electronics [103], and MXene-based heterostructures [104].

Before discussing the device performances, we look at the structure of MXenes via the classification of MXenes. According to their morphologies, MXene can be divided into four categories, i.e., quantum dots, nanosheets, epitaxial film or large domains (by chemical vapor deposition), and the macroform.

We start with the top-down strategies for producing the quantum dots and nanosheets from the parent MAX phases. First, the MXene-based quantum dots have features in photoluminescence of different wavelengths according to the size of quantum dots. The quantum dots can be prepared by the microexplosion method [105] or high-frequency electromechanical vibration [106]. The quantum dots have demonstrated applications in light-emitting diodes [107], ultrafast photonics [26, 100], cellular imaging [108], and catalytic cancer therapy. Second, the Ti_3C_2 MXene nanosheets can be obtained by selected Al etching of Ti_3AlC_2 MAX phase and delamination. These nanosheets (in dispersions) can be spun or drop-coated onto dielectric substrates for depositing patterned electrodes, which demonstrate the functions of sensors or transistors [109].

Then, we briefly introduce bottom-up synthesis strategies, including a thermal deposition from atomic or molecular precursors and the three-dimensional (3D) assembly from nanosheets. Third, the nanosheets can be assembled into macroform, including clay by powder hydration [110, 111], freestanding membrane by vacuum filtration [21, 112], or aerogel by freeze drying [102, 113]. Fourth, the MXene films can be grown by bottom-up approaches, including the co-sputtering of Ti, Al, and C targets into MAX films and chemical vapor deposition of Mo_2C [114]. The epitaxial film has potential in wafer-scale integrated electronic devices such as transistors, chemiresistors, and photodetectors. The macroform may find its applications in energy storage, such as batteries and supercapacitors, as well as energy conversion, including catalysis. Here, the MXene films become dominant in sensor applications. We come to the discussion of sensor applications of MXenes.

We come to several advantages that MXene possesses in electronic properties for sensors. First, MXene shows high electrical conductivity (6,000–8,000 S·cm^{-1}), exceeding a large number of two-dimensional materials [115]. Second, MXene promotes the recognition of heavy metals [116], humidity [117], hydrogen peroxide [118], acetaminophen [119], biomarkers in whole blood [120], refractive index [121], acoustic sound [122, 123], and human motion [124, 125] in different types of sensors [98]. Solution-gated transistors provide great sensitivity and cycling performances [126]. Besides, MXene has good hydrophilicity because of the OH surface groups [127].

The readers may refer to essential reviews on the emerging topics of heterostructures [96], new types of MXenes beyond Ti_3C_2 [23], and novel device components [97].

**Table 1** The comparison of MXenes with other two-dimensional materials

Materials	Bandgap (eV)	Advantages	Disadvantages	References
MXene	<0.2, monolayer	Adjustable bandgap; wide optical response bandwidth; large nonlinear absorption coefficient; excellent conductivity; high optical clarity	Challenges in homogeneity control during synthesis	[20, 46–49]
Graphene	0, monolayer	High electron mobility and optical transmittance	Low modulation depth (< 2.3%) at monolayer graphene	[50, 51]
Black phosphorus (BP) or phosphorene (P)	0.3, direct, bulk2, direct, monolayer	Broadband nonlinear response for the mid-infrared region; feasible mass production protocols [52]	Weak stability in humidity and air conditions	[53, 54]
Topological insulators (TIs), e.g., Bi$_2$Se$_3$	0.3, indirect, bulk	Broadband nonlinear response	Prolonged recovery time not suitable for an ultra-short pulse; complicated fabrication process	[55–57]
Transition metal dichalcogenides (TMDCs)	1.2, indirect, bulk; 1.9, direct, monolayer	Wide bandgap range that varies with the number of layers, which leads to its unique optical properties	Low charge carrier mobility; low photon absorption in the mid-infrared region	[58–60]
Other single-elemental 2D materials		Feasible large-scale production by both epitaxy, delamination from bulk parents, e.g., tellurene (Te) [61–63]; germanene (Ge) [64–66]	High cost deposition techniques such as molecular beam epitaxy systems and single-crystal substrates; not thoroughly explored by theoretical calculations; experimental results not matching *ab-initio* predication; borophene (B) [67]; silicene (Si) [68–70]	[71–75]
		Stanene or tinene (Sn) [76–79]; arsenene (As) [80–82]; antimonene (Sb) [83]	bismuthene (Bi) [84]; selenene (Se) [85]; gallenene (Ga) [86]	
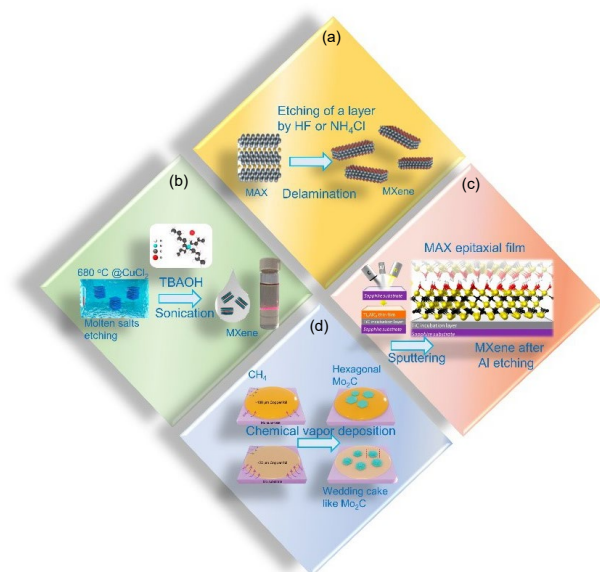
Figure 2 Typical synthesis routes for obtaining MXenes. Top-down: (a) etching of MAX and delamination. Reproduced with permission from Ref. [87], © American Chemical Society 2020. (b) Molten salt etching of MAX and sonication-derived delamination. Reproduced with permission from Ref. [88], © American Chemical Society 2022. Bottom-up: (c) reactive sputtering deposition of MAX film for MXene formation after Al etching. Reproduced with permission from Ref. [89], © American Chemical Society 2014. (d) Direct chemical vapor deposition of Mo$_2$C MXene over Cu/Mo substrate. Reproduced with permission from Ref. [90], © WILEY-VCH Verlag GmbH & Co. KGaA, Weinheim 2019.

According to the types of transduction, the MXenes-based sensors can be categorized by the sensing mechanisms, including plasmonic [128, 129], chemiresistive [61, 130–132], mechanotransducive [133], colorimetric [134], fluorescence [135], and electrochemical [119] approaches.

Here, we provide a timely review of the emerging MXene-based sensors for achieving the performances of artificial organs (Scheme 1), including light sensors, gas sensors, chemical biosensors, sound sensors, and tactile sensors. Besides, the MXene-based actuators are briefly introduced. We start with the sight sense, including photodetectors and image sensors.
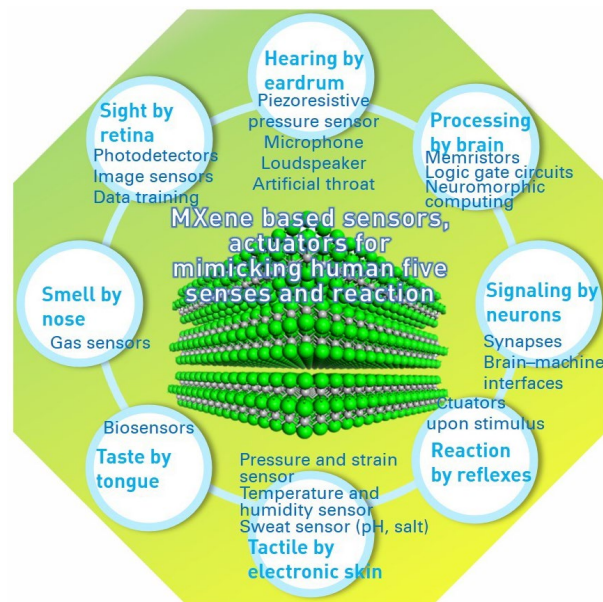
Scheme 1 The MXene-based devices for mimicking five human senses, brain processing, neural pathway, and reflexes.

2　Image sensor for vision sense

The principle of sight is depicted as follows. The eyes convert light to image and color signals for processing by the brain. The retina, a membrane composed of arrays of photoreceptor cells, converts the light beam into nerve pulses, which transform to the synaptic potential and transmit to the brain. Eventually, the brain reconstructs the visual image continuously.

MXene was employed as an electrode for a perovskite-based photodetector array for image sensing. Wang et al. designed an image sensor (Fig. 3) with MXene/perovskite/MXene structures by laser scribing technology. The MXene shows an energy band alignment with the perovskite-based photoactive layers, which facilitates charge transfer at the interface.

Light absorption can be achieved through resonance enhancement in the near-infrared band. The photodetector array enables 1,250-pixel image sensing [136], with a response of 84.8 A·W^{-1}, a specific detectivity of 3.22 × 10^{12} Jones, and a linear
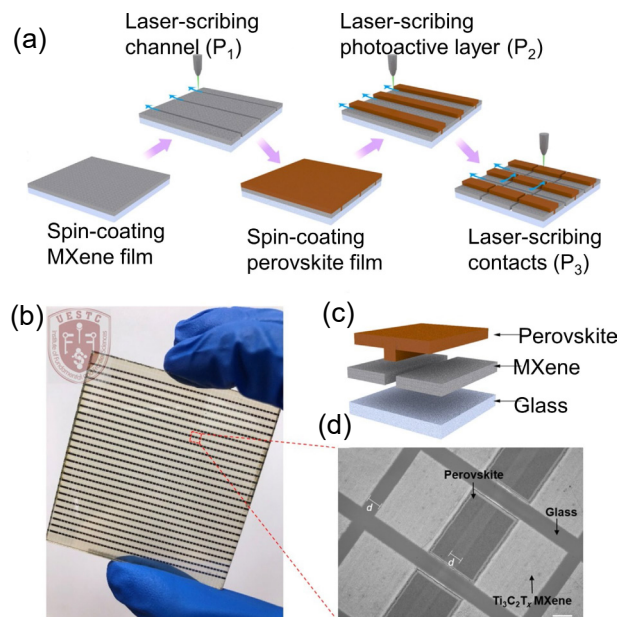
Figure 3 MXene/perovskite/MXene based photodetector array as image sensor. (a) Processes for the fabrication of MXene/perovskite heterostructures by spin coating and laser scribing techniques. (b) Photograph of 50 pixel × 25 pixel image sensor. (c) MXene electrode and perovskite photoactive layer structure of a single pixel. (d) Optical micrograph of MXene electrode and perovskite channel. The scale bar is 200 μm. Reproduced with permission from Ref. [136], © The Royal Society of Chemistry 2020.

dynamic range of 82 dB in the near-infrared region. This work provides a solution for an image sensor of high resolution and pattern controllability.

The transistor array based on MXene can be prepared with patterning techniques, such as direct writing and inject printing. They have drawbacks of low pixel resolution [137–139].

Cheng et al. report an MXene/Si-based image sensor array with a high resolution of 2 μm [140]. The $Ti_3C_2T_x$/Si photodetector has a high-density integrated array of 1,024 pixels (Fig. 4), with a detectivity of 7.7×10^{14} Jones and an ON/OFF current ratio (6.2×10^6).

With a transistor-based detector in each pixel, the MXene/Si image sensor [140] has been fabricated with conventional lithography protocols over a 4-inch wafer, which shows high compatibility with Si technology. The MXene stacking with other photosensitive materials, such as metal sulfides [141–143] or selenides [144–146], leads to the regulation of detection wavelength. For example, $PdSe_2$ [147] may extend to the near-infrared for thermal imaging.

Another 32 × 32 pixel image sensor report has demonstrated a deer's shape [148] based on the heterostructures of MXene/RAN. Here, RAN polymer serves as photosensitive material and MXene as conducting electrodes. Such a photodetector shows transmittance of 70%, excellent mechanical stability, and performance retention under large bending angles.

Future opportunities remain in the coupling of MXene and photoactive materials. First, the metal halide perovskites [149], semiconductor nanowires [150], and metal chalcogenides [151, 152] become emerging photosensitive materials for image sensors. In type I heterojunction, the bandgap engineering facilitates color-sensitive imaging, i.e., wavelength selective photodetection [153] via a bias voltage. Second, more active materials can be selected from conventional solar energy materials, including antimony selenides [154, 155] and sulfides [156, 157] and tandem structures [151], amorphous silicon [158], and four-element compound thin films [159–161]. Third, the charge transport layer may promote the sensitivity and responsivity of the photodetectors.
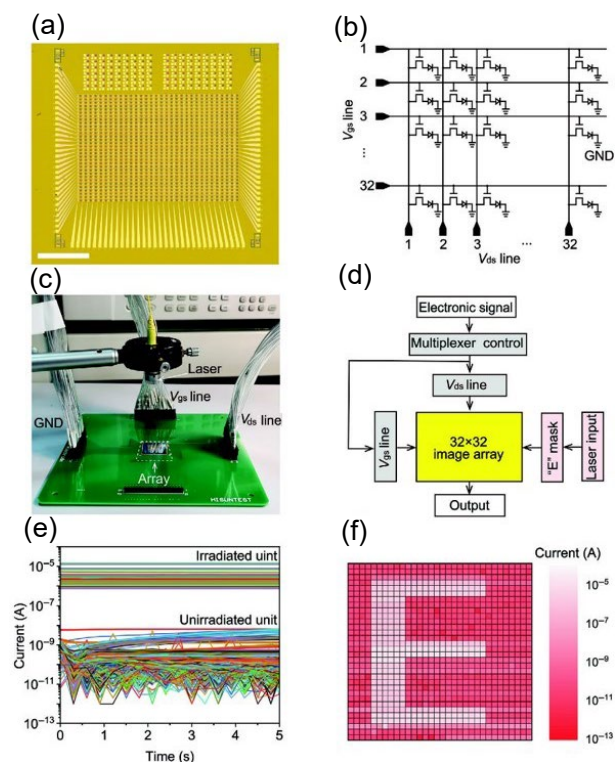
Figure 4 MXene/Si heterostructure-based image sensor. (a) Photograph of an image sensor of 32 × 32 pixel photodetectors. (b) Circuit diagram, (c) photograph, and (d) workflow diagram of the image sensor by a multiplexer technology. (c) Test the array chip using the laser and a shade cover on top of the array. The V_{gs}, V_{ds}, and ground wires (GND, i.e., the chip substrate) are connected to the measuring system. (d) The electrical signal input is controlled by the multiplexer and then generated by the V_{ds} line to generate an array of 1,024 pixels. (e) The 1,024 pieces of drain current curves from each pixel photodetector. The higher current (10^{-6} A) occurs at the irradiated photodetector while the lower current (10^{-9} A) emerges at the dark condition with the light selectively illumination inside the capital E projection. (f) The image detection of E capital alphabet by the 1,024 pixels of drain current after a current mapping. Reproduced with permission from Ref. [140], © Wiley-VCH GmbH 2022.

High-performance optoelectronic devices require significant absorption coefficients, long diffusion lengths, and adjustable bandgap width. High-quality photosensitive materials are among the research hotspots of next-generation optoelectronics. Early image sensors are developed based on light intensity. Future opportunities remain for recognizing color by speculating the wavelength of illuminated light.

3 Artificial eardrum for hearing sense

Human hearing perceives sounds via ear after receiving air vibrations with periodic pressure changes. The auditory system conducts human hearing, which converts the mechanical waves by the eardrum into neural pulse signals for brain collection. Hearing loss can be caused by heredity and congenital at birth, presbycusis in aging people, and acquired by living environments. Several solutions promote hearing ability, such as wearing a hearing aid device and restoring the perforated eardrum.

Firstly, hearing aid devices, which integrate the microphone, amplification circuit, and loudspeaker, have improved the living conditions of deaf people and others with hearing loss. The current technology of acoustic devices suffers from heavy rechargeable nickel-metal batteries, which are not comfortable to carry. The low energy consumption, lightweight, and integration with micro-batteries or micro-supercapacitors are core requirements for technology upgradation. In addition, the safety

[162] and the lifetime of batteries should be taken care of [163]. Therefore, low-dimensional nanomaterials are ideal alternative materials for acoustic membranes in microphones, amplification integrated circuits (if any), and loudspeakers. Secondly, low-dimensional nanomaterials have been implanted in the perforated eardrum of animal models for hearing recovery.

In this section, we discuss the progress in MXene-based acoustic devices, including fundamental components such as microphones and loudspeakers and system-level applications, e.g., artificial eardrums and artificial throats for voice recognition assisted by machine learning and data training.

We begin with the MXene-based microphone device. The sound provides a weak force of continuously regulated frequency that can be transduced to electric current by a microphone.

The vibration of air or water typically transmits the sound. Humans can hear the audio frequency ranges from 20 to 20,000 Hz. The acoustic wave induces the sound pressure (with a pascal unit), a frequency-dependent periodic change in local air pressure, which varies from one standard atmosphere. The microphone can measure the sound pressure.

The sound pressure level (SPL) depicts the relative pressure compared to a standard value in a logarithmic format, i.e., $20 \log_{10}(p/p_0)$ dB, where p is sound pressure and p_0 is 20 μPa as reference.

The typical acoustic membranes rely on isinglass, wood, mica, and polymers. They feature heavyweight and are not easily tailored. The ultimate goal for acoustic devices is to produce or detect a sound with high sensitivity, low detection limits, and a broad frequency spectrum [164]. Further improvement in acoustic performances remains challenging based on these conventional materials. Nanostructured materials may improve the performance of acoustic membranes. Acoustic sensors made of graphene [164] and carbon nanotubes [165] have been reported to detect human voices and recognize speech assisted with deep data learning.

Here, we discuss the artificial eardrum based on the MXene membrane. Ren et al. constructed an MXene-based piezoresistive pressure sensor that simulates artificial eardrums (Fig. 5) and combined it with machine learning to perform sound detection and recognition [166].

The pressure sensor [166] performs well, including a sensitivity of 62 kPa^{-1} and a detection limit (of 0.1 Pa). The MXene artificial eardrum (Fig. 6) can precisely record audio waves comparable to commercial recorders. Based on the voice recognition algorithm, the MXene eardrum-based artificial auditory system can identify 280 voice signals with 96.4% accuracy. The concept of acoustic devices shows promising applications in wearable healthcare devices.

The artificial throat is introduced based on MXene. In the human throat, the larynx produces sound by periodic opening and switching off the vocal cords [167, 168], which chop the continuous airflow to pulsed sound waves. The collisions of vocal cords produce harmonics, with a fundamental frequency of 120 Hz for men and 210 Hz for women. The artificial larynx or vocal cords become necessary for mimicking human voices, reparating voice loss, and restoring throat diseases.

Ding et al. prepared an MXene-based artificial throat that recognizes the pair (ɑː and æ) of a long and short vowel by sound detection sensor [169]. The MXene-based acoustic sensor achieves a perceived response to pressure and vibration (Fig. 7).

They used the convolutional neural network model [169] to recognize syllables in human pronunciation, which can identify long and short vowels. The study could broaden the applications of MXene acoustic sensors in sound generation for mimicking the larynx and vocal cords. The loudspeaker component based on
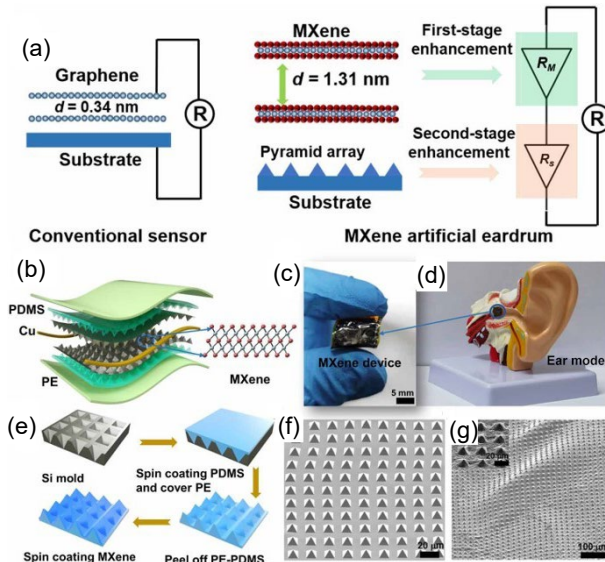

Figure 5 The MXene/PDMS-based piezoresistive pressure sensor. (a) Resistance model diagram. (b) Scheme of the pressure sensor. (c) Photograph of MXene-based pressure sensor and (d) ear model. (e) Fabrication protocol and (f) and (g) scanning electron microscopy (SEM) micrograph of the pyramid of PDMS. Reproduced with permission from Ref. [166], © Gou, G. Y. et al. 2022.
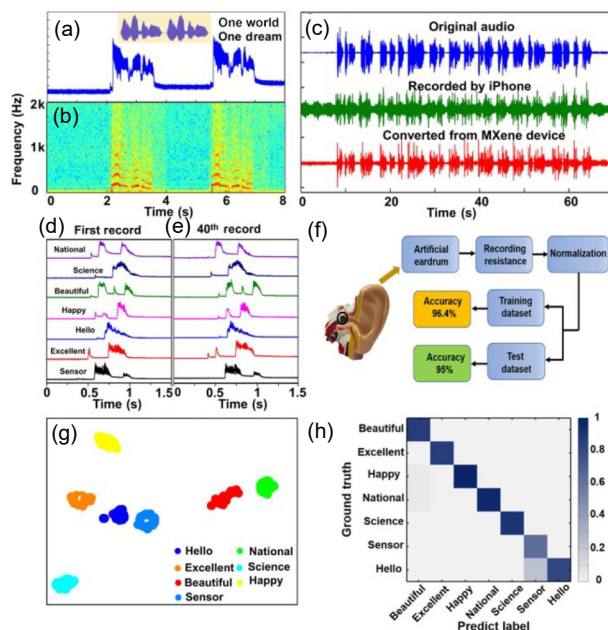
Figure 6 Artificial eardrums based on MXene piezoresistive pressure sensors for sound sensing and voice recognition. (a) The recorded sound wave and (b) spectrum in the means of frequency (related to the resistance change) of the MXene eardrum. The frequency was equivalently calibrated to the sound pressure, which has a linear relationship to the change ratio of initial resistance $\Delta R/R_0$. The sensitivity of such a pressure sensor is extracted as the slope of the $\Delta R/R_0$ versus ΔP curve, viz., the $(\Delta R/R_0)/\Delta P$ is constant of 62 kPa^{-1}, where ΔP is applied sound pressure. (c) Comparison of the recorded wave curves by MXene eardrum and iPhone with the original audio. Good retention between (d) the initial recording and (e) after 40 cycles of recording tests for seven words. (f) Machine learning for voice recognition based on the k-means clustering algorithm. The 40 times recording of seven words has produced 280 pieces of recordings. Among them, 140 recordings were employed as data training sets. Another 140 pieces of recording were used for testing data sets. The voice recognition results by (g) strategy of t-distributed stochastic neighbor embedding and (h) confusion mapping of prediction against the testing dataset. Reproduced with permission from Ref. [166], © Gou, G. Y. et al. 2022.

MXene is still an ongoing investigation. The MXene has proven outstanding biocompatibility. But, the reparation of perforated eardrums by MXene membrane remains unexplored.
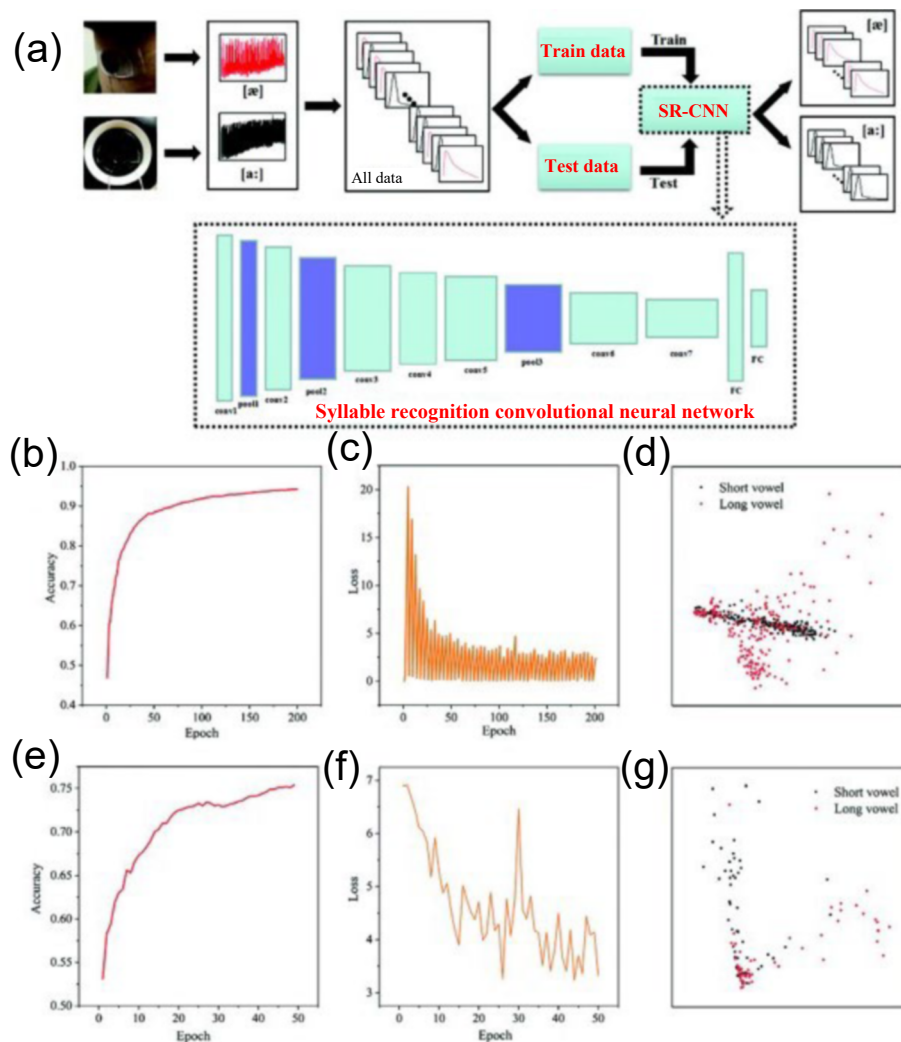
Figure 7 Syllable recognition through MXene-based artificial throat by deep learning. (a) Workflow for syllable (ɑː and æ) recognition based on convolutional neural network. In the structure of a convolutional neural network, the conv, pool, and FC denote the convolution layer, pooling layer, and fully connected layers, respectively. (b) The accuracy and (c) loss of syllable recognition with the number of training epochs. The training set was from the 200 values of $\Delta R/R_0$ of MXene-based piezoresistive sensor with sound pressure from the loudspeaker. $\Delta R/R_0$ denotes the relative change in resistance upon the sound detection of MXene device. (d) Visualized recognition output diagram of the sound (ɑː and æ) from a loudspeaker. (e) The accuracy and (f) loss of syllable recognition with the number of training epochs. The training set was from the 50 values of $\Delta R/R_0$ of sound sensor when detecting sound pressure from the human throat. (g) Visualized recognition output diagram of the voice from the human throat. Reproduced with permission from Ref. [169], © WILEY-VCH Verlag GmbH & Co. KGaA, Weinheim 2020.

4 Gas sensors for olfaction sense

The olfaction sense is generated by the recognition of the gas molecules in the air. Here we discuss the MXene-based gas sensors. We take examples of acetone, methanol, toluene, and humidity to demonstrate the MXene potentials in gas detection.

Acetone, as a biomarker of diabetes [170, 171], indicates insulin levels that promote glucose conversion. When blood sugar levels rise, the acetone concentration decreases in the exhaled gas and increases in insulin [172, 173]. Therefore, an acetone gas sensor [174, 175] provides an early diagnosis of diabetes and health monitoring. Most acetone sensors employ metal oxides for catalytic oxidation of acetone to change the conductance as a sensing mechanism. The MXene incorporation could elevate the sensor performances by a large specific area and excellent conductivity.

Wang et al. designed an acetone sensor based on chemiresistors of α-Fe$_2$O$_3$/MXene heterostructure [176]. The sensor can detect acetone content by the amount of electron transfer upon the acetone decomposition. The sensor has shown good selectivity of acetone detection, viz., the response to acetone has exceeded six times than that of other organic molecules such as toluene and alcohols [176].

Two mechanisms account for the sensitivity and selectivity of the sensor. First, the hydrogen bonds between MXene and acetone (Fig. 8) guarantee the efficient chemisorption of acetone, which is favored compared to aromatic molecules without forming hydrogen bonds. Second, the bond dissociation energy of acetone (366 kJ·mol^{-1}) is much lower than methanol and ethanol; therefore, the oxidation of acetone provides a large number of electrons for increasing the conductance of the chemiresistors-based sensors.

The sensing mechanism is depicted as follows. The adsorption capacity of the sample surface was analyzed according to the density functional theory (DFT) calculation. The surface model of the heterostructure was optimized (Fig. 8) to α-Fe$_2$O$_3$/MXene. The gas sensitivity mechanism of the α-Fe$_2$O$_3$/ MXene sensor to acetone was discussed.

Such a sensor, which operates at room temperature, exhibits specific selectivity for acetone, with a response of 16.6% to 5 ppm acetone and a response/recovery rate of 5/5 s. The acetone sensor has a large humidity tolerance ranging from 20% to 80%. Cycling tests show good performance retention after 28 days, which provides an essential reference for acetone sensing at room temperature.
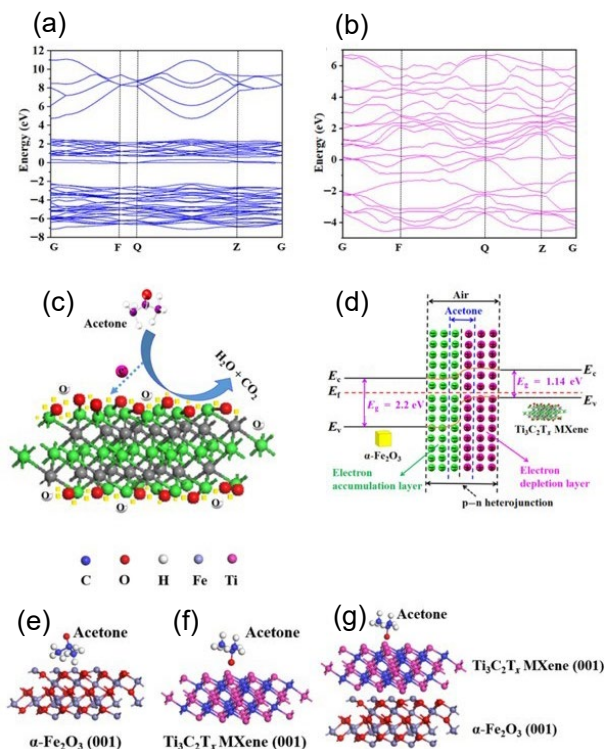
Figure 8 The mechanism of acetone sensing at the MXene/α-Fe$_2$O$_3$ heterostructure. Electronic structure of (a) α-Fe$_2$O$_3$ and (b) MXene from density functional theory calculation. (c) The electron transfer to MXene electrode after the oxidation of acetone adsorbed at the MXene surface. (d) The band alignment of MXene/α-Fe$_2$O$_3$ heterostructure. The geometry of acetone chemisorbed on three kinds of surfaces (e) α-Fe$_2$O$_3$, (f) MXene, and (g) MXene/α-Fe$_2$O$_3$. Reproduced with permission from Ref. [176], © Elsevier B.V. 2021.

Methanol, which is converted from a waste of biomass, has been employed in fuel cells for consumer electronics and vehicles [177, 178]. Methanol is toxic to the body's perception organs, blood, and nervous systems [179, 180]. Often, the methanol sensors employ noble metals for catalytic oxidation of methanol to provide electron transfer, which induces resistance change as a sensing mechanism. Therefore, it is necessary to develop a quick and easy gas-sensing method to detect methanol [181–183].

Wang et al. fabricated a methanol sensor based on chemiresistors of In$_2$O$_3$/MXene heterostructure [184]. Here the In$_2$O$_3$ serves as a sensitive material for providing electrons to chemisorbed oxygen molecules to form O$_2^-$. The highly reactive O$_2^-$ oxidizes the methanol into carbon dioxide and releases electrons, which increases the conductance of the chemiresistors as a sensing mechanism. The MXene, as an electron-rich species, promotes the electron transfer to the depletion layer of In$_2$O$_3$.

When the sensor is initially exposed to air, the In$_2$O$_3$/MXene shows a decrease in carrier concentration due to electron depletion by forming O$_2^-$ and an increase in resistance. When methanol is adsorbed to In$_2$O$_3$ surface, O^{2-} can release electrons for methanal oxidation [185], which results in conductance changes and improves the sensitivity.

The sensor [184] exhibits a response rate of 29.6% for five ppm methanol and a response/recovery time of 6.5/3.5 s. This method of combining metal oxides/MXene provides methanol detection options.

Toluene is widely used in interior decoration as an adhesive solvent. Toluene is highly toxic to the respiratory system and can lead to nasopharyngeal cancer and bronchial disease [186]. Besides, toluene becomes an essential biomarker of lung cancer. Therefore, detecting toluene traces becomes significant for early lung cancer diagnosis [187, 188].

Salama et al. designed MXene-based sensors for the selective detection of toluene [189]. They used ultrasound treatment to increase the specific surface area of Mo$_2$CT$_x$ MXene materials, which eventually reflected in the improvement in device performances.

The MXene sensor exhibits remarkable selectivity for toluene sensing [189], which causes over three times larger responses than the other four gaseous molecules, including benzene, ethanol, methanol, and acetone. According to the *ab initio* calculations, the toluene shows the lowest adsorption energy at the MXene surface among the five types of organic molecules. First, the alcohol and ketone molecules are chemisorbed on MXene surfaces by hydrogen bonding [190]. Second, the interaction between the benzene ring and MXene is more robust than hydrogen bonds, reducing the charge carriers' concentration and increasing the MXene channel's resistance. Third, the methyl radical in toluene [191] enhances the activity of aromatic rings compared to benzene, which accounts for the best response in sensing toluene.

The toluene sensor based on MXene [189] has a limit of detection of 220 ppb, a linear detection range (35–170 ppm), and a sensitivity of 0.037 Ω·ppm^{-1}.

The Ti$_3$C$_2$T$_x$ MXene sensor can detect acetone, methanol, and ammonia at room temperature [192–195]. MXene has been reported in examining the concentration of volatile organic compounds (VOCs) in a nitrogen environment, which mimics air ambiance [196]. In these laboratory works, the impact of humidity on sensor performance has not been considered.

Sysoev et al. investigated the influence of humidity on the performances of gas sensors based on MXene chemiresistors in detecting organic and inorganic molecules [197]. The MXene-based humidity sensor has achieved a record limit of detection (10 ppm) for sensing H$_2$O concentration (Fig. 9), which exceeds the performance of a commercial humidity sensor.

In the background of dry air, the sensor can be used to detect volatile organic gases, alcohols, acetone, and ammonia. But in wet air, only ammonia [197] causes the change in resistance, while other analytes do not change sensor resistance compared to the reference wet air. The strong hydrogen bonds between ammonia and MXene may account for the change in conductance. Indeed, other organic solvents, which do not form hydrogen bonds with MXene, cause no change in resistance in MXene channels. It shows the concerns of significant interference by the water [197], which makes the organic gases undetectable, i.e., no conductance changes in sensor resistance when incorporating organic gases in wet air. Therefore, the target analytes' dry treatment becomes necessary before the concentration examination.

Moreover, a multi-sensor array can be integrated with the same wafer with the Mo$_2$CT$_x$ MXene as a sensing material, potentially detecting different vapors parallelly by multiplexer technology.

5 Chemical biosensors for gustation sense

The perception of food taste turns vital for human happiness when going to dinner. The tongue hosts the taste receptor cells for recognizing the taste of different chemicals. We discuss the chemical biosensors based on MXenes for detecting chemicals that produce the sense of taste. Samples for recognition are capsaicin, inosine monophosphate, and L-glutamate.

First, capsaicin, as the primary source of spiciness, has induced spicy Chinese dishes, which has a large consumer group. One evaluates the degree of spicy food by the content of capsaicin. Standardizing pre-cooked dishes requires precise control of capsaicin content in food. Hence, one can evaluate capsaicin concentration by various methods, including colorimetry [198],
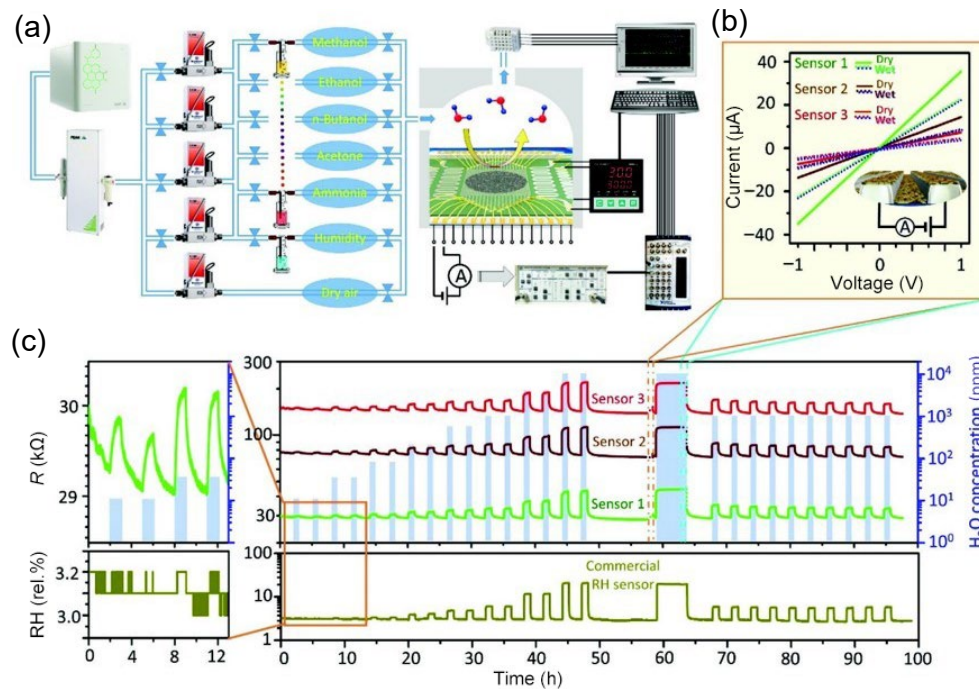
Figure 9 The MXene-based chemiresistors array for multiple gas sensing by data collection card with multiplexer technology. (a) The scheme of gas sensing system. The multiple analyte gases controlled by a flowmeter with dry air and wet air as reference (left). The multi-channel data collection by multiplexer card and personal computer software (right). (b) The response current curves of three kinds of humidity by three sensors. (c) The comparison of humidity sensing performances of MXene-based chemiresistors and the commercial humidity sensor. Reproduced with permission from Ref. [197], © Pazniak, H. et al. 2021.

spectrophotometry [199], and liquid chromatography-mass spectrometry [200]. Among them, electrochemical sensors can reduce the cost of expensive equipment and save the detection time of complex operation protocols.

Xu et al. designed an electrochemical sensor for capsaicin detection using MXene/poly(diallyldimethylammonium chloride) (PDDA)-carbon nanotubes/β-cyclodextrins [201]. The sensor utilizes MXene and carbon nanotubes to amplify the electrochemical current signal (Fig. 10) by enlarging the specific surface area of the composite. Indeed, the redox current gets extensively promoted by the MXene composite modified work electrode compared to bare glassy carbon. The β-cyclodextrins improve the degree of dispersion of the MXene-based suspension.

The MXene-based electrochemical sensor [201] was employed to detect capsaicin in three commercially available Chinese food, including pot-roast duck neck, pot-roast chicken claw, and pot-roast beef, which are heavily cooked with soy sources. The sensor achieves a linear detection range of 0.1–50 μmol·L^{-1}, with a limit of

detection of 0.06 μmol·L^{-1} and a recovery rate of 84%–126%. This work has potential application in detecting food content, which mimics the function of gustation organs such as tongues.

Second, inosine monophosphate can be an essential indicator of meat quality. Liu et al. [202] adopt the MXene/enzyme-modified glassy carbon electrode in a biosensor for detecting inosine monophosphate. In the double-enzyme hydrolyzed inosine monophosphate process, the decomposition of H_2O_2 leads to the transfer of charge, producing an electric current. Subsequently, the current change can determine the content of inosine monophosphate.

Such a biosensor, with a linear detection range of 0.04–17 g·L^{-1} and a detection limit of 2.73 ng·mL^{-1}, promotes an easy and quick detection of inosine monophosphate content. The MXene/enzyme-based biosensor [202] has precisely detected the content of inosine monophosphate in four kinds of meat, including chicken and beef. Indeed, the amount of ingredient of inosine monophosphate was evaluated by such a biosensor, e.g., 1.88 mg·g^{-1} in chicken and
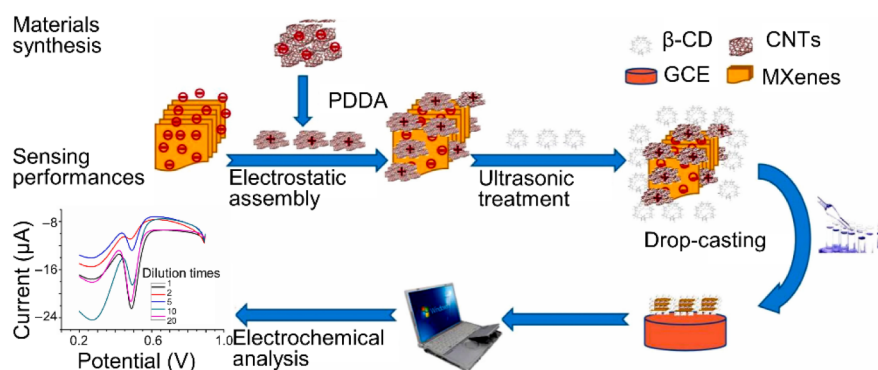
Figure 10 MXene-based composite as electrochemical work electrodes for sensing capsaicin. First, MXene nanosheets, which are negatively charged, react with positively charged PDDA-decorated carbon nanotubes through electrostatic effect. The PDDA denotes poly(dimethyldiallylammonium chloride). Then, β-CD was immobilized on the MXene-based materials by ultrasonic treatment. The β-CD denotes β-cyclodextrin. Subsequently, the MXene composite-based dispersion was drop-cast onto the glassy carbon. Eventually, MXene-modified glassy carbon was employed in the electrochemical workstation for capsaicin detection. Reproduced with permission from Ref. [201], © Elsevier Ltd. 2022.

2.44 mg·g⁻¹ in beef, which showed a low relative deviation (< 2%) compared to commercial liquid chromatography.

Third, L-glutamate is one of the components involved in the human perception of food taste, and the content of free glutamate can determine the umami taste of food [203]. Monosodium glutamate, which is rich in L-glutamate, has been widely used in cooking Chinese dishes. The accurate determination of the glutamate content of foods can provide information on food safety and standardization of pre-cooked food [203] that the capital market favors.

Liu et al. developed an MXene electrochemical sensor based on Pt nanoparticle modifications for the selective detection of glutamate [203]. The sensor uses the decomposition of H_2O_2 (produced during enzyme-catalyzed glutamate oxidation) to cause electron transfer to glassy carbon for electrochemical sensing (Fig. 11).

In evaluating glutamate concentration, the MXene-based biosensor shows a linear detection range of 10–110 µmol·L⁻¹, a sensitivity of 1.59 nA·µmol⁻¹, and a limit of detection of 0.45 µmol·L⁻¹. The sensor can be successfully used to detect monosodium glutamate as added to cooked foodstuff such as soy sauce, beef, and vegetable soups. The detection results of such an MXene-based biosensor are comparable to commercial liquid chromatography.

Besides, the field-effect transistors guarantee the recognition of miRNA [204]. Similarly, the photodegradation of organic dye molecules can be monitored by optical methods [205]. The transistor performances can be promoted by interface engineering [206] and Fermi-level depinning [207]. The transistor arrays guarantee industrial production compatibility [208].

MXene-based biosensors can detect more taste-related chemicals. The data fusion of several chemical sensors could lead to taste recognition.

6 Pressure sensors for touch sense

The tactile sense is produced by human skin through environmental pressure, temperature, and humidity. Electronic skin (e-skin) has become a crucial replacing material in prosthetic limbs, stretchable electronics, and biomedical monitoring.

Electronic skins, also called pressure sensors, have the advantages of sensitivity, stretchability, and lightweight, which satisfy the requirements of wearable and flexible electronics. The pressure sensors consist of flexible substrates, sensitive materials, and conducting electrodes. First, MXenes become emerging conductive materials [209] compared to indium tin oxide, metals, and graphene. Second, the MXene can incorporate into the polymeric composite [168, 210–215] as an active layer for improving the sensitivity. Moreover, the active layer may employ the macrostructures, such as interlocking [216], hollow spheres [217], porous [218], and lamellar architectures [219].

Four work mechanisms exist in the pressure sensor for touch senses, including piezo-capacitive, piezoresistive, piezoelectric, and triboelectric modes. Here, we discuss the recent progress of MXene incorporation in these four types of pressure sensors. First, we start with the capacitive mechanism for pressure sensing.

Tung et al. [220] designed an electronic skin based on a piezo-capacitive pressure sensor of MXene/polyacrylamide hydrogel heterostructures (Fig. 12(a)). In a parallel plate capacitor, the MXene/polypyrrole nanowires serve as both the top and bottom conductive plates. Meanwhile, the vinyl silica nanoparticle-modified polyacrylamide hydrogel and elastic tape play the role of dielectric (Fig. 12(b)).

In the elastomer performance, the abundant bonding between polymers and nanowires has reduced the energy dissipation of the hydrogel network [220]. Indeed, the composite exploits hydrogen bonds on polyacrylamide molecular chains and covalent bonding between polyacrylamide and vinyl-hybrid-silica nanoparticles, improving the sensor's toughness and responsiveness. Moreover, the formation of hydrogen bonds between bridging layers of polypyrrole nanowires and MXene can promote the sliding stability of MXene/hydrogel heterostructures. Therefore, the material has a skin-like strain-sensitive deformation and recovery behavior.

Furthermore, piezo-capacitive sensing is formed by pressing two heterogeneous structures together. When the external environment changes, the electric field of the electronic skin changes, and the charge transfer changes the capacitance, achieving sensing at a distance of 20 cm (Fig. 12), which is closer to the natural skin performance. The MXene sensor has significance in prosthetics or robots with a natural feeling.

When a significant strain applies (e.g., considerable gesture change when playing badminton and wearing e-skin sensors on forearms), the piezo-capacitive sensor does not operate accurately. Therefore, the piezoresistive mechanism applies to provide monitoring. Indeed, the MXene sensor [220] has a vast work range of up to 2,800% (breaking strain), a response of 90 ms, an elasticity of 240 ms, and reproducibility of greater than 5,000 cycles.

Eventually, an intelligent system is assembled to monitor finger approaching and pressuring (Fig. 13). Indeed, the MXene-based e-skin is transmitted to a data analyzer circuit and connected to a smartphone app with a wireless Wi-Fi module for real-time human motion monitoring by attaching to the elbow joint.

Now we turn to the piezoresistive sensor. Shen et al. designed a flexible piezoresistive sensor using MXene/polyacrylonitrile composite membranes [210]. The polyacrylonitrile and MXene nanosheets were blended thoroughly to form a composite (Fig. 14)
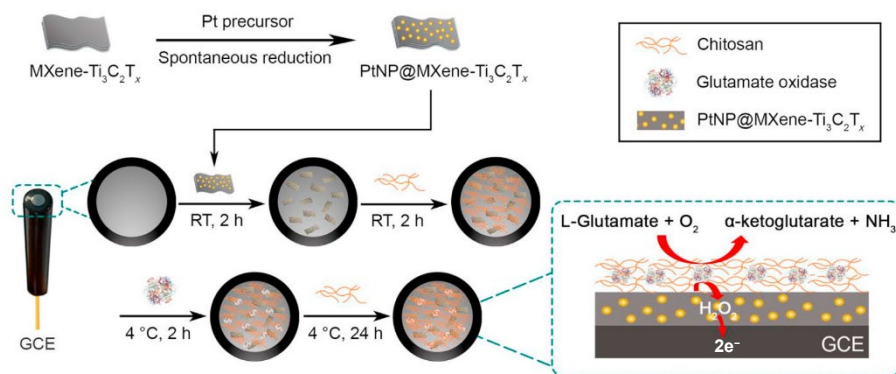
Figure 11 MXene/Pt nanoparticles/enzyme composite modified glassy carbon as electrochemical sensors for detecting the concentration of L-glutamate. The amperometry was employed to collect the current at the work electrode from the electron transfer due to the oxidation of H_2O_2. L-glutamate oxidation (catalyzed by glutamate oxidase) generates H_2O_2, indicating L-glutamate concentration. Reproduced with permission from Ref. [203], © Elsevier Ltd. 2021.
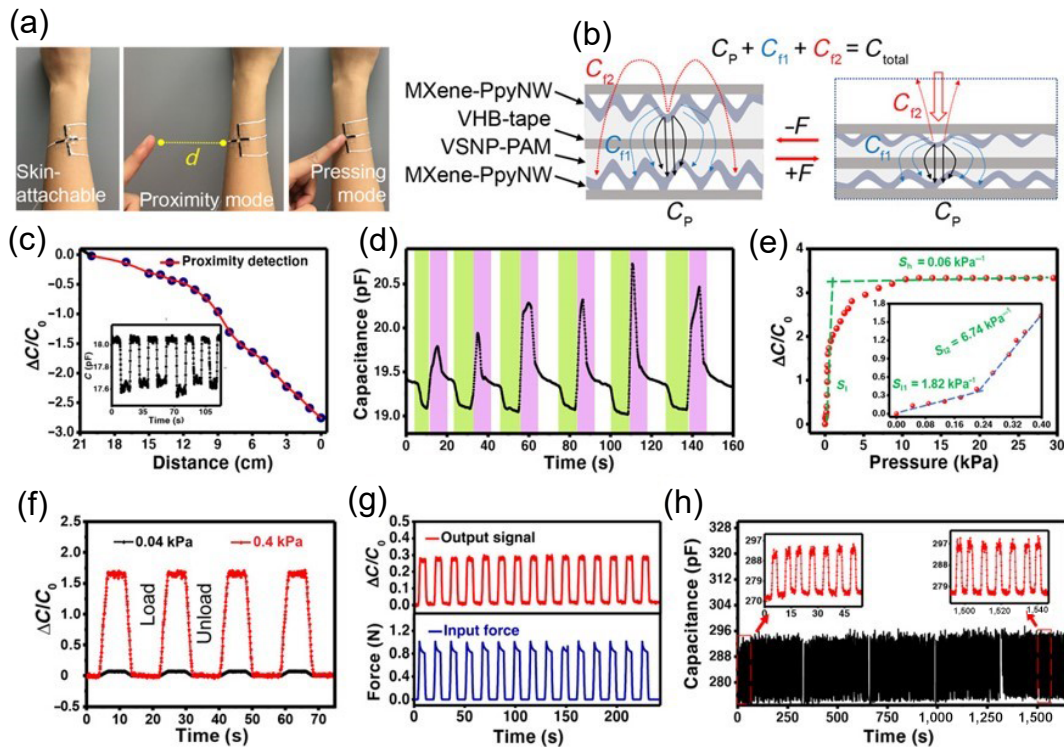
Figure 12 MXene/PpyNW-VSNP-PAM based piezo-capacitive pressure sensor for electronic skin. (a) Photograph of the e-skin sensor attached to forearm. (b) Capacitance model of the parallel plate capacitor with MXene-PpyNW as conductive plates and the VHB-tape and VSNP-PAM as a dielectric. PpyNW denotes polypyrrole nanowires. VHB is an elastic tape model (VHB 4905). VSNP-PAM denotes the vinyl silica nanoparticle-modified polyacrylamide hydrogel. (c) Capacitance change versus the distance between the finger and the sensor surface. (d) Cyclic test of capacitance changes by periodically approaching, pressing, and retracting the finger to the electronic skin. After approaching the sensor with a finger, the fringing capacitance C_{f2} (through air medium) decreases (green). When the finger pressure applied to the sensor gradually increases, the plate electrode capacitance C_p and fringing capacitance (in the overlay area through elastic tape) C_{f1} increase (pink). When releasing pressure by retracting the finger, the capacitance recovers to the initial state (white). (e) Capacitance changes with pressure in a linear relation ranging from 0 to 0.4 kPa, then in a second linear range to 4 kPa and gradually saturated at 10 kPa. The capacitive sensor is not accurate (applicable) to large strains (> 1%) where piezoresistive sensor operates. (f) The capacitance versus input pressures. (g) Calibration of capacitance relative change ratio as output signal with pressure force as input. (h) Sensor durability testing for 5,000 cycles at pulsed pressure force of 1 kPa and 0.13 Hz. Reproduced with permission from Ref. [220], © Cai, Y. C. et al. 2020.

encapsulated and electrically connected by both MXene electrodes. When pressure is applied, the voids in the fiber network are compressed, allowing the MXene nanosheets to come into closer contact with each other. The close connection of MXene nanosheets increases the number of current paths, thereby significantly increasing the contact area of the composite fiber network. These structures minimize strain caused by bending.

Besides, they used the piezoresistive sensor to form a circuit with the light-emitting device (LED) (Fig. 15). When the sensor resistance changed, the voltage of the LED changed accordingly, thus characterizing the pressure received by the sensor with the brightness of the LED [210].

The sensor shows a sensitivity of 104 k·Pa^{-1}, with a response/recovery time of 30/20 ms and a limit of detection (1.5 Pa) to withstand 240 bending cycles. The sensitivity of this MXene electrode-based sensor is 20 times higher than similar sensors [221–224] using traditional nickel, copper, gold, or silver electrodes. The sensor can detect subtle movements of muscles, such as finger bending. The study allows MXene to combine with polymer fibers to design wearable devices.

The slight motion of humans can be quantified by MXene/polyimide aerogels-based piezoresistive sensors [225]. The gentle carotid artery has changed the resistance by 0.4% due to the small deformation (Fig. 16).

Indeed, the gestures of breath, swallowing, and pronunciation [225] were perturbed by the change in resistance, $\Delta R/R_0$, below 10%. But the bending of the finger and knee achieved changes in resistance of 20%–30%.

Next, we come to discuss the piezoelectric potential-based pressure sensor. Ko et al. used MXene/ferroelectric polymer-based composite to design the piezoelectric pressure sensor [226]. The sensor uses functional groups on the surface of MXene to form hydrogen bonds with polyvinylidene fluoride (PVDF) to bind them. The MXene has a charge accumulation effect in MXene/polyvinylidene fluoride. When subjected to external pressure, the enhanced polarization of the sensor interface induces electron transmission to balance the potential, which in turn enhances the piezoelectric potential output. In addition, the porous structure of the sensor produces a local stress concentration effect at the hole after being pressed (Fig. 17), which makes the sensor's sensitivity several times higher than that of the planar structure.

Subsequently, we update the report on triboelectric nanogenerator-based pressure sensors. Li et al. [227] proposed the MXene as electrodes for connecting the triboelectric layer to form a nanogenerator-based pressure sensor (Fig. 18). Polytetrafluoroethylene (PTFE) was employed as filtration paper to support MXene film formation during vacuum filtration.

Besides, the PTFE serves as a triboelectric layer in the MXene/PTFE/MXene-based triboelectric nanogenerator (TENG). The TENG works in contact–separation mode. The pressure sensor has shown significant sensitivity and an excellent retention ratio in a cycling test of 6,000 cycles.

The MXene-based TENG can operate in a single electrode mode driven by the falling and sliding of water droplets. Indeed, the device inside an infusion pipe works for remote drop counting (Fig. 19). Therefore, it may hold promise in biomedical and healthcare applications.

The MXene electrodes assisted TENG [227] have promoted the sensitivity (6.1 V·N^{-1}) to subtle force, together with fast rising and
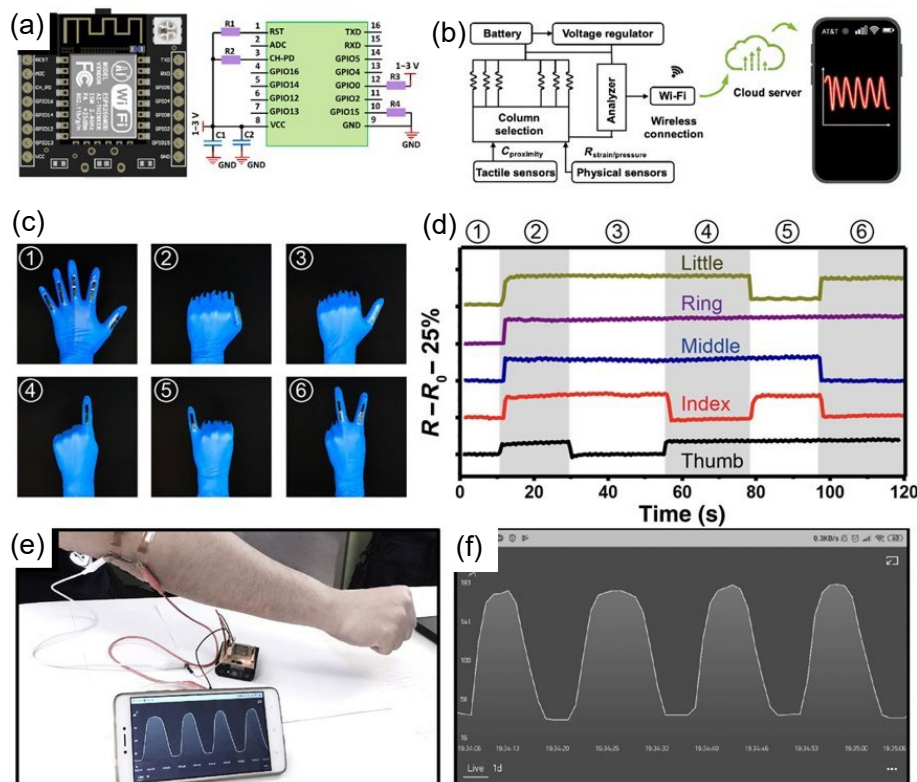
**Figure 13** Intelligent system for recognizing the finger approaching and elbow-joint bending based on MXene electronic skin. (a) Photograph and circuit scheme and (b) electric diagram of the intelligent system. (c) Six types of finger gestures and (d) piezoresistive response curves of the five sensors attached to five fingers. (e) The operation of the intelligent system by the e-skin sensor attached to elbow joint for (f) real-time sensing by relative resistance change ratio. Reproduced with permission from Ref. [220], © Cai, Y. C. et al. 2020.
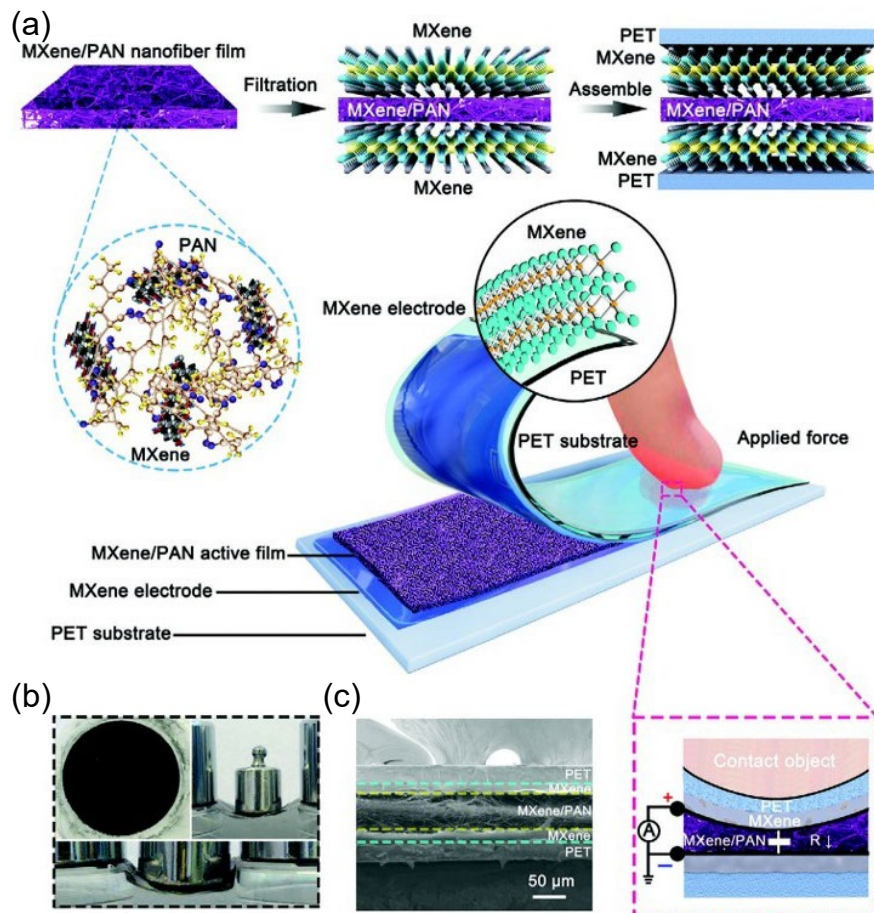
Figure 14 The MXene/PAN-based pressure sensor and piezoresistive mechanism. (a) The structure of the piezoresistive MXene/PAN composite and the MXene electrode connected pressure sensor. PAN denotes 3D polyacrylonitrile. (b) Photographs of the MXene/PAN membrane over filter paper and its application in supporting the weight load. (c) Cross-section SEM image of sandwich MXene electrode/MXene-PAN/MXene electrode in the piezoresistive sensor. Reproduced with permission from Ref. [210], © Wiley-VCH GmbH 2021.
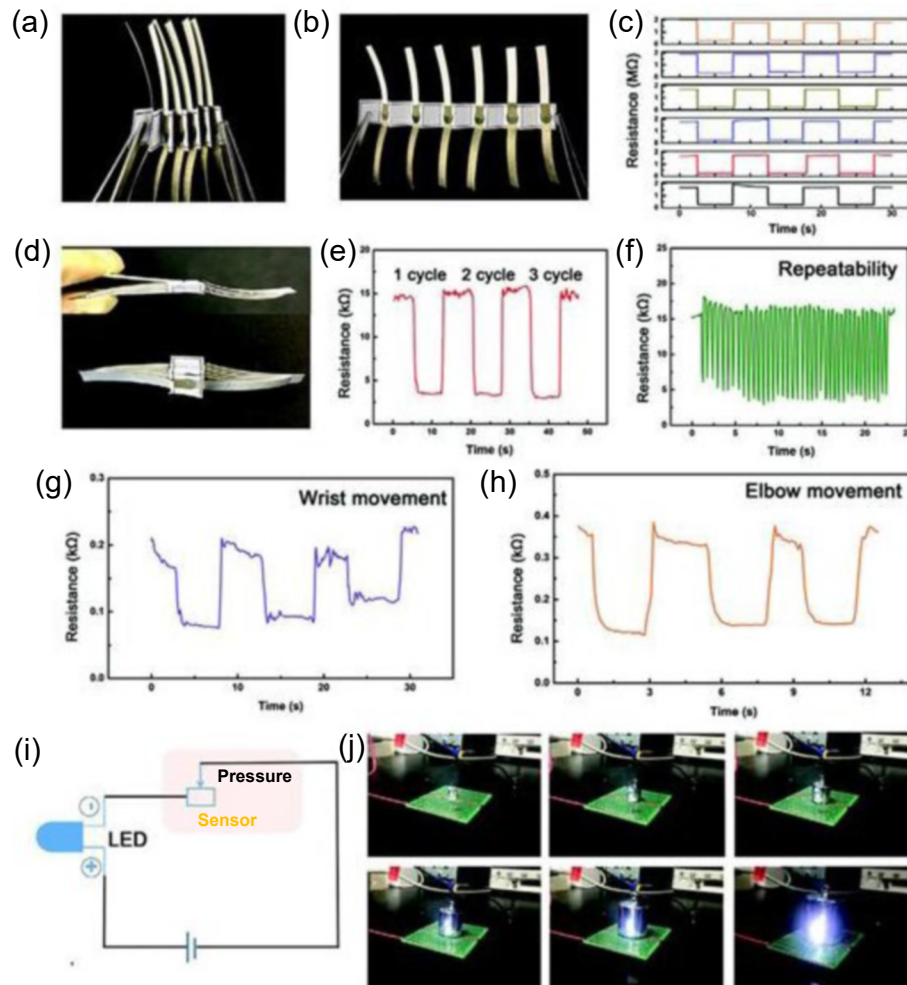
Figure 15 Demonstration of MXene/PAN-based piezoresistive sensor. The integration of six pieces of pressure sensors in a folding paper at (a) half-folded state, (b) flat state, and (d) folded state. The real-time resistance curves of the periodical folding and unfolding of (c) one individual pressure sensor and (e) the six pieces for an integrated pressure sensor. (f) Cycling test. Real-time resistance curves of the folded sensor attached to (g) wrist and (h) elbow. Demonstration of the resistance reduction upon a load of gradually increasing weight by (i) the circuit diagram and (j) photographs. Reproduced with permission from Ref. [210], © Wiley-VCH GmbH 2021.
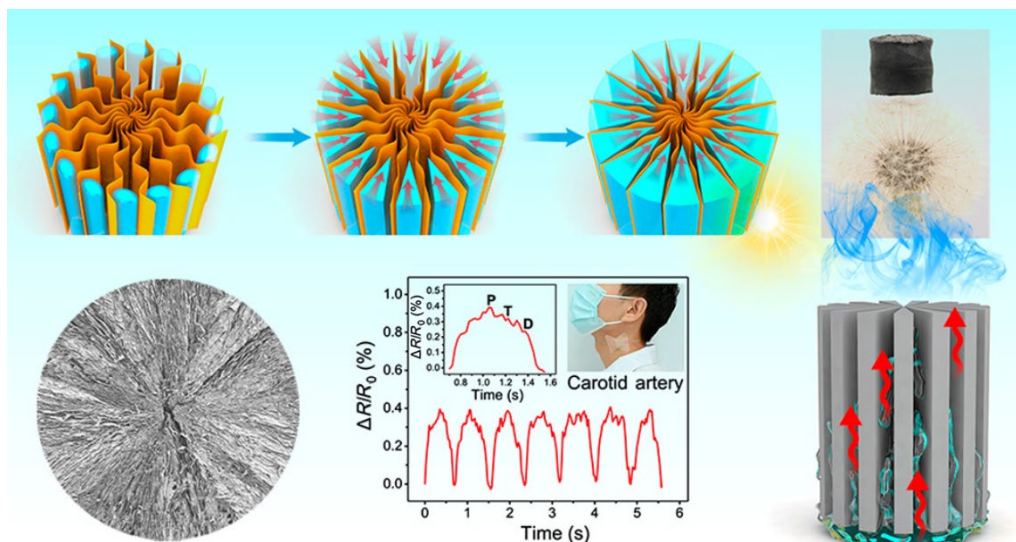
Figure 16 The MXene/polyimide aerogels-based piezoresistive sensor for human motion monitoring. The fabrication of xylem-like architecture (top). SEM image (bottom left). The sensing performance for monitoring the carotid artery (bottom middle). Demonstration of such structure for water steam collection (bottom right). Reproduced with permission from Ref. [225], © American Chemical Society 2022.

falling time (52/34 ms). Besides, the MXene composite-based electrodes can be further modified by blending nanosheets with other dispersions. It may show broad prospects for wearable electronics.

The MXene/rGO aerogel-based pressure sensor [216] shows a linear range of 0–40 kPa and a response of 61.5 kPa⁻¹, which hold promises in monitoring human health statuses, such as heartbeats, pulse, and motions. The microbridges in human skin possess high
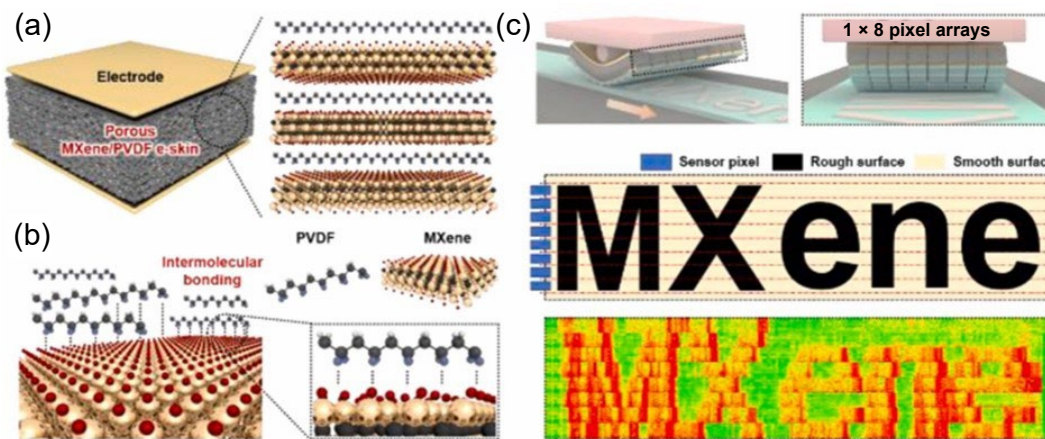
Figure 17 The individual sensors and their array based on MXene/PVDF piezoelectric membrane. (a) Scheme of the blending of MXene and PVDF for composite formation. PVDF denotes polyvinylidene fluoride. (b) The hydrogen bonds form between MXene and PVDF. (c) The MXene/PVDF sensor array for recognizing five alphabets of the word MXene. Reproduced with permission from Ref. [226], © Elsevier Ltd. 2021.
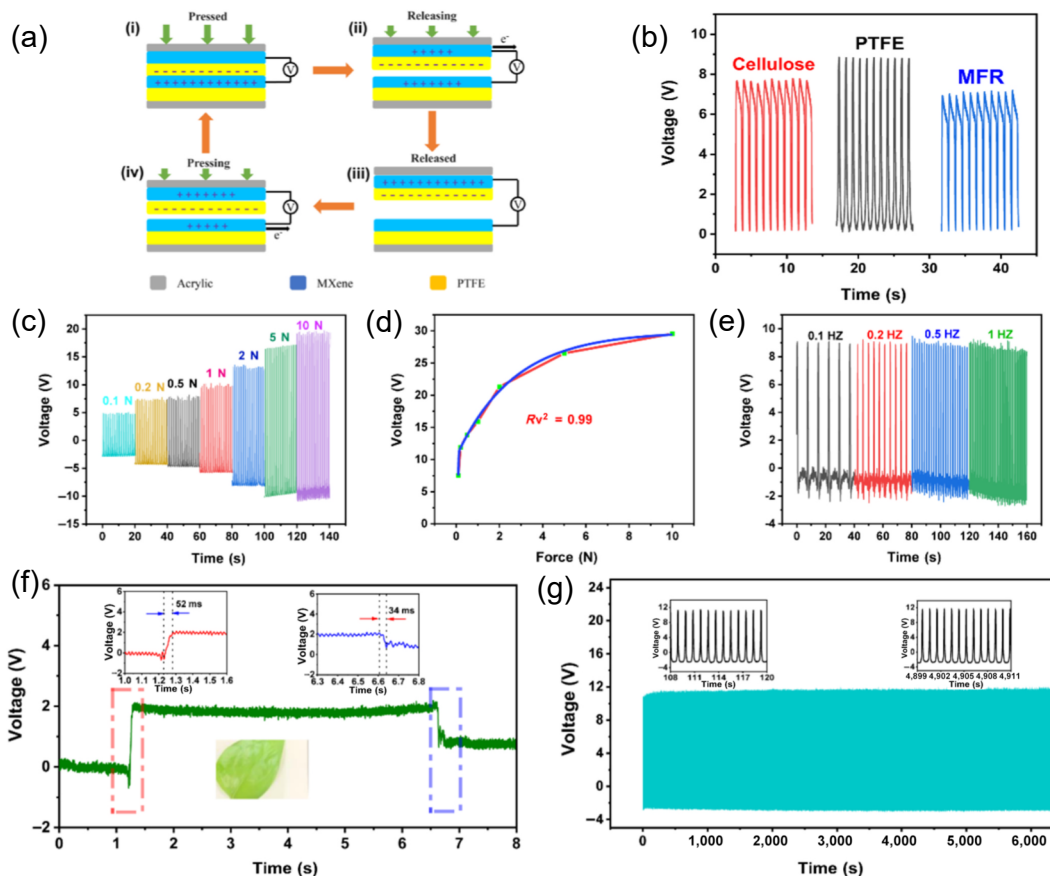
Figure 18 The MXene composite-based triboelectric nanogenerator for pressure sensor. (a) Work mechanism and (b) output voltage of three kinds of triboelectric layers. PTFE denotes polytetrafluoroethylene. MFR means mixed fiber resin. (c) Output voltage with different forces and (d) calibration of voltage versus the pressure forces. (d) Relationship of voltage output of the TENG with force change. (e) The frequency-dependent voltage response. (f) Rising and falling time of the pressure sensor. (g) Cycling test for 6,000 cycles. Reproduced with permission from Ref. [227], © Elsevier Ltd. 2021.

elastic moduli, which inspires the interlocked structure of MXene/microcapsule for pressure sensors [168]. Such an interlocked MXene composite has led to over 9-fold sensitivity compared to planar MXene-based pressure sensors. Moreover, the silk fibroin was employed as a template for crosslinking the MXene nanosheets into macroform [212]. Such a composite-based pressure sensor shows a low limit of detection (9.8 Pa) and high retention after 3,500 cycles. Indeed, the blends of MXene with polymers [211, 213] become essential strategies for designing high-performance pressure-sensing materials.

Biodegradable electronics reduce the quantity of solid waste in the environment [228, 229], termed green materials, and green production techniques [230]. The bioresorbable [231–233], bioabsorbable devices [234, 235], and transient electronics [236], may satisfy the *in vivo*-friendly requirements for implantable clinical applications [237]. Biodegradable devices consist of substrates and functional electronic components of different conductivity. For example, poly(vinylidene fluoride-co-hexafluoropropylene) (P(VDF-HFP)) serves as conducting gate electrodes in top-gated transistors [238]. Often, one can choose biodegradable polymers, plant-derived biomass [239], natural wax [240], silk fibroin [241, 242], and chitosan [243] as supporting substrates for hosting device fabrication.

Besides, the active composite layer consists of conductive polymers [244] and additive materials such as MXene [245, 246],
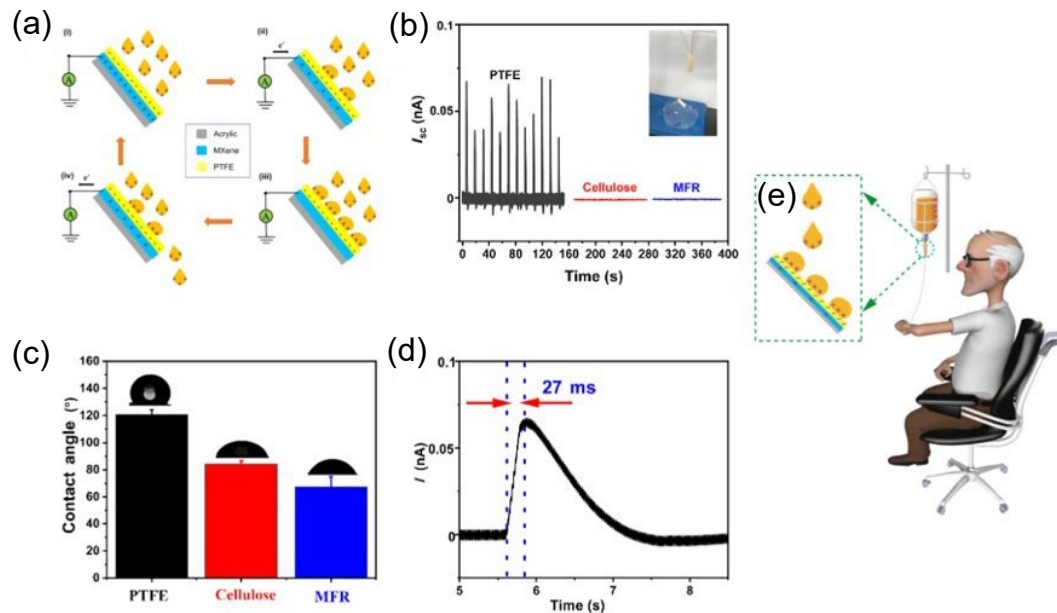
Figure 19 The MXene-PEDOT:PSS/PTFE-based triboelectric nanogenerators as pressure sensors for healthcare monitoring. (a) Single electrode work mode for TENG. TENG denotes triboelectric nanogenerators. PEDOT denotes poly(3,4-ethylenedioxythiophene). PSS denotes poly(styrenesulfonate). (b) Output current and (c) the contact angle of different triboelectric layers when immersing in water in a single electrode mode. (d) The current response curve for one individual droplet contacting and separating from the surface of MXene composite. (e) The remote monitoring of the drop counter during infusion for aging people. Here, a series of water droplets continue falling to and sliding away from the sensor. Reproduced with permission from Ref. [227], © Elsevier Ltd. 2021.

graphene [247–250], and other low-dimensional carbon nanostructures [251–253]. One can investigate the potential of biodegradation in additives and dielectrics [254, 255].

We listed the biodegradation behaviors of some polymers as examples. The poly(vinyl alcohol) (PVA) and poly(3,4-ethylenedioxythiophene)-poly(styrenesulfonate) (PEDOT:PSS) show outstanding biocompatibility with animal skins and degradability in deionized water [256]. Besides, the polysaccharides [257] can be used as matrix for hosting the composite formation. The polyvinylidene difluoride (PVDF)/polycaprolactone (PCL) blends could enhance the biodegradation of pure PVDF [258, 259]. The polylactic acid (PLA)/polybutylene adipate terephthalate (PBAT) blends demonstrate full biodegradable capability [260].

In addition, self-healing [261] becomes a prerequisite feature for polymeric building blocks for wearable electronics. In the future, one needs to develop lab-to-fab potentials for the mass production of stretchable electronics in materials preparation [262].

The self-powering of electronic devices become emerging topics promoted by MXene-based energy storage. To date, the MXene-based new gadgets such as batteries [263–266] and supercapacitors [267] remain individual prototypes in the lab [268], viz., no commercial widgets are available in portable electronic devices such as smartphones and tablets. Indeed, the on-chip micro-supercapacitors [269] facilitate the powering of miniaturized sensors but with a low technological readiness level [270, 271] due to the limited efficient volume and package issues.

The technology readiness level of MXene-based composite and energy devices can be estimated as 1–2 [272]. It may take another ten years to achieve the technological maturity of MXene.

In the forthcoming decade, the community should tackle several technological issues. First, the shortening of charging time of batteries [273–275] and supercapacitors should exceed the conventional anode materials of graphite. Besides, the supercapacitors [276] are typically applied in the uphill climbing stage in an electric vehicle, and the batteries [277] are dominant power sources for motion on flat ground. When supercapacitors possess a high energy density comparable to a battery [278],

supercapacitors may play a more important role in electric vehicles.

Besides, the wafer-scale production of micro-supercapacitor remains low in technological readiness level [279]. Similarly, clean electricity can be generated by the reduction of carbon dioxide [280, 281], hydropower [282], and solar cells [283]. Second, the production cost should be reduced to less than the graphite. The MXenes have demonstrated successes in laboratory production, i.e., 50 g MAX transformed to MXene per batch in a 60 mL container [284]. The MXene nanosheets are as high quality as in a minimized synthesis protocol, i.e., 5 g per batch.

Third, incorporating MXene nanosheets into the yarns may push the textile electronics forward, including the core–sheath structure [285] of MXene-based capacitors. Here, the robust electrical contact inside a device and between the series and parallel connected device cascades remains challenging. Indeed, the stretching and strain can easily induce the deformation and breakage of the MXene-based composite electrodes, which causes electrical disconnect and device failure. Besides, the MXene plays the role of separation membrane [286] for the adsorption of the toxins in blood [287, 288], which may regenerate the dialysate and eventually lead to a wearable kidney.

Fourth, integrating MXene-based displays with triboelectric nanogenerators may facilitate self-powered electroluminescence [219, 289]. In addition, the electromagnetic shielding film [290] may be the first real-world product based on MXenes, which can suppress the interference of two adjacent microphones.

The sensors often require a battery for continuous operation. Wearable electronics [291], including implantable devices [292], demand lightweight and self-powering, i.e., without an external power supply. Indeed, the integration of pressure sensor with micro-supercapacitors [293, 294] and photovoltaic devices [295, 296] has shown energy storage of solar energy [297] for self-powering of sensor operation [298]. Here, MXene can promote the performances of the solar cell as a charge transport layer [299] and suppress the dendrite formation in batteries [300] as an electrolyte additive [301]. The lithium-ion batteries [302] and zinc-ion batteries [303] can connect with energy production units [304–307]. The nanogenerators themselves can serve as biosensors

[308]. Programmed macrostructures have enriched the choice of flexible sensors [309].

The data retention can be extended with the assistance of resistive random access memory [310] and neuromorphic computing [311]. Indeed, the interfaces could be built between data acquisition [312] (at electronic skins) and transmission to processing devices (for computing).

7 Actuators for artificial reflex

Simulating human perception and responding to stimuli is a fundamental challenge for bionic robots and neural prosthetics. Actuators for artificial reflex enable the perception of light, heat, and electricity and convert various signals into chemical or physical signals to complete the expected reflections.

Lee et al. proposed an MXene/cellulose bilayer heterostructure for a near-infrared irradiation-induced actuator [313]. Inspired by the leaf, the palisade mesophyll expands and shrinks upon water incorporation with a vein as robust support to retain structural stability. The polycarbonate filter supports the membrane formation by vacuum filtering the ink of MXene/cellulose blends (Fig. 20).

The sensor uses MXene nanosheets to convert light energy to thermal energy (simulating palisade mesophyll cells) to achieve thermal actuation. First, the flexibility of the sensor is achieved by constructing a biocompatible nanofiber skeleton (simulating the leaf vein skeleton). The MXene is mixed with cellulose (simulating the stratum corneum). An asymmetrical structure with polycarbonate (acting as the epidermis) achieves hygroscopic actuation. As the humidity increases, the cellulose absorbs water, which induces the shrinkage of the polymer architecture (Fig. 20).

The bending of an actuator occurs by the deformation of the polymer layer while MXene layer remains unchanged. With the thermal treatment, further deformation occurs by the interlayer spacing decreases.

First, the sensor uses MXene, and hydrophilic groups on the surface of the nanofibers can form hydrogen bonds with water. It responds to trace amounts of water of 44.4 $\mu g \cdot cm^{-2}$ by asymmetric structure and automatic bending at 10% relative humidity and improves the response speed through the porous structure of polycarbonate film. Second, the sensor can achieve bending folding under near-infrared wave illumination.

The realization of this function is mainly driven by the synergy of a large number of MXene-cellulose nanofibers. When irradiated with near-infrared light, a rapid heating up of 2.3 s of low power can be achieved. Third, according to the finite element model analysis, the volume mismatch between MXene-cellulose nanofibers and polycarbonate membranes in the near-infrared environment leads to the movement of the sensor, and as the light increases, the shrinkage increases. Fourth, the sensor can implement programmable behavior in a narrow rectangular area.

The MXene/cellulose could be tailored to two-column or three-column patterns (Fig. 21). By infrared irradiation, the MXene-based actuators experience periodical bending and recovery, which mimics the motion. Besides, the folding and unfolding of the box can be obtained. Moreover, the blooming and closure of the MXene-cellulose nanofibers to make bionic flowers by near-infrared irradiation are realized. The drive process has an energy density of 0.74 $W \cdot kg^{-1}$ and a power density of 0.92 $W \cdot kg^{-1}$.

Such MXene-based actuators lighten the display upon infrared irradiation, indicating good information encryption. The deformation upon infrared irradiation may lead to intelligent
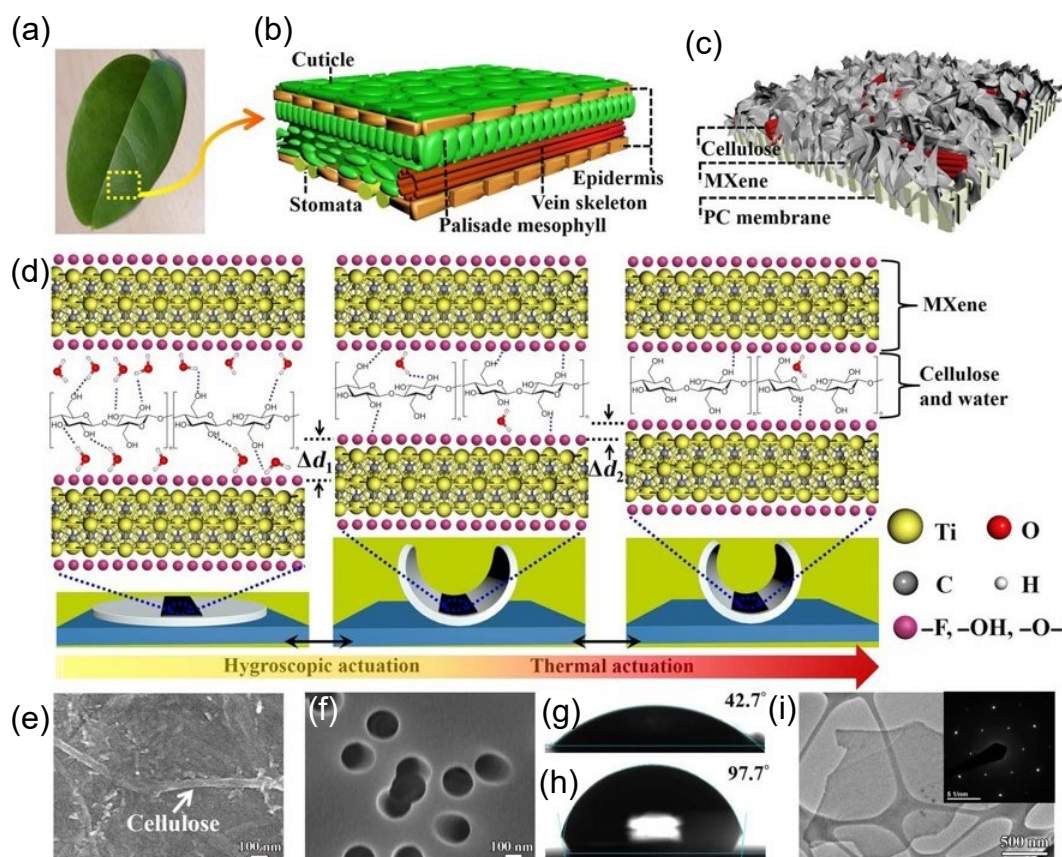
Figure 20 The MXene/cellulose-based actuator. (a) Photograph and (b) cross-section view of a sheet of a leaf. (c) Scheme of MXene/cellulose heterostructure for actuation over a polycarbonate substrate. PC denotes polycarbonate. (d) The actuation mechanism by the stimulus of water and heat. The deformation of MXene occurs upon humidity and near-infrared irradiation. SEM micrographs of (e) MXene/cellulose heterostructure and (f) polycarbonate membrane. Contact angle of (g) the heterostructure and (h) filter. (i) TEM micrograph and selected area electron diffraction (SAED) pattern of an MXene nanosheet. Reproduced with permission from Ref. [313], © Cai, G. F. et al. 2019.
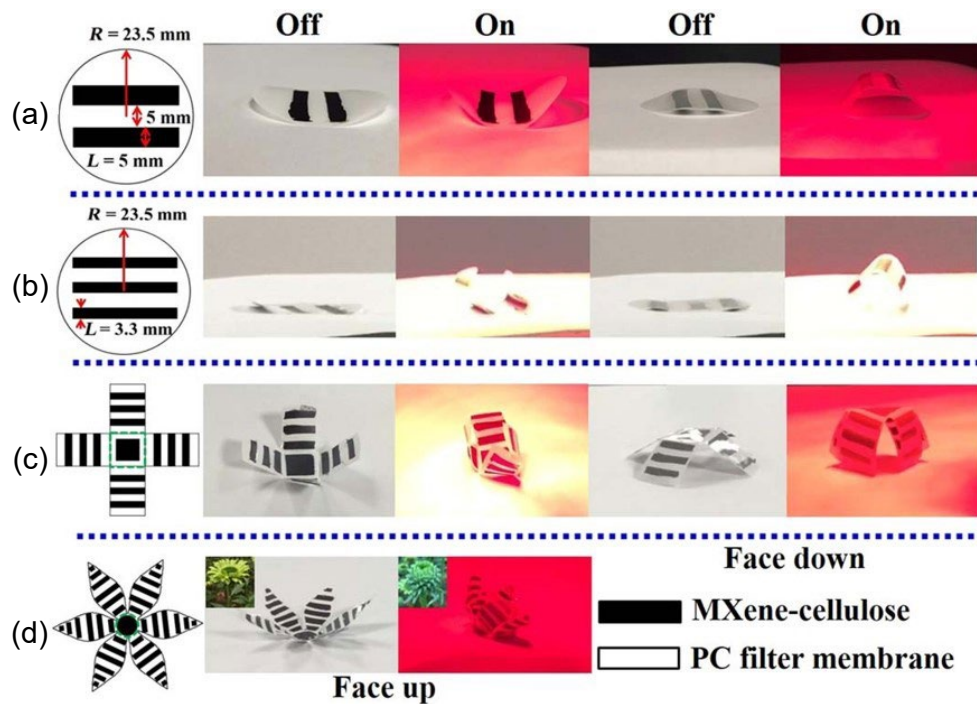
Figure 21 The MXene/cellulose-based actuators for controllable motion with different shapes (a) U, (b) arch, (c) box, and (d) bloom. These actuators continue to bend and recover for sliding motion and box folding and blooming during the periodical switching on and off near-infrared illumination. Reproduced with permission from Ref. [313], © Cai, G. F. et al. 2019.

switches of night light. They also demonstrate the possibilities of application in the haptics.

The human-like sensors and actuators have demonstrated excellent potential in future applications. First, artificial prosthetics [314, 315] possesses huge markets, which is a system-level product that integrates tactile sensors (often termed electronic skins), temperature and humidity sensors [316], and interfaces [317]. The tactile sensor arrays [318] facilitate the imaging of palmprint [319].

And artificial muscles employ the concept of actuators. Second, the current service robotics remain machine-like and not ideal for human interaction, i.e., a shortage of human-like bending and stretching. Therefore, intelligent sensors and actuators will boost the actuate machine vision [320] and speed of sensing tiny objects and elevate actuation performances [321] with delicate displacement and small forces. Future service robotics may mimic human perception [322] and respond more vividly. Third, human-machine interfaces arouse next-generation consumer electronics.

The metaverse-based electronic products and networking incorporate intelligent headsets, virtual reality [323], brain–machine interfacing [324], virtual community, flexible displays, three-dimensional vision, sixth-generation wireless systems [325], and the internet of things. Fourth, smart cities [326] may exploit intelligent sensors, innovative construction materials, smart switches based on actuators, the internet of everything, big data, and cloud computing. Human-like sensors and actuators have a bright future for evolving technological developments and growing huge markets.

8 Conclusion and future opportunities

This review provides the most recent advances in MXene-based sensors that demonstrate the fundamental functions of human-like five senses and the actuators that serve as artificial muscles. First, the artificial retina based on MXene has been discussed for image pattern recognition. Second, the MXene-based gas sensors cover the detection of several representative gases, including methanol (biomass-derived fuel), volatile organic gases, including toluene (hazardous in vehicles and indoor decoration), and

acetone as biomarkers of diabetes. Third, the taste sense has been achieved by detecting the chemicals in food that produces the gustation, such as L-glutamate (in monosodium glutamate), inosine monophosphate (in meat), and capsaicin (in spicy dishes). Then, the acoustic devices are discussed, including artificial eardrums, loudspeakers, microphones, and sound generators. In addition, the four types of pressure sensors are outlined based on MXene electrodes and sensitive materials. Eventually, the MXene-based actuators were conveyed in response to humidity, light irradiation, and magnetic field.

MXene-based semiconductors are still in their infant stage, investigating physical properties and device performances. First is the material properties. The saturable absorber properties of MXenes [327–329] have been employed for applications of pulsed laser [330, 331], soliton pulses [332], optical modulators [333–335], wavelength conversion [336], and integrated photonic circuits [103, 337, 338]. Besides, MXenes have been incorporated into optoelectronic devices such as photovoltaic cells [91, 339] and photodetectors [23, 97] as carrier transport layers and heterojunction contact [24].

However, drawbacks remain to be solved for electronic applications of MXenes. For example, pristine MXene demonstrates low flexibility [340], oxidization-driven degradation [341], and aggregation-induced precipitation [342].

But the fundamental physics behind remains less known, i.e., carrier relation [343] and ultrafast dynamics [344], bandgap manipulation, and the conductivity-regulating mechanism. The investigation of the model MXene of $Ti_3C_2T_x$ is relatively extensive [98, 345], covering its conductivity and optical properties [346]. However, challenges remain for other types of MXenes [347] that have been less explored for both synthesis and properties. Hence, more efforts should investigate the semiconducting behaviors of MXenes by experimentally regulating their different types and amounts of terminational groups and theoretically predicting optical properties [348].

Great opportunities remain in exploring properties' fundamentals in theoretical [49, 348] and experimental

approaches [349, 350]. The MXene investigation continues to elevate the mechanical strength performances [351], electrochemical [352–354], catalytic [355–359], superconducting [360], magnetic properties, ultrafast photonics [329, 343, 344, 347], and other condensed matter physics. The structure–property relationship could be unveiled by scanning probe microscopy [361]. The MXene-based electrodes for zinc batteries [362–365] show promising low cost and high energy storage density. Besides, the MXene-based electromagnetic shielding [366, 367], including infrared shielding [368], continues to break its record performance [369, 370]. The field-effect mobility that explores the semiconducting behaviors of MXenes continues to grow. Indeed, the gate voltage regulating conductivity may promote the gas sensing performances by the signal magnification through the transconductance from voltage to current at the channel materials. Indeed, the bandgap engineering of MXenes for thermoelectric power generation [371–373] is worth investigating.

The synthesis of MXenes continues to evolute in both dry and wet conditions. First, substituting elements in MXenes leads to forming new compounds [374, 375]. More efforts should be put into the controlled direct thermal deposition synthesis of MXene film over a wafer scale. Indeed, compound structures [376, 377] analogous to MXene have been synthesized by chemical vapor deposition. Second, the solution processing of MXene [92] becomes promising for mass production of nanosheets in dispersions [378]. The MXene quantum dots [100] are efficient photoluminescent materials for near-infrared images [108]. Besides, the long-term stability of MXene-based aqueous solutions or dispersion could be improved by polymer hybridization [379] and surface engineering [93, 378] without oxidation [95]. Indeed, printed electronics require the long durability of MXene-based inks [119] for reducing manufacturing costs and maintaining the uniformity of fabricated films. In addition, the MXene-based heterostructures [96, 380, 381] or composites [87, 382] continue to expand the knowledge boundaries. The morphologies of hydrogel [125] and aerogel may elevate their mechanical and electrical performances.

Regarding the synthesis of MXene-based semiconductors, there is a lot of room to fill in between the ideal MXene materials and the currently available status. The MXene of different morphologies [96, 98] will continue to evolve, aiming at the improved homogeneity of quantum dots, nanosheets, monolayer film, and thick membranes. Further developments are needed to optimize the stability of MXene nanosheets [383] and the homogeneity of nanosheet size and thickness. For the ultimate goal of MXenes, their terminational groups could be precisely manipulated, i.e., controllable fluorination [94], in the means of the density and the location of the MXene. The substitution of X element may induce novel phenomena [384]. The yield of MXene can be elevated during the etching and rinsing of nanosheets. More possibilities of heterostructures occur when coupling the MXene with different functional materials.

The MXene-based devices are mainly designed for individual functions, e.g., sensors [97, 385], memories or data processors, and power units such as batteries and supercapacitors [386]. First, the individual device should break the theoretical limit for higher performances [387]. The integration of microfluidic chips and chemiresistor results in biosensors of good selectivity [120]. The Internet of Things era [388, 389] requires high integration density of devices for lightweight, portable [390], and wearable electronics [391, 392]. A few emerging devices and components have achieved dual functions by integrating two devices: temperature and humidity sensors, nanogenerators and supercapacitors for self-powering, triboelectric nanogenerators for self-powered sensing, and humidity sensors and actuators. Indeed, the integration of supercapacitors [393] with logic devices leads to self-powering and self-charging [394]. More innovations may turn in for enriching the device design and fabrication.

The sensing-memory-computing in one remains challenging and requires more effort to push forwards. First, the memristor keeps boosting its performance as memory [395, 396]. The in-sensor memory [397, 398] and neuromorphic signal transmission have shown the integration of two functional devices [399]. Indeed, brain-like neuromorphic computing based on memristors is an emerging hot topic for elevating artificial data processing [400]. The MXene-based memristors and synapses [401] are still in their infancy. The system-level integration [402] requires the compromise of devices, hardware, algorithm, and interfaces.

The MXenes have shown great promise in biomedical applications [97, 101], including sensing [119–121], diagnosis [99], imaging [403], drug delivery [404], and photothermal therapy [405, 406]. Besides, the evaluation of biocompatibility [407] and biosafety [408] remains essential before clinic applications. Moreover, the antibacterial performances have been reported by photocatalytic charge transfer mechanism [409, 410]. In addition, the MXene matrix can host tissue regeneration [411] and promote cancer immunotherapy [412]. Integrating electrochemical sensors [119] with a microfluidic chip [120] would guarantee the feasible detection of individual cells or miRNA molecules. The MXene-based heterostructure may demonstrate the synergistic effect when coupling with other low-dimensional materials [413–417], which may improve biomedical performances. Overall, MXene has become an important candidate material for biomedicine experiments.

MXene may eventually turn up in clinical applications after long-term mature surgery over animal models [418–421]. For example, the decoration of MXene by DOXjade groups [405] can employ the accumulation and localization of MXene nanosheets in tumor tissue, in which DOXjade liberates and serves for chemotherapy of tumors. However, the operation mechanism of MXene-based drug delivery and biomedicine has not yet been clarified. Efforts should be taken to achieve the *in vivo* release and biodegradation [422] after completing its role of therapy inside human bodies. Therefore, a more focused investigation on the reliability and robustness of MXene could promote its clinical applications.

Humanoid robotics remain the ultimate goal of artificial intelligence. Indeed, humanoids could be assembled by connecting various sensors and motors (actuators) for mimicking human behaviors such as speech, interactive dialogues, accompanying, and nursing. The wearable smart glasses and metaverse have driven the displays for virtual reality in healthcare and accompanying applications. Soft robotics based on MXene actuators [423] may provide efficient solutions for an artificial limb.

In sum, tremendous opportunities remain in MXene-related research, including materials synthesis, properties, device performances, and intelligent integrated systems composed of multiple interconnecting devices and their communications.

Acknowledgments

References

[1] Du, Z. G.; Yang, S. B.; Li, S. M.; Lou, J.; Zhang, S. Q.; Wang, S.; Li, B.; Gong, Y. J.; Song, L.; Zou, X. L. et al. Conversion of non-van der Waals solids to 2D transition-metal chalcogenides. *Nature* **2020**, *577*, 492–496.

[2] Xia, Y.; Mathis, T. S.; Zhao, M. Q.; Anasori, B.; Dang, A. L.; Zhou, Z. H.; Cho, H.; Gogotsi, Y.; Yang, S. Thickness-independent capacitance of vertically aligned liquid-crystalline MXenes. *Nature* **2018**, *557*, 409–412.

[3] Iqbal, A.; Shahzad, F.; Hantanasirisakul, K.; Kim, M. K.; Kwon, J.; Hong, J.; Kim, H.; Kim, D.; Gogotsi, Y.; Koo, C. M. Anomalous absorption of electromagnetic waves by 2D transition metal carbonitride Ti_3CNT_x (MXene). *Science* **2020**, *369*, 446–450.

[4] Kamysbayev, V.; Filatov, A. S.; Hu, H. C.; Rui, X.; Lagunas, F.; Wang, D.; Klie, R. F.; Talapin, D. V. Covalent surface modifications and superconductivity of two-dimensional metal carbide MXenes. *Science* **2020**, *369*, 979–983.

[5] Naguib, M.; Barsoum, M. W.; Gogotsi, Y. Ten years of progress in the synthesis and development of MXenes. *Adv. Mater.* **2021**, *33*, 2103393.

[6] Naguib, M.; Kurtoglu, M.; Presser, V.; Lu, J.; Niu, J. J.; Heon, M.; Hultman, L.; Gogotsi, Y.; Barsoum, M. W. Two-dimensional nanocrystals produced by exfoliation of Ti_3AlC_2. *Adv. Mater.* **2011**, *23*, 4248–4253.

[7] VahidMohammadi, A.; Rosen, J.; Gogotsi, Y. The world of two-dimensional carbides and nitrides (MXenes). *Science* **2021**, *372*, eabf1581.

[8] Malaki, M.; Varma, R. S. Mechanotribological aspects of MXene-reinforced nanocomposites. *Adv. Mater.* **2020**, *32*, 2003154.

[9] Zhou, T. Z.; Wu, C.; Wang, Y. L.; Tomsia, A. P.; Li, M. Z.; Saiz, E.; Fang, S. L.; Baughman, R. H.; Jiang, L.; Cheng, Q. F. Super-tough MXene-functionalized graphene sheets. *Nat. Commun.* **2020**, *11*, 2077.

[10] Lipatov, A.; Goad, A.; Loes, M. J.; Vorobeva, N. S.; Abourahma, J.; Gogotsi, Y.; Sinitskii, A. High electrical conductivity and breakdown current density of individual monolayer $Ti_3C_2T_x$ MXene flakes. *Matter* **2021**, *4*, 1413–1427.

[11] Ling, Z.; Ren, C. E.; Zhao, M. Q.; Yang, J.; Giammarco, J. M.; Qiu, J. S.; Barsoum, M. W.; Gogotsi, Y. Flexible and conductive MXene films and nanocomposites with high capacitance. *Proc. Natl. Acad. Sci. USA* **2014**, *111*, 16676–16681.

[12] Dong, Y. C.; Chertopalov, S.; Maleski, K.; Anasori, B.; Hu, L. Y.; Bhattacharya, S.; Rao, A. M.; Gogotsi, Y.; Mochalin, V. N.; Podila, R. Saturable absorption in 2D Ti_3C_2 MXene thin films for passive photonic diodes. *Adv. Mater.* **2018**, *30*, 1705714.

[13] Jeon, J.; Yang, Y. J.; Choi, H.; Park, J. H.; Lee, B. H.; Lee, S. MXenes for future nanophotonic device applications. *Nanophotonics* **2020**, *9*, 1831–1853.

[14] Khazaei, M.; Arai, M.; Sasaki, T.; Chung, C. Y.; Venkataramanan, N. S.; Estili, M.; Sakka, Y.; Kawazoe, Y. Novel electronic and magnetic properties of two-dimensional transition metal carbides and nitrides. *Adv. Funct. Mater.* **2013**, *23*, 2185–2192.

[15] Iqbal, M.; Fatheema, J.; Noor, Q.; Rani, M.; Mumtaz, M.; Zheng, R. K.; Khan, S. A.; Rizwan, S. Co-existence of magnetic phases in two-dimensional MXene. *Mater. Today Chem.* **2020**, *16*, 100271.

[16] Li, R. S.; Gao, Q.; Xing, H. N.; Su, Y. Z.; Zhang, H. M.; Zeng, D.; Fan, B. B.; Zhao, B. Lightweight, multifunctional MXene/polymer composites with enhanced electromagnetic wave absorption and high-performance thermal conductivity. *Carbon* **2021**, *183*, 301–312.

[17] Luo, Y.; Xie, Y. H.; Jiang, H.; Chen, Y.; Zhang, L.; Sheng, X. X.; Xie, D. L.; Wu, H.; Mei, Y. Flame-retardant and form-stable phase change composites based on MXene with high thermostability and thermal conductivity for thermal energy storage. *Chem. Eng. J.* **2021**, *420*, 130466.

[18] Zhao, S.; Zhang, H. B.; Luo, J. Q.; Wang, Q. W.; Xu, B.; Hong, S.; Yu, Z. Z. Highly electrically conductive three-dimensional $Ti_3C_2T_x$ MXene/reduced graphene oxide hybrid aerogels with excellent electromagnetic interference shielding performances. *ACS Nano* **2018**, *12*, 11193–11202.

[19] Shahzad, F.; Alhabeb, M.; Hatter, C. B.; Anasori, B.; Hong, S. M.; Koo, C. M.; Gogotsi, Y. Electromagnetic interference shielding with 2D transition metal carbides (MXenes). *Science* **2016**, *353*, 1137–1140.

[20] Naguib, M.; Mochalin, V. N.; Barsoum, M. W.; Gogotsi, Y. 25th anniversary article: MXenes: A new family of two-dimensional materials. *Adv. Mater.* **2014**, *26*, 992–1005.

[21] Zhang, J. Z.; Kong, N.; Uzun, S.; Levitt, A.; Seyedin, S.; Lynch, P. A.; Qin, S.; Han, M. K.; Yang, W. R.; Liu, J. Q. et al. Scalable manufacturing of free-standing, strong $Ti_3C_2T_x$ MXene films with outstanding conductivity. *Adv. Mater.* **2020**, *32*, 2001093.

[22] Chen, R. S.; Ding, G. L.; Feng, Z. H.; Zhang, S. R.; Mo, W. A.; Han, S. T.; Zhou, Y. MoS_2 transistor with weak fermi level pinning via MXene contacts. *Adv. Funct. Mater.* **2022**, *32*, 2204288.

[23] Gao, L. F.; Ma, C. Y.; Wei, S. R.; Kuklin, A. V.; Zhang, H.; Ågren, H. Applications of few-layer Nb_2C MXene: Narrow-band photodetectors and femtosecond mode-locked fiber lasers. *ACS Nano* **2021**, *15*, 954–965.

[24] Zhang, Y.; Xu, Y.; Gao, L.; Liu, X.; Fu, Y.; Ma, C.; Ge, Y.; Cao, R.; Zhang, X.; Al-Hartomy, O. A. et al. MXene-based mixed-dimensional Schottky heterojunction towards self-powered flexible high-performance photodetector. *Mater. Today Phys.* **2021**, *21*, 100479.

[25] Agresti, A.; Pazniak, A.; Pescetelli, S.; Di Vito, A.; Rossi, D.; Pecchia, A.; Der Maur, M. A.; Liedl, A.; Larciprete, R.; Kuznetsov, D. V. et al. Titanium-carbide MXenes for work function and interface engineering in perovskite solar cells. *Nat. Mater.* **2019**, *18*, 1228–1234.

[26] Fu, B.; Sun, J. X.; Wang, C.; Shang, C.; Xu, L. J.; Li, J. B.; Zhang, H. MXenes: Synthesis, optical properties, and applications in ultrafast photonics. *Small* **2021**, *17*, 2006054.

[27] Kim, H.; Wang, Z. W.; Alshareef, H. N. MXetronics: Electronic and photonic applications of MXenes. *Nano Energy* **2019**, *60*, 179–197.

[28] Jin, X. X.; Wang, J. F.; Dai, L. Z.; Liu, X. Y.; Li, L.; Yang, Y. Y.; Cao, Y. X.; Wang, W. J.; Wu, H.; Guo, S. Y. Flame-retardant poly(vinyl alcohol)/MXene multilayered films with outstanding electromagnetic interference shielding and thermal conductive performances. *Chem. Eng. J.* **2020**, *380*, 122475.

[29] Siriwardane, E. M. D.; Karki, P.; Loh, Y. L.; Çakır, D. Strain-spintronics: Modulating electronic and magnetic properties of Hf$_2$MnC$_2$O$_2$ MXene by uniaxial strain. *J. Phys. Chem. C* **2019**, *123*, 12451–12459.

[30] Kim, H.; Alshareef, H. N. MXetronics: MXene-enabled electronic and photonic devices. *ACS Materials Lett.* **2020**, *2*, 55–70.

[31] Zhang, J. Q.; Zhao, Y. F.; Guo, X.; Chen, C.; Dong, C. L.; Liu, R. S.; Han, C. P.; Li, Y. D.; Gogotsi, Y.; Wang, G. X. Single platinum atoms immobilized on an MXene as an efficient catalyst for the hydrogen evolution reaction. *Nat. Catal.* **2018**, *1*, 985–992.

[32] Palankar, R. Microrobots mop-up nanoplastics. *Nat. Nanotechnol.* **2022**, *17*, 821.

[33] Liu, S. Y.; Liu, J. Y.; Liu, X. F.; Shang, J. X.; Xu, L.; Yu, R. H.; Shui, J. L. Hydrogen storage in incompletely etched multilayer Ti$_2$CT$_x$ at room temperature. *Nat. Nanotechnol.* **2021**, *16*, 331–336.

[34] Wu, F.; Zheng, H. L.; Wang, W. Z.; Wu, Q.; Zhang, Q.; Guo, J. Y.; Pu, B. Z.; Shi, X. Y.; Li, J. B.; Chen, X. M. et al. Rapid eradication of antibiotic-resistant bacteria and biofilms by MXene and near-infrared light through photothermal ablation. *Sci. Chin. Mater.* **2020**, *64*, 748–758.

[35] Sun, L. Y.; Fan, L.; Bian, F. K.; Chen, G. P.; Wang, Y. T.; Zhao, Y. J. MXene-integrated microneedle patches with innate molecule encapsulation for wound healing. *Research (Wash. D C)* **2021**, *2021*, 9838490.

[36] Li, X. L.; Li, M.; Yang, Q.; Wang, D. H.; Ma, L. T.; Liang, G. J.; Huang, Z. D.; Dong, B. B.; Huang, Q.; Zhi, C. Y. Vertically aligned Sn^{4+} preintercalated Ti$_2$CT$_x$ MXene sphere with enhanced Zn ion transportation and superior cycle lifespan. *Adv. Energy Mater.* **2020**, *10*, 2001394.

[37] Li, M.; Li, X. L.; Qin, G. F.; Luo, K.; Lu, J.; Li, Y. B.; Liang, G. J.; Huang, Z. D.; Zhou, J.; Hultman, L. et al. Halogenated Ti$_3$C$_2$ MXenes with electrochemically active terminals for high-performance zinc ion batteries. *ACS Nano* **2021**, *15*, 1077–1085.

[38] Wang, J. J.; Du, C. F.; Xue, Y. Q.; Tan, X. Y.; Kang, J. Z.; Gao, Y.; Yu, H.; Yan, Q. Y. MXenes as a versatile platform for reactive surface modification and superior sodium-ion storages. *Exploration* **2021**, *1*, 20210024.

[39] Peng, S. A.; Jin, Z.; Zhang, D. Y.; Shi, J. Y.; Mao, D. C.; Wang, S. Q.; Yu, G. H. Carrier-number-fluctuation induced ultralow 1/*f* noise level in top-gated graphene field effect transistor. *ACS Appl. Mater. Interfaces* **2017**, *9*, 6661–6665.

[40] Peng, S. A.; Jin, Z.; Zhang, D. Y.; Shi, J. Y.; Niu, J. B.; Huang, X. N.; Yao, Y.; Zhang, Y. H.; Yu, G. H. How do contact and channel contribute to the dirac points in graphene field-effect transistors? *Adv. Electron. Mater.* **2018**, *4*, 1800158.

[41] Peng, S. A.; Jin, Z.; Zhang, D. Y.; Shi, J. Y.; Zhang, Y. H.; Yu, G. H. Evidence of electric field-tunable tunneling probability in graphene and metal contact. *Nanoscale* **2017**, *9*, 9520–9528.

[42] Peng, S. A.; Jin, Z.; Yao, Y.; Li, L.; Zhang, D. Y.; Shi, J. Y.; Huang, X. N.; Niu, J. B.; Zhang, Y. H.; Yu, G. H. Metal-contact-induced transition of electrical transport in monolayer MoS$_2$: From thermally activated to variable-range hopping. *Adv. Electron. Mater.* **2019**, *5*, 1900042.

[43] Peng, S. A.; Zhang, J.; Jin, Z.; Zhang, D. Y.; Shi, J. Y.; Wei, S. H. Electric-field induced doping polarity conversion in top-gated transistor based on chemical vapor deposition of graphene. *Crystals* **2022**, *12*, 184.

[44] Peng, S. A.; Jin, Z.; Yao, Y.; Huang, X. N.; Zhang, D. Y.; Niu, J. B.; Shi, J. Y.; Zhang, Y. H.; Yu, G. H. Controllable p-to-n type conductance transition in top-gated graphene field effect transistor by interface trap engineering. *Adv. Electron. Mater.* **2020**, *6*, 2000496.

[45] Peng, S. A.; Jin, Z.; Zhang, D. Y.; Shi, J. Y.; Niu, J. B.; Zhu, C. Y.;

[46] Zhang, Y. H.; Yu, G. H. The effect of metal contact doping on the scaled graphene field effect transistor. *Adv. Eng. Mater.* **2022**, *24*, 2100935.

[46] Chaudhuri, K.; Alhabeb, M.; Wang, Z. X.; Shalaev, V. M.; Gogotsi, Y.; Boltasseva, A. Highly broadband absorber using plasmonic titanium carbide (MXene). *ACS Photonics* **2018**, *5*, 1115–1122.

[47] Hantanasirisakul, K.; Zhao, M. Q.; Urbankowski, P.; Halim, J.; Anasori, B.; Kota, S.; Ren, C. E.; Barsoum, M. W.; Gogotsi, Y. Fabrication of Ti$_3$C$_2$T$_x$ MXene transparent thin films with tunable optoelectronic properties. *Adv. Electron. Mater.* **2016**, *2*, 1600050.

[48] Guo, J. X.; Sun, Y.; Liu, B. Z.; Zhang, Q. R.; Peng, Q. M. Two-dimensional scandium-based carbides (MXene): Band gap modulation and optical properties. *J. Alloys Compd.* **2017**, *712*, 752–759.

[49] Hantanasirisakul, K.; Gogotsi, Y. Electronic and optical properties of 2D transition metal carbides and nitrides (MXenes). *Adv. Mater.* **2018**, *30*, 1804779.

[50] Bao, Q. L.; Zhang, H.; Wang, Y.; Ni, Z. H.; Yan, Y. L.; Shen, Z. X.; Loh, K. P.; Tang, D. Y. Atomic-layer graphene as a saturable absorber for ultrafast pulsed lasers. *Adv. Funct. Mater.* **2009**, *19*, 3077–3083.

[51] Wang, T. H.; Zhu, Y. F.; Jiang, Q. Bandgap opening of bilayer graphene by dual doping from organic molecule and substrate. *J. Phys. Chem. C* **2013**, *117*, 12873–12881.

[52] Carvalho, A.; Wang, M.; Zhu, X.; Rodin, A. S.; Su, H. B.; Neto, A. H. C. Phosphorene: From theory to applications. *Nat. Rev. Mater.* **2016**, *1*, 16061.

[53] Hu, G. H.; Albrow-Owen, T.; Jin, X. X.; Ali, A.; Hu, Y. W.; Howe, R. C. T.; Shehzad, K.; Yang, Z. Y.; Zhu, X. K.; Woodward, R. I. et al. Black phosphorus ink formulation for inkjet printing of optoelectronics and photonics. *Nat. Commun.* **2017**, *8*, 278.

[54] Lu, S. B.; Miao, L. L.; Guo, Z. N.; Qi, X.; Zhao, C. J.; Zhang, H.; Wen, S. C.; Tang, D. Y.; Fan, D. Y. Broadband nonlinear optical response in multi-layer black phosphorus: An emerging infrared and mid-infrared optical material. *Opt. Express* **2015**, *23*, 11183–11194.

[55] Luo, Z. Q.; Huang, Y. Z.; Weng, J.; Cheng, H. H.; Lin, Z. Q.; Xu, B.; Cai, Z. P.; Xu, H. Y. 1.06 μm Q-switched ytterbium-doped fiber laser using few-layer topological insulator Bi$_2$Se$_3$ as a saturable absorber. *Opt. Express* **2013**, *21*, 29516–29522.

[56] Chen, C. Y.; Xie, Z. J.; Feng, Y.; Yi, H. M.; Liang, A. J.; He, S. L.; Mou, D. X.; He, J. F.; Peng, Y. Y.; Liu, X. et al. Tunable Dirac fermion dynamics in topological insulators. *Sci. Rep.* **2013**, *3*, 2411.

[57] Hajlaoui, M.; Papalazarou, E.; Mauchain, J.; Lantz, G.; Moisan, N.; Boschetto, D.; Jiang, Z.; Miotkowski, I.; Chen, Y. P.; Taleb-Ibrahimi, A. et al. Ultrafast surface carrier dynamics in the topological insulator Bi$_2$Te$_3$. *Nano Lett.* **2012**, *12*, 3532–3536.

[58] Zhang, H.; Lu, S. B.; Zheng, J.; Du, J.; Wen, S. C.; Tang, D. Y.; Loh, K. P. Molybdenum disulfide (MoS$_2$) as a broadband saturable absorber for ultra-fast photonics. *Opt. Express* **2014**, *22*, 7249–7260.

[59] Wang, Q. H.; Kalantar-Zadeh, K.; Kis, A.; Coleman, J. N.; Strano, M. S. Electronics and optoelectronics of two-dimensional transition metal dichalcogenides. *Nat. Nanotechnol.* **2012**, *7*, 699–712.

[60] Zhang, Y. X.; Wang, S. X.; Yu, H. H.; Zhang, H. J.; Chen, Y. X.; Mei, L. M.; Di Lieto, A.; Tonelli, M.; Wang, J. Y. Atomic-layer molybdenum sulfide optical modulator for visible coherent light. *Sci. Rep.* **2015**, *5*, 11342.

[61] Cui, H. P.; Zheng, K.; Xie, Z. J.; Yu, J. B.; Zhu, X. Y.; Ren, H.; Wang, Z. P.; Zhang, F.; Li, X. D.; Tao, L. Q. et al. Tellurene nanoflake-based NO$_2$ sensors with superior sensitivity and a sub-parts-per-billion detection limit. *ACS Appl. Mater. Interfaces* **2020**, *12*, 47704–47713.

[62] Wu, W. Z.; Qiu, G.; Wang, Y. X.; Wang, R. X.; Ye, P. D. Tellurene: Its physical properties, scalable nanomanufacturing, and device applications. *Chem. Soc. Rev.* **2018**, *47*, 7203–7212.

[63] Sang, D. K.; Ding, T.; Wu, M. N.; Li, Y.; Li, J. Q.; Liu, F. S.; Guo, Z. N.; Zhang, H.; Xie, H. P. Monolayer β-tellurene: A promising p-type thermoelectric material via first-principles calculations. *Nanoscale* **2019**, *11*, 18116–18123.

[64] Liu, N. N.; Bo, G. Y.; Liu, Y. N.; Xu, X.; Du, Y.; Dou, S. X.

Recent progress on germanene and functionalized germanene: Preparation, characterizations, applications, and challenges. *Small* **2019**, *15*, 1805147.

[65] Zhao, F. L.; Feng, Y. Y.; Feng, W. Germanium-based monoelemental and binary two-dimensional materials: Theoretical and experimental investigations and promising applications. *InfoMat*, in press, https://doi.org/10.1002/inf2.12365.

[66] Dávila, M. E.; Xian, L.; Cahangirov, S.; Rubio, A.; Le Lay, G. Germanene: A novel two-dimensional germanium allotrope akin to graphene and silicene. *New J. Phys.* **2014**, *16*, 095002.

[67] Kiraly, B.; Liu, X. L.; Wang, L. Q.; Zhang, Z. H.; Mannix, A. J.; Fisher, B. L.; Yakobson, B. I.; Hersam, M. C.; Guisinger, N. P. Borophene synthesis on Au(111). *ACS Nano* **2019**, *13*, 3816–3822.

[68] Tokmachev, A. M.; Averyanov, D. V.; Parfenov, O. E.; Taldenkov, A. N.; Karateev, I. A.; Sokolov, I. S.; Kondratev, O. A.; Storchak, V. G. Emerging two-dimensional ferromagnetism in silicene materials. *Nat. Commun.* **2018**, *9*, 1672.

[69] Singh, S.; Zanolli, Z.; Amsler, M.; Belhadji, B.; Sofo, J. O.; Verstraete, M. J.; Romero, A. H. Low-energy phases of bi monolayer predicted by structure search in two dimensions. *J. Phys. Chem. Lett.* **2019**, *10*, 7324–7332.

[70] Johnson, N. W.; Vogt, P.; Resta, A.; De Padova, P.; Perez, I.; Muir, D.; Kurmaev, E. Z.; Le Lay, G.; Moewes, A. The metallic nature of epitaxial silicene monolayers on Ag(111). *Adv. Funct. Mater.* **2014**, *24*, 5253–5259.

[71] Pumera, M.; Sofer, Z. 2D monoelemental arsenene, antimonene, and bismuthene: Beyond black phosphorus. *Adv. Mater.* **2017**, *29*, 1605299.

[72] Huang, Z. Y.; Liu, H. T.; Hu, R.; Qiao, H.; Wang, H. D.; Liu, Y. D.; Qi, X.; Zhang, H. Structures, properties and application of 2D monoelemental materials (Xenes) as graphene analogues under defect engineering. *Nano Today* **2020**, *35*, 100906.

[73] Gablech, I.; Pekárek, J.; Klempa, J.; Svatoš, V.; Sajedi-Moghaddam, A.; Neužil, P.; Pumera, M. Monoelemental 2D materials-based field effect transistors for sensing and biosensing: Phosphorene, antimonene, arsenene, silicene, and germanene go beyond graphene. *TrAC Trends Anal. Chem.* **2018**, *105*, 251–262.

[74] Zhou, D. C.; Li, H. P.; Si, N.; Li, H.; Fuchs, H.; Niu, T. C. Epitaxial growth of main group monoelemental 2D materials. *Adv. Funct. Mater.* **2021**, *31*, 2006997.

[75] Qiao, H.; Liu, H. T.; Huang, Z. Y.; Hu, R.; Ma, Q.; Zhong, J. X.; Qi, X. Tunable electronic and optical properties of 2D monoelemental materials beyond graphene for promising applications. *Energy Environ. Mater.* **2021**, *4*, 522–543.

[76] Zhu, F. F.; Chen, W. J.; Xu, Y.; Gao, C. L.; Guan, D. D.; Liu, C. H.; Qian, D.; Zhang, S. C.; Jia, J. F. Epitaxial growth of two-dimensional stanene. *Nat. Mater.* **2015**, *14*, 1020–1025.

[77] Dong, X.; Zhang, L. Z.; Yoon, M.; Zhang, P. P. The role of substrate on stabilizing new phases of two-dimensional tin. *2D Mater.* **2021**, *8*, 045003.

[78] Hofmann, E. V. S.; Scalise, E.; Montalenti, F.; Stock, T. J. Z.; Schofield, S. R.; Capellini, G.; Miglio, L.; Curson, N. J.; Klesse, W. M. The formation of a Sn monolayer on Ge(1 0 0) studied at the atomic scale. *Appl. Surf. Sci.* **2021**, *561*, 149961.

[79] Chen, R. B.; Chen, S. C.; Chiu, C. W.; Lin, M. F. Optical properties of monolayer tinene in electric fields. *Sci. Rep.* **2017**, *7*, 1849.

[80] Hu, Y.; Liang, J. C.; Xia, Y. R.; Zhao, C.; Jiang, M. H.; Ma, J.; Tie, Z. X.; Jin, Z. 2D arsenene and arsenic materials: Fundamental properties, preparation, and applications. *Small* **2022**, *18*, 2104556.

[81] Ye, X. J.; Zhu, G. L.; Liu, J.; Liu, C. S.; Yan, X. H. Monolayer, bilayer, and heterostructure arsenene as potential anode materials for magnesium-ion batteries: A first-principles study. *J. Phys. Chem. C* **2019**, *123*, 15777–15786.

[82] Benzidi, H.; Lakhal, M.; Garara, M.; Abdellaoui, M.; Benyoussef, A.; El Kenz, A.; Mounkachi, O. Arsenene monolayer as an outstanding anode material for (Li/Na/Mg)-ion batteries: Density functional theory. *Phys. Chem. Chem. Phys.* **2019**, *21*, 19951–19962.

[83] Shi, Z. Q.; Li, H. P.; Yuan, Q. Q.; Song, Y. H.; Lv, Y. Y.; Shi, W.; Jia, Z. Y.; Gao, L. B.; Chen, Y. B.; Zhu, W. G. et al. Van der Waals

[84] Aktürk, E.; Aktürk, O. Ü.; Ciraci, S. Single and bilayer bismuthene: Stability at high temperature and mechanical and electronic properties. *Phys. Rev. B* **2016**, *94*, 014115.

[85] Xian, L. D.; Paz, A. P.; Bianco, E.; Ajayan, P. M.; Rubio, A. Square selenene and tellurene: Novel group VI elemental 2D materials with nontrivial topological properties. *2D Mater.* **2017**, *4*, 041003.

[86] Badalov, S. V.; Yagmurcukardes, M.; Peeters, F. M.; Sahin, H. Enhanced stability of single-layer w-gallenene through hydrogenation. *J. Phys. Chem. C* **2018**, *122*, 28302–28309.

[87] Gao, L. F.; Li, C.; Huang, W. C.; Mei, S.; Lin, H.; Ou, Q.; Zhang, Y.; Guo, J.; Zhang, F.; Xu, S. X. et al. MXene/polymer membranes: Synthesis, properties, and emerging applications. *Chem. Mater.* **2020**, *32*, 1703–1747.

[88] Liu, L. Y.; Orbay, M.; Luo, S.; Duluard, S.; Shao, H.; Harmel, J.; Rozier, P.; Taberna, P. L.; Simon, P. Exfoliation and delamination of $Ti_3C_2T_x$ MXene prepared via molten salt etching route. *ACS Nano* **2022**, *16*, 111–118.

[89] Halim, J.; Lukatskaya, M. R.; Cook, K. M.; Lu, J.; Smith, C. R.; Näslund, L. Å.; May, S. J.; Hultman, L.; Gogotsi, Y.; Eklund, P. et al. Transparent conductive two-dimensional titanium carbide epitaxial thin films. *Chem. Mater.* **2014**, *26*, 2374–2381.

[90] Zhao, X. X.; Sun, W. W.; Geng, D. C.; Fu, W.; Dan, J. D.; Xie, Y.; Kent, P. R. C.; Zhou, W.; Pennycook, S. J.; Loh, K. P. Edge segregated polymorphism in 2D molybdenum carbide. *Adv. Mater.* **2019**, *31*, 1808343.

[91] Wang, B.; Zhong, S. P.; Xu, P.; Zhang, H. Booming development and present advances of two dimensional MXenes for photodetectors. *Chem. Eng. J.* **2021**, *403*, 126336.

[92] Abdolhosseinzadeh, S.; Jiang, X. T.; Zhang, H.; Qiu, J. S.; Zhang, C. F. Perspectives on solution processing of two-dimensional MXenes. *Mater. Today* **2021**, *48*, 214–240.

[93] Zou, J.; Wu, J.; Wang, Y. Z.; Deng, F. X.; Jiang, J. Z.; Zhang, Y. Z.; Liu, S.; Li, N.; Zhang, H.; Yu, J. G. et al. Additive-mediated intercalation and surface modification of MXenes. *Chem. Soc. Rev.* **2022**, *51*, 2972–2990.

[94] Yin, T.; Li, Y.; Wang, R. H.; Al-Hartomy, O. A.; Al-Ghamdi, A.; Wageh, S.; Luo, X. L.; Tang, X.; Zhang, H. Synthesis of $Ti_3C_2F_x$ MXene with controllable fluorination by electrochemical etching for lithium-ion batteries applications. *Ceram. Int.* **2021**, *47*, 28642–28649.

[95] Cao, F. C.; Zhang, Y.; Wang, H. Q.; Khan, K.; Tareen, A. K.; Qian, W. J.; Zhang, H.; Ågren, H. Recent advances in oxidation stable chemistry of 2D MXenes. *Adv. Mater.* **2022**, *34*, 2107554.

[96] Gao, L. F.; Bao, W. L.; Kuklin, A. V.; Mei, S.; Zhang, H.; Ågren, H. Hetero-MXenes: Theory, synthesis, and emerging applications. *Adv. Mater.* **2021**, *33*, 2004129.

[97] Huang, W. C.; Hu, L. P.; Tang, Y. F.; Xie, Z. X.; Zhang, H. Recent advances in functional 2D MXene-based nanostructures for next-generation devices. *Adv. Funct. Mater.* **2020**, *30*, 2005223.

[98] Abbasi, N. M.; Xiao, Y.; Peng, L.; Duo, Y. H.; Wang, L. D.; Zhang, L.; Wang, B.; Zhang, H. Recent advancement for the synthesis of MXene derivatives and their sensing protocol. *Adv. Mater. Technol.* **2021**, *6*, 2001197.

[99] Sundaram, A.; Ponraj, J. S.; Wang, C.; Peng, W. K.; Manavalan, R. K.; Dhanabalan, S. C.; Zhang, H.; Gaspar, J. Engineering of 2D transition metal carbides and nitrides MXenes for cancer therapeutics and diagnostics. *J. Mater. Chem. B* **2020**, *8*, 4990–5013.

[100] Xu, N.; Li, H. B.; Gan, Y. Y.; Chen, H. L.; Li, W. J.; Zhang, F.; Jiang, X. T.; Shi, Y. H.; Liu, J. F.; Wen, Q. et al. Zero-dimensional MXene-based optical devices for ultrafast and ultranarrow photonics applications. *Adv. Sci.* **2020**, *7*, 2002209.

[101] Lin, X. P.; Li, Z. J.; Qiu, J. M.; Wang, Q.; Wang, J. X.; Zhang, H.; Chen, T. K. Fascinating MXene nanomaterials: Emerging opportunities in the biomedical field. *Biomater. Sci.* **2021**, *9*, 5437–5471.

[102] Yue, Y.; Liu, N. S.; Ma, Y. N.; Wang, S. L.; Liu, W. J.; Luo, C.;

Zhang, H.; Cheng, F.; Rao, J. Y.; Hu, X. K. et al. Highly self-healable 3D microsupercapacitor with MXene-graphene composite aerogel. *ACS Nano* **2018**, *12*, 4224–4232.

[103] Yao, Y. H.; Xia, X. F.; Cheng, Z.; Wei, K. K.; Jiang, X. T.; Dong, J. J.; Zhang, H. All-optical modulator using MXene inkjet-printed microring resonator. *IEEE J. Sel. Top. Quantum Electron.* **2020**, *26*, 5900306.

[104] Abbasi, N. M.; Xiao, Y.; Zhang, L.; Peng, L.; Duo, Y. H.; Wang, L. D.; Yin, P.; Ge, Y. Q.; Zhu, H. Y.; Zhang, B. et al. Heterostructures of titanium-based MXenes in energy conversion and storage devices. *J. Mater. Chem. C* **2021**, *9*, 8395–8465.

[105] Li, X. S.; Liu, F.; Huang, D. P.; Xue, N.; Dang, Y. Y.; Zhang, M. Q.; Zhang, L. L.; Li, B.; Liu, D.; Wang, L. et al. Nonoxidized MXene quantum dots prepared by microexplosion method for cancer catalytic therapy. *Adv. Funct. Mater.* **2020**, *30*, 2000308.

[106] Alijani, H.; Rezk, A. R.; Farsani, M. M. K.; Ahmed, H.; Halim, J.; Reineck, P.; Murdoch, B. J.; El-Ghazaly, A.; Rosen, J.; Yeo, L. Y. Acoustomicrofluidic synthesis of pristine ultrathin $Ti_3C_2T_z$ MXene nanosheets and quantum dots. *ACS Nano* **2021**, *15*, 12099–12108.

[107] Feng, Z.; Yiyu, G.; Libin, J.; Qiao, W. MXene quantum dot synthesis, optical properties, and ultra-narrow photonics: A comparison of various sizes and concentrations. *Laser Photonics Rev.* **2021**, *15*, 2100059.

[108] Xue, Q.; Zhang, H. J.; Zhu, M. S.; Pei, Z. X.; Li, H. F.; Wang, Z. F.; Huang, Y.; Huang, Y.; Deng, Q. H.; Zhou, J. et al. Photoluminescent Ti_3C_2 MXene quantum dots for multicolor cellular imaging. *Adv. Mater.* **2017**, *29*, 1604847.

[109] Huang, T.; Ding, J. F.; Liu, Z. R.; Zhang, R.; Zhang, B. L.; Xiong, K.; Zhang, L. Z.; Wang, C.; Shen, S. L.; Li, C. Y. et al. Insight into the underlying competitive mechanism for the shift of the charge neutrality point in a trilayer-graphene field-effect transistor. *eScience* **2022**, *2*, 319–328.

[110] Wang, H.; Wu, Y.; Yuan, X. Z.; Zeng, G. M.; Zhou, J.; Wang, X.; Chew, J. W. Clay-inspired MXene-based electrochemical devices and photo-electrocatalyst: State-of-the-art progresses and challenges. *Adv. Mater.* **2018**, *30*, 1704561.

[111] Ghidiu, M.; Lukatskaya, M. R.; Zhao, M. Q.; Gogotsi, Y.; Barsoum, M. W. Conductive two-dimensional titanium carbide 'clay' with high volumetric capacitance. *Nature* **2014**, *516*, 78–81.

[112] Zheng, W.; Halim, J.; El Ghazaly, A.; Etman, A. S.; Tseng, E. N.; Persson, P. O. Å.; Rosen, J.; Barsoum, M. W. Flexible free-standing $MoO_3/Ti_3C_2T_z$ MXene composite films with high gravimetric and volumetric capacities. *Adv. Sci.* **2021**, *8*, 2003656.

[113] Liu, H.; Chen, X. Y.; Zheng, Y. J.; Zhang, D. B.; Zhao, Y.; Wang, C. F.; Pan, C. F.; Liu, C. T.; Shen, C. Y. Lightweight, superelastic, and hydrophobic polyimide nanofiber /MXene composite aerogel for wearable piezoresistive sensor and oil/water separation applications. *Adv. Funct. Mater.* **2021**, *31*, 2008006.

[114] Geng, D. C.; Zhao, X. X.; Chen, Z. X.; Sun, W. W.; Fu, W.; Chen, J. Y.; Liu, W.; Zhou, W.; Loh, K. P. Direct synthesis of large-area 2D Mo_2C on *in situ* grown graphene. *Adv. Mater.* **2017**, *29*, 1700072.

[115] Sang, X. H.; Xie, Y.; Lin, M. W.; Alhabeb, M.; Van Aken, K. L.; Gogotsi, Y.; Kent, P. R. C.; Xiao, K.; Unocic, R. R. Atomic defects in monolayer titanium carbide ($Ti_3C_2T_x$) MXene. *ACS Nano* **2016**, *10*, 9193–9200.

[116] Zhang, X.; An, D.; Bi, Z. S.; Shan, W.; Zhu, B. B.; Zhou, L.; Yu, L. M.; Zhang, H.; Xia, S. W.; Qiu, M. Ti_3C_2-MXene@N-doped carbon heterostructure-based electrochemical sensor for simultaneous detection of heavy metals. *J. Electroanal. Chem.* **2022**, *911*, 116239.

[117] Li, N.; Jiang, Y.; Xiao, Y.; Meng, B.; Xing, C. Y.; Zhang, H.; Peng, Z. C. A fully inkjet-printed transparent humidity sensor based on a Ti_3C_2/Ag hybrid for touchless sensing of finger motion. *Nanoscale* **2019**, *11*, 21522–21531.

[118] Zhu, B. B.; An, D.; Bi, Z. S.; Liu, W.; Shan, W.; Li, Y. H.; Nie, G. H.; Xie, N.; Al-Hartomy, O. A.; Al-Ghamdi, A. et al. Two-dimensional nitrogen-doped Ti_3C_2 promoted catalysis performance of silver nanozyme for ultrasensitive detection of hydrogen peroxide. *Chem Electro Chem* **2022**, *9*, e202200050.

[119] Zhang, Y.; Jiang, X. T.; Zhang, J. J.; Zhang, H.; Li, Y. C. Simultaneous voltammetric determination of acetaminophen and isoniazid using MXene modified screen-printed electrode. *Biosens. Bioelectron.* **2019**, *130*, 315–321.

[120] Liu, J.; Jiang, X. T.; Zhang, R. Y.; Zhang, Y.; Wu, L. M.; Lu, W.; Li, J. Q.; Li, Y. C.; Zhang, H. MXene-enabled electrochemical microfluidic biosensor: Applications toward multicomponent continuous monitoring in whole blood. *Adv. Funct. Mater.* **2019**, *29*, 1807326.

[121] Chen, Y. Z.; Ge, Y. Q.; Huang, W. C.; Li, Z. J.; Wu, L. M.; Zhang, H.; Li, X. J. Refractive index sensors based on $Ti_3C_2T_x$ MXene fibers. *ACS Appl. Nano Mater.* **2020**, *3*, 303–311.

[122] Ding, H. J.; Zeng, Z. P.; Wang, Z. W.; Li, X. L.; Yildirim, T.; Xie, Q. L.; Zhang, H.; Wageh, S.; Al-Ghamdi, A. A.; Zhang, X. et al. Deep learning-enabled MXene/PEDOT:PSS acoustic sensor for speech recognition and skin-vibration detection. *Adv. Intell. Syst.* **2022**, *4*, 2200140.

[123] Ding, H. J.; Shu, X. L.; Jin, Y. K.; Fan, T. J.; Zhang, H. Recent advances in nanomaterial-enabled acoustic devices for audible sound generation and detection. *Nanoscale* **2019**, *11*, 5839–5860.

[124] Guo, J. H.; Yu, Y. R.; Zhang, H.; Sun, L. Y.; Zhao, Y. J. Elastic MXene hydrogel microfiber-derived electronic skin for joint monitoring. *ACS Appl. Mater. Interfaces* **2021**, *13*, 47800–47806.

[125] Guo, J. H.; Yu, Y. R.; Zhang, D. G.; Zhang, H.; Zhao, Y. J. Morphological hydrogel microfibers with MXene encapsulation for electronic skin. *Research (Wash. D C)* **2021**, *2021*, 7065907.

[126] Fan, Q.; Wang, L. D.; Xu, D.; Duo, Y. H.; Gao, J.; Zhang, L.; Wang, X. B.; Chen, X.; Li, J. H.; Zhang, H. Solution-gated transistors of two-dimensional materials for chemical and biological sensors: Status and challenges. *Nanoscale* **2020**, *12*, 11364–11394.

[127] Dillon, A. D.; Ghidiu, M. J.; Krick, A. L.; Griggs, J.; May, S. J.; Gogotsi, Y.; Barsoum, M. W.; Fafarman, A. T. Highly conductive optical quality solution-processed films of 2D titanium carbide. *Adv. Funct. Mater.* **2016**, *26*, 4162–4168.

[128] Zhou, J.; Yang, T. Q.; Chen, J. J.; Wang, C.; Zhang, H.; Shao, Y. H. Two-dimensional nanomaterial-based plasmonic sensing applications: Advances and challenges. *Coord. Chem. Rev.* **2020**, *410*, 213218.

[129] Xue, T. Y.; Liang, W. Y.; Li, Y. W.; Sun, Y. H.; Xiang, Y. J.; Zhang, Y. P.; Dai, Z. G.; Duo, Y. H.; Wu, L. M.; Qi, K. et al. Ultrasensitive detection of miRNA with an antimonene-based surface plasmon resonance sensor. *Nat. Commun.* **2019**, *10*, 28.

[130] Yang, T. Q.; Gao, L. F.; Wang, W. X.; Kang, J. L.; Zhao, G. H.; Li, D. L.; Chen, W.; Zhang, H. Berlin green framework-based gas sensor for room-temperature and high-selectivity detection of ammonia. *Nano-Micro Lett.* **2021**, *13*, 63.

[131] Bai, S. L.; Sun, C. Z.; Yan, H.; Sun, X. M.; Zhang, H.; Luo, L.; Lei, X. D.; Wan, P. B.; Chen, X. D. Healable, transparent, room-temperature electronic sensors based on carbon nanotube network-coated polyelectrolyte multilayers. *Small* **2015**, *11*, 5807–5813.

[132] Zhang, L.; Khan, K.; Zou, J. F.; Zhang, H.; Li, Y. C. Recent advances in emerging 2D material-based gas sensors: Potential in disease diagnosis. *Adv. Mater. Interfaces* **2019**, *6*, 1901329.

[133] Wang, T.; Yang, H.; Qi, D. P.; Liu, Z. Y.; Cai, P. Q.; Zhang, H.; Chen, X. D. Mechano-based transductive sensing for wearable healthcare. *Small* **2018**, *14*, 1702933.

[134] Wang, T.; Guo, Y. L.; Wan, P. B.; Sun, X. M.; Zhang, H.; Yu, Z. Z.; Chen, X. D. A flexible transparent colorimetric wrist strap sensor. *Nanoscale* **2017**, *9*, 869–874.

[135] Xue, T. Y.; Bongu, S. R.; Huang, H.; Liang, W. Y.; Wang, Y. W.; Zhang, F.; Liu, Z. Y.; Zhang, Y. P.; Zhang, H.; Cui, X. Q. Ultrasensitive detection of microRNA using a bismuthene-enabled fluorescence quenching biosensor. *Chem. Commun.* **2020**, *56*, 7041–7044.

[136] Ren, A. B.; Zou, J. H.; Lai, H. G.; Huang, Y. X.; Yuan, L. M.; Xu, H.; Shen, K.; Wang, H.; Wei, S. Y.; Wang, Y. F. et al. Direct laser-patterned MXene-perovskite image sensor arrays for visible-near infrared photodetection. *Mater. Horiz.* **2020**, *7*, 1901–1911.

[137] Zhang, Y. Z.; Wang, Y.; Jiang, Q.; El-Demellawi, J. K.; Kim, H.;

Alshareef, H. N. MXene printing and patterned coating for device applications. *Adv. Mater.* **2020**, *32*, 1908486.

[138] Kurra, N.; Ahmed, B.; Gogotsi, Y.; Alshareef, H. N. MXene-on-paper coplanar microsupercapacitors. *Adv. Energy Mater.* **2016**, *6*, 1601372.

[139] Hu, H. B.; Bai, Z. M.; Niu, B.; Wu, M. Z.; Hua, T. Binder-free bonding of modularized MXene thin films into thick film electrodes for on-chip micro-supercapacitors with enhanced areal performance metrics. *J. Mater. Chem. A* **2018**, *6*, 14876–14884.

[140] Li, B.; Zhu, Q. B.; Cui, C.; Liu, C.; Wang, Z. H.; Feng, S.; Sun, Y.; Zhu, H. L.; Su, X.; Zhao, Y. M. et al. Patterning of wafer-scale MXene films for high-performance image sensor arrays. *Adv. Mater.* **2022**, *34*, 2201298.

[141] Pang, J. B.; Wang, Y. H.; Yang, X. X.; Zhang, L.; Li, Y. F.; Zhang, Y.; Yang, J. L.; Yang, F.; Wang, X.; Cuniberti, G. et al. A wafer-scale two-dimensional platinum monosulfide ultrathin film via metal sulfurization for high performance photoelectronics. *Mater. Adv.* **2022**, *3*, 1497–1505.

[142] Wang, J.; Liu, S. P.; Pang, J. B.; Song, P.; Tang, W. J.; Ren, Y. H.; Xia, W. Threshold decrease and output-power improvement in dual-loss Q-switched laser based on a few-layer WTe$_2$ saturable absorber. *Appl. Phys. Express* **2020**, *13*, 052004.

[143] Wang, Y. H.; Zhang, Y. H.; Cheng, Q. L.; Pang, J. B.; Chu, Y. J.; Ji, H.; Gao, J. W.; Han, Y. K.; Han, L.; Liu, H. et al. Large area uniform PtS$_x$ synthesis on sapphire substrate for performance improved photodetectors. *Appl. Mater. Today* **2021**, *25*, 101176.

[144] Cao, Y.; Qu, P.; Wang, C. G.; Zhou, J.; Li, M. H.; Yu, X. M.; Yu, X.; Pang, J. B.; Zhou, W. J.; Liu, H. et al. Epitaxial growth of vertically aligned antimony selenide nanorod arrays for heterostructure based self-powered photodetector. *Adv. Opt. Mater.* **2022**, *10*, 2200816.

[145] Cheng, Q. L.; Pang, J. B.; Sun, D. H.; Wang, J. G.; Zhang, S.; Liu, F.; Chen, Y. K.; Yang, R. Q.; Liang, N.; Lu, X. H. et al. WSe$_2$ 2D p-type semiconductor-based electronic devices for information technology: Design, preparation, and applications. *InfoMat* **2020**, *2*, 656–697.

[146] Zhang, S.; Pang, J. B.; Cheng, Q. L.; Yang, F.; Chen, Y.; Liu, Y.; Li, Y. F.; Gemming, T.; Liu, X. Y.; Ibarlucea, B. et al. High-performance electronics and optoelectronics of monolayer tungsten diselenide full film from pre-seeding strategy. *InfoMat* **2021**, *3*, 1455–1469.

[147] Wang, Y. H.; Pang, J. B.; Cheng, Q. L.; Han, L.; Li, Y. F.; Meng, X.; Ibarlucea, B.; Zhao, H. B.; Yang, F.; Liu, H. Y. et al. Applications of 2D-layered palladium diselenide and its van der Waals heterostructures in electronics and optoelectronics. *Nano-Micro Lett.* **2021**, *13*, 143.

[148] Hu, C. Q.; Chen, H.; Li, L.; Huang, H.; Shen, G. Z. Ti$_3$C$_2$T$_x$ MXene-RAN van der Waals heterostructure-based flexible transparent NIR photodetector array for 1,024 pixel image sensing application. *Adv. Mater. Technol.* **2022**, *7*, 2101639.

[149] Li, L. D.; Ye, S.; Qu, J. L.; Zhou, F. F.; Song, J.; Shen, G. Z. Recent advances in perovskite photodetectors for image sensing. *Small* **2021**, *17*, 2005606.

[150] Lou, Z.; Shen, G. Z. Flexible image sensors with semiconducting nanowires for biomimic visual applications. *Small Struct.* **2021**, *2*, 2000152.

[151] Cao, Y.; Liu, C. Y.; Yang, T. H.; Zhao, Y.; Na, Y. L.; Jiang, C. X.; Zhou, J.; Pang, J. B.; Liu, H.; Rummeli, M. H. et al. Gradient bandgap modification for highly efficient carrier transport in antimony sulfide-selenide tandem solar cells. *Sol. Energy Mater. Sol. Cells* **2022**, *246*, 111926.

[152] Cao, Y.; Liu, C. Y.; Jiang, J. H.; Zhu, X. Y.; Zhou, J.; Ni, J.; Zhang, J. J.; Pang, J. B.; Rummeli, M. H.; Zhou, W. J. et al. Theoretical insight into high-efficiency triple-junction tandem solar cells via the band engineering of antimony chalcogenides. *Solar RRL* **2021**, *5*, 2000800.

[153] Li, L.; Chen, H. Y.; Fang, Z. M.; Meng, X. Y.; Zuo, C. T.; Lv, M. L.; Tian, Y. Z.; Fang, Y.; Xiao, Z.; Shan, C. X. et al. An electrically modulated single-color/dual-color imaging photodetector. *Adv. Mater.* **2020**, *32*, 1907257.

[154] Cao, Y.; Zhu, X. Y.; Chen, H. B.; Zhang, X. T.; Zhou, J.; Hu, Z. Y.; Pang, J. B. Towards high efficiency inverted Sb$_2$Se$_3$ thin film solar cells. *Sol. Energy Mater. Sol. Cells* **2019**, *200*, 109945.

[155] Zhou, J.; Meng, D.; Yang, T. H.; Zhang, X. T.; Tang, Z. Q.; Cao, Y.; Ni, J.; Zhang, J. J.; Hu, Z. Y.; Pang, J. B. Enhanced charge carrier transport via efficient grain conduction mode for Sb$_2$Se$_3$ solar cell applications. *Appl. Surf. Sci.* **2022**, *591*, 153169.

[156] Cao, Y.; Zhu, X. Y.; Jiang, J. H.; Liu, C. Y.; Zhou, J.; Ni, J.; Zhang, J. J.; Pang, J. B. Rotational design of charge carrier transport layers for optimal antimony trisulfide solar cells and its integration in tandem devices. *Sol. Energy Mater. Sol. Cells* **2020**, *206*, 110279.

[157] Zhou, J.; Chen, H. B.; Zhang, X. T.; Chi, K. L.; Cai, Y. M.; Cao, Y.; Pang, J. B. Substrate dependence on (Sb$_4$Se$_6$)$_n$ ribbon orientations of antimony selenide thin films: Morphology, carrier transport and photovoltaic performance. *J. Alloys Compd.* **2021**, *862*, 158703.

[158] Cao, Y.; Zhu, X. Y.; Tong, X. Y.; Zhou, J.; Ni, J.; Zhang, J. J.; Pang, J. B. Ultrathin microcrystalline hydrogenated Si/Ge alloyed tandem solar cells towards full solar spectrum conversion. *Front. Chem. Sci. Eng.* **2020**, *14*, 997–1005.

[159] He, Z. C.; Liu, Y.; Lin, S. P.; Shi, S. H.; Sun, S. L.; Pang, J. B.; Zhou, Z. Q.; Sun, Y.; Liu, W. Energy band alignment in molybdenum oxide/Cu(In, Ga)Se$_2$ interface for high-efficiency ultrathin Cu(In, Ga)Se$_2$ solar cells from low-temperature growth. *ACS Appl. Energy Mater.* **2020**, *3*, 3408–3414.

[160] Pang, J. B.; Cai, Y. A.; He, Q.; Wang, H.; Jiang, W. L.; He, J. J.; Yu, T.; Liu, W.; Zhang, Y.; Sun, Y. Preparation and characteristics of MoSe$_2$ interlayer in bifacial Cu(In, Ga)Se$_2$ solar cells. *Phys. Procedia* **2012**, *32*, 372–378.

[161] Liu, W.; He, J. J.; Li, Z. G.; Jiang, W. L.; Pang, J. B.; Zhang, Y.; Sun, Y. Effect of Na on lower open circuit voltage of flexible CIGS thin-film solar cells prepared by the low-temperature process. *Phys. Scr.* **2012**, *85*, 055806.

[162] Zhang, S. C.; Li, S. Y.; Lu, Y. Y. Designing safer lithium-based batteries with nonflammable electrolytes: A review. *eScience* **2021**, *1*, 163–177.

[163] Guo, Y.; Wu, S. C.; He, Y. B.; Kang, F. Y.; Chen, L. Q.; Li, H.; Yang, Q. H. Solid-state lithium batteries: Safety and prospects. *eScience* **2022**, *2*, 138–163.

[164] Le, T. S. D.; An, J. N.; Huang, Y.; Vo, Q.; Boonruangkan, J.; Tran, T.; Kim, S. W.; Sun, G. Z.; Kim, Y. J. Ultrasensitive anti-interference voice recognition by bio-inspired skin-attachable self-cleaning acoustic sensors. *ACS Nano* **2019**, *13*, 13293–13303.

[165] Gu, Y.; Wang, X. W.; Gu, W.; Wu, Y. J.; Li, T.; Zhang, T. Flexible electronic eardrum. *Nano Res.* **2017**, *10*, 2683–2691.

[166] Gou, G. Y.; Li, X. S.; Jian, J. M.; Tian, H.; Wu, F.; Ren, J.; Geng, X. S.; Xu, J. D.; Qiao, Y. C.; Yan, Z. Y. et al. Two-stage amplification of an ultrasensitive MXene-based intelligent artificial eardrum. *Sci. Adv.* **2022**, *8*, eabn2156.

[167] Cai, Y. C.; Shen, J.; Ge, G.; Zhang, Y. Z.; Jin, W. Q.; Huang, W.; Shao, J. J.; Yang, J.; Dong, X. C. Stretchable Ti$_3$C$_2$T$_x$ MXene/carbon nanotube composite based strain sensor with ultrahigh sensitivity and tunable sensing range. *ACS Nano* **2018**, *12*, 56–62.

[168] Wang, K.; Lou, Z.; Wang, L. L.; Zhao, L. J.; Zhao, S. F.; Wang, D. Y.; Han, W.; Jiang, K.; Shen, G. Z. Bioinspired interlocked structure-induced high deformability for two-dimensional titanium carbide (MXene)/natural microcapsule-based flexible pressure sensors. *ACS Nano* **2019**, *13*, 9139–9147.

[169] Jin, Y. K.; Wen, B.; Gu, Z. X.; Jiang, X. T.; Shu, X. L.; Zeng, Z. P.; Zhang, Y. P.; Guo, Z. N.; Chen, Y.; Zheng, T. T. et al. Deep-learning-enabled MXene-based artificial throat: Toward sound detection and speech recognition. *Adv. Mater. Technol.* **2020**, *5*, 2000262.

[170] Li, G. J.; Cheng, Z. X.; Xiang, Q.; Yan, L. M.; Wang, X. H.; Xu, J. Q. Bimetal PdAu decorated SnO$_2$ nanosheets based gas sensor with temperature-dependent dual selectivity for detecting formaldehyde and acetone. *Sens. Actuators B:Chem.* **2019**, *283*, 590–601.

[171] Drmosh, Q. A.; Alade, I. O.; Qamar, M.; Akbar, S. Zinc oxide-

based acetone gas sensors for breath analysis: A review. *Chem. Asian J.* **2021**, *16*, 1519–1538.

[172] Xing, X. X.; Du, L. L.; Feng, D. L.; Wang, C.; Yao, M. S.; Huang, X. H.; Zhang, S. X.; Yang, D. C. Individual gas sensor detecting dual exhaled biomarkers via a temperature modulated n/p semiconducting transition. *J. Mater. Chem. A* **2020**, *8*, 26004–26012.

[173] Wang, Z. N.; Wang, C. J. Is breath acetone a biomarker of diabetes? A historical review on breath acetone measurements. *J. Breath Res.* **2013**, *7*, 037109.

[174] Sharma, B.; Sharma, A.; Myung, J. H. Highly selective detection of acetone by TiO_2–SnO_2 heterostructures for environmental biomarkers of diabetes. *Sens. Actuators B:Chem.* **2021**, *349*, 130733.

[175] Yuan, K. P.; Wang, C. Y.; Zhu, L. Y.; Cao, Q.; Yang, J. H.; Li, X. X.; Huang, W.; Wang, Y. Y.; Lu, H. L.; Zhang, D. W. Fabrication of a micro-electromechanical system-based acetone gas sensor using CeO_2 nanodot-decorated WO_3 nanowires. *ACS Appl. Mater. Interfaces* **2020**, *12*, 14095–14104.

[176] Liu, M.; Ji, J.; Song, P.; Liu, M.; Wang, Q. α-Fe_2O_3 nanocubes/$Ti_3C_2T_x$ MXene composites for improvement of acetone sensing performance at room temperature. *Sens. Actuators B: Chem.* **2021**, *349*, 130782.

[177] Kumar, A.; Daw, P.; Milstein, D. Homogeneous catalysis for sustainable energy: Hydrogen and methanol economies, fuels from biomass, and related topics. *Chem. Rev.* **2022**, *122*, 385–441.

[178] Gautam, P.; Neha; Upadhyay, S. N.; Dubey, S. K. Bio-methanol as a renewable fuel from waste biomass: Current trends and future perspective. *Fuel* **2020**, *273*, 117783.

[179] Feng, C. H.; Jiang, Z. W.; Chen, B.; Cheng, P. F.; Wang, Y. L.; Huang, C. Z. Aluminum-doped NiO nanofibers as chemical sensors for selective and sensitive methanol detection. *Anal. Methods* **2019**, *11*, 575–581.

[180] Zhang, Y.; Pan, W. J.; Dong, G. K.; Zhang, D. Z. A high-performance room temperature methanol gas sensor based on alpha-iron oxide/polyaniline/PbS quantum dots nanofilm. *J. Mater. Sci.: Mater. Electron.* **2019**, *30*, 17907–17915.

[181] Van Den Broek, J.; Abegg, S.; Pratsinis, S. E.; Güntner, A. T. Highly selective detection of methanol over ethanol by a handheld gas sensor. *Nat. Commun.* **2019**, *10*, 4220.

[182] Young, S. J.; Chu, Y. L. Platinum nanoparticle-decorated ZnO nanorods improved the performance of methanol gas sensor. *J. Electrochem. Soc.* **2020**, *167*, 147508.

[183] Sinha, M.; Neogi, S.; Mahapatra, R.; Krishnamurthy, S.; Ghosh, R. Material dependent and temperature driven adsorption switching (p- to n-type) using CNT/ZnO composite-based chemiresistive methanol gas sensor. *Sens. Actuators B:Chem.* **2021**, *336*, 129729.

[184] Liu, M.; Wang, Z. Y.; Song, P.; Yang, Z. X.; Wang, Q. In_2O_3 nanocubes/$Ti_3C_2T_x$ MXene composites for enhanced methanol gas sensing properties at room temperature. *Ceram. Int.* **2021**, *47*, 23028–23037.

[185] Li, H. J.; Zhang, N.; Zhao, X. L.; Xu, Z. Q.; Zhang, Z. Y.; Wang, Y. Modulation of TEA and methanol gas sensing by ion-exchange based on a sacrificial template 3D diamond-shaped MOF. *Sens. Actuators B:Chem.* **2020**, *315*, 128136.

[186] Dasari, S. G.; Nagaraju, P.; Yelsani, V.; Tirumala, S.; Reddy, M. V. R. Nanostructured indium oxide thin films as a room temperature toluene sensor. *ACS Omega* **2021**, *6*, 17442–17454.

[187] Ahmed, A. M.; Mehaney, A.; Elsayed, H. A. Detection of toluene traces in exhaled breath by using a 1D PC as a biomarker for lung cancer diagnosis. *Eur. Phys. J. Plus* **2021**, *136*, 626.

[188] Gregis, G.; Sanchez, J. B.; Bezverkhyy, I.; Weber, G.; Berger, F.; Fierro, V.; Bellat, J. P.; Celzard, A. Detection and quantification of lung cancer biomarkers by a micro-analytical device using a single metal oxide-based gas sensor. *Sens. Actuators B:Chem.* **2018**, *255*, 391–400.

[189] Guo, W. Z.; Surya, S. G.; Babar, V.; Ming, F. W.; Sharma, S.; Alshareef, H. N.; Schwingenschlögl, U.; Salama, K. N. Selective toluene detection with Mo_2CT_x MXene at room temperature. *ACS Appl. Mater. Interfaces* **2020**, *12*, 57218–57227.

[190] Iqbal, A.; Sambyal, P.; Kwon, J.; Han, M. K.; Hong, J.; Kim, S. J.; Kim, M. K.; Gogotsi, Y.; Koo, C. M. Enhanced absorption of electromagnetic waves in $Ti_3C_2T_x$ MXene films with segregated polymer inclusions. *Compos. Sci. Technol.* **2021**, *213*, 108878.

[191] Ma, H.; Xu, Y. M.; Rong, Z. M.; Cheng, X. L.; Gao, S.; Zhang, X. F.; Zhao, H.; Huo, L. H. Highly toluene sensing performance based on monodispersed Cr_2O_3 porous microspheres. *Sens. Actuators B:Chem.* **2012**, *174*, 325–331.

[192] Lee, E.; VahidMohammadi, A.; Prorok, B. C.; Yoon, Y. S.; Beidaghi, M.; Kim, D. J. Room temperature gas sensing of two-dimensional titanium carbide (MXene). *ACS Appl. Mater. Interfaces* **2017**, *9*, 37184–37190.

[193] Kim, S. J.; Koh, H. J.; Ren, C. E.; Kwon, O.; Maleski, K.; Cho, S. Y.; Anasori, B.; Kim, C. K.; Choi, Y. K.; Kim, J. et al. Metallic $Ti_3C_2T_x$ MXene gas sensors with ultrahigh signal-to-noise ratio. *ACS Nano* **2018**, *12*, 986–993.

[194] Wu, M.; He, M.; Hu, Q. K.; Wu, Q. H.; Sun, G.; Xie, L. L.; Zhang, Z. Y.; Zhu, Z. G.; Zhou, A. G. Ti_3C_2 MXene-based sensors with high selectivity for NH_3 detection at room temperature. *ACS Sens.* **2019**, *4*, 2763–2770.

[195] Yuan, W. J.; Yang, K.; Peng, H. F.; Li, F.; Yin, F. X. A flexible VOCs sensor based on a 3D Mxene framework with a high sensing performance. *J. Mater. Chem. A* **2018**, *6*, 18116–18124.

[196] Zhao, Q. N.; Zhang, Y. J.; Duan, Z. H.; Wang, S.; Liu, C.; Jiang, Y. D.; Tai, H. L. A review on $Ti_3C_2T_x$-based nanomaterials: Synthesis and applications in gas and humidity sensors. *Rare Met.* **2020**, *40*, 1459–1476.

[197] Pazniak, H.; Varezhnikov, A. S.; Kolosov, D. A.; Plugin, I. A.; Vito, A. D.; Glukhova, O. E.; Sheverdyaeva, P. M.; Spasova, M.; Kaikov, I.; Kolesnikov, E. A. et al. 2D molybdenum carbide MXenes for enhanced selective detection of humidity in air. *Adv. Mater.* **2021**, *33*, 2104878.

[198] Bajaj, K. L.; Kaur, G. Colorimetric determination of capsaicin in capsicum fruits with the Folin−Ciocalteu reagent. *Microchim. Acta* **1979**, *71*, 81–86.

[199] Perucka, I.; Oleszek, W. Extraction and determination of capsaicinoids in fruit of hot pepper *Capsicum annuum* L. by spectrophotometry and high-performance liquid chromatography. *Food Chem.* **2000**, *71*, 287–291.

[200] Hamada, N.; Hashi, Y.; Yamaki, S.; Guo, Y. L.; Zhang, L.; Li, H. F.; Lin, J. M. Construction of on-line supercritical fluid extraction with reverse phase liquid chromatography-tandem mass spectrometry for the determination of capsaicin. *Chin. Chem. Lett.* **2019**, *30*, 99–102.

[201] Gu, Q. H.; Chen, X. G.; Lu, C. Q.; Ye, C. Z.; Li, W. Z.; Chu, J. Y.; Zhang, W. G.; Wang, Z. P.; Xu, B. C. Electrochemical determination of capsaicinoids content in soy sauce and pot-roast meat products by glassy carbon electrode modified with MXene/PDDA-carbon nanotubes/β-cyclodextrin. *Food Control* **2022**, *138*, 109022.

[202] Wang, G. X.; Sun, J. F.; Yao, Y.; An, X. S.; Zhang, H.; Chu, G. L.; Jiang, S.; Guo, Y. M.; Sun, X.; Liu, Y. Detection of inosine monophosphate (IMP) in meat using double-enzyme sensor. *Food Anal. Methods* **2020**, *13*, 420–432.

[203] Liu, J. S.; Fan, Y. X.; Chen, G. L.; Liu, Y. Highly sensitive glutamate biosensor based on platinum nanoparticles decorated MXene-$Ti_3C_2T_x$ for l-glutamate determination in foodstuffs. *LWT* **2021**, *148*, 111748.

[204] Gao, J. W.; Gao, Y. K.; Han, Y. K.; Pang, J. B.; Wang, C.; Wang, Y. H.; Liu, H.; Zhang, Y.; Han, L. Ultrasensitive label-free MiRNA sensing based on a flexible graphene field-effect transistor without functionalization. *ACS Appl. Electron. Mater.* **2020**, *2*, 1090–1098.

[205] Yin, Y.; Pang, J. B.; Wang, J. W.; Lu, X. Y.; Hao, Q.; Naz, E. S. G.; Zhou, X. X.; Ma, L. B.; Schmidt, O. G. Graphene-activated optoplasmonic nanomembrane cavities for photodegradation detection. *ACS Appl. Mater. Interfaces* **2019**, *11*, 15891–15897.

[206] Jiang, J. F.; Zhang, Y.; Wang, A. Z.; Duan, J. Z.; Ji, H.; Pang, J. B.; Sang, Y. H.; Feng, X. J.; Liu, H.; Han, L. Construction of high field-effect mobility multilayer MoS_2 field-effect transistors with excellent stability through interface engineering. *ACS Appl. Electron. Mater.* **2020**, *2*, 2132–2140.

[207] Jiang, J. F.; Meng, F. Q.; Cheng, Q. L.; Wang, A. Z.; Chen, Y. K.;

Qiao, J.; Pang, J. B.; Xu, W. D.; Ji, H.; Zhang, Y. et al. Low lattice mismatch inse-se vertical van der Waals heterostructure for high-performance transistors via strong fermi-level depinning. *Small Methods* **2020**, *4*, 2000238.

[208] Sun, B. J.; Pang, J. B.; Cheng, Q. L.; Zhang, S.; Li, Y. F.; Zhang, C. C.; Sun, D. H.; Ibarlucea, B.; Li, Y.; Chen, D. et al. Synthesis of wafer-scale graphene with chemical vapor deposition for electronic device applications. *Adv. Mater. Technol.* **2021**, *6*, 2000744.

[209] Lei, D. D.; Liu, N. S.; Su, T. Y.; Zhang, Q. X.; Wang, L. X.; Ren, Z. Q.; Gao, Y. H. Roles of MXene in pressure sensing: Preparation, composite structure design, and mechanism. *Adv. Mater.*, in press, https://doi.org/10.1002/adma.202110608.

[210] Fu, X. Y.; Wang, L. L.; Zhao, L. J.; Yuan, Z. Y.; Zhang, Y. P.; Wang, D. Y.; Wang, D. P.; Li, J. Z.; Li, D. D.; Shulga, V. et al. Controlled assembly of MXene nanosheets as an electrode and active layer for high-performance electronic skin. *Adv. Funct. Mater.* **2021**, *31*, 2010533.

[211] Zhao, L. J.; Wang, L. L.; Zheng, Y. Q.; Zhao, S. F.; Wei, W.; Zhang, D. W.; Fu, X. Y.; Jiang, K.; Shen, G. Z.; Han, W. Highly-stable polymer-crosslinked 2D MXene-based flexible biocompatible electronic skins for *in vivo* biomonitoring. *Nano Energy* **2021**, *84*, 105921.

[212] Wang, D. Y.; Wang, L. L.; Lou, Z.; Zheng, Y. Q.; Wang, K.; Zhao, L. J.; Han, W.; Jiang, K.; Shen, G. Z. Biomimetic, biocompatible and robust silk Fibroin-MXene film with stable 3D cross-link structure for flexible pressure sensors. *Nano Energy* **2020**, *78*, 105252.

[213] Wang, L. L.; Wang, D. P.; Wang, K.; Jiang, K.; Shen, G. Z. Biocompatible MXene/chitosan-based flexible bimodal devices for real-time pulse and respiratory rate monitoring. *ACS Materials Lett.* **2021**, *3*, 921–929.

[214] Ryan, K. R.; Down, M. P.; Hurst, N. J.; Keefe, E. M.; Banks, C. E. Additive manufacturing (3D printing) of electrically conductive polymers and polymer nanocomposites and their applications. *eScience* **2022**, *2*, 365–381.

[215] Liu, Q. Q.; Liu, R. T.; He, C. H.; Xia, C. F.; Guo, W.; Xu, Z. L.; Xia, B. Y. Advanced polymer-based electrolytes in zinc-air batteries. *eScience* **2022**, *2*, 453–466.

[216] Zhao, S. F.; Ran, W. H.; Wang, L. L.; Shen, G. Z. Interlocked MXene/rGO aerogel with excellent mechanical stability for a health-monitoring device. *J. Semicond.* **2022**, *43*, 082601.

[217] Yang, Z. J.; Lv, S. Y.; Zhang, Y. Y.; Wang, J.; Jiang, L.; Jia, X. T.; Wang, C. G.; Yan, X.; Sun, P.; Duan, Y. et al. Self-assembly 3D porous crumpled MXene spheres as efficient gas and pressure sensing material for transient all-MXene sensors. *Nano-Micro Lett.* **2022**, *14*, 56.

[218] Guo, Y.; Zhong, M. J.; Fang, Z. W.; Wan, P. B.; Yu, G. H. A wearable transient pressure sensor made with MXene nanosheets for sensitive broad-range human-machine interfacing. *Nano Lett.* **2019**, *19*, 1143–1150.

[219] Lee, S.; Kim, E. H.; Yu, S.; Kim, H.; Park, C.; Lee, S. W.; Han, H.; Jin, W.; Lee, K.; Lee, C. E. et al. Polymer-laminated $Ti_3C_2T_X$ MXene electrodes for transparent and flexible field-driven electronics. *ACS Nano* **2021**, *15*, 8940–8952.

[220] Cai, Y. C.; Shen, J.; Yang, C. W.; Wan, Y.; Tang, H. L.; Aljarb, A. A.; Chen, C. L.; Fu, J. H.; Wei, X.; Huang, K. W. et al. Mixed-dimensional MXene-hydrogel heterostructures for electronic skin sensors with ultrabroad working range. *Sci. Adv.* **2020**, *6*, eabb5367.

[221] Leung, S. F.; Ho, K. T.; Kung, P. K.; Hsiao, V. K. S.; Alshareef, H. N.; Wang, Z. L.; He, J. H. A self-powered and flexible organometallic halide perovskite photodetector with very high detectivity. *Adv. Mater.* **2018**, *30*, 1704611.

[222] Liana, D. D.; Raguse, B.; Gooding, J. J.; Chow, E. An integrated paper-based readout system and piezoresistive pressure sensor for measuring bandage compression. *Adv. Mater. Technol.* **2016**, *1*, 1600143.

[223] Zhou, Z. Q.; Li, Y.; Cheng, J.; Chen, S. Y.; Hu, R.; Yan, X. W.; Liao, X. Q.; Xu, C. M.; Yu, J. S.; Li, L. Supersensitive all-fabric pressure sensors using printed textile electrode arrays for human

motion monitoring and human-machine interaction. *J. Mater. Chem. C* **2018**, *6*, 13120–13127.

[224] Zhu, Y. Z.; Hartel, M. C.; Yu, N.; Garrido, P. R.; Kim, S.; Lee, J.; Bandaru, P.; Guan, S. H.; Lin, H. S.; Emaminejad, S. et al. Epidermis-inspired wearable piezoresistive pressure sensors using reduced graphene oxide self-wrapped copper nanowire networks. *Small Methods* **2022**, *6*, 2100900.

[225] Pu, L.; Ma, H. J.; Dong, J. C.; Zhang, C.; Lai, F. L.; He, G. J.; Ma, P. M.; Dong, W. F.; Huang, Y. P.; Liu, T. X. Xylem-inspired polyimide/MXene aerogels with radial lamellar architectures for highly sensitive strain detection and efficient solar steam generation. *Nano Lett.* **2022**, *22*, 4560–4568.

[226] Kim, J.; Jang, M.; Jeong, G.; Yu, S.; Park, J.; Lee, Y.; Cho, S.; Yeom, J.; Lee, Y.; Choe, A. et al. MXene-enhanced β-phase crystallization in ferroelectric porous composites for highly-sensitive dynamic force sensors. *Nano Energy* **2021**, *89*, 106409.

[227] Zhang, Z. C.; Yan, Q. Y.; Liu, Z. R.; Zhao, X. Y.; Wang, Z.; Sun, J.; Wang, Z. L.; Wang, R. R.; Li, L. L. Flexible MXene composed triboelectric nanogenerator via facile vacuum-assistant filtration method for self-powered biomechanical sensing. *Nano Energy* **2021**, *88*, 106257.

[228] Feig, V. R.; Tran, H.; Bao, Z. N. Biodegradable polymeric materials in degradable electronic devices. *ACS Cent. Sci.* **2018**, *4*, 337–348.

[229] Chang, J. K.; Chang, H. P.; Guo, Q. L.; Koo, J.; Wu, C. I.; Rogers, J. A. Biodegradable electronic systems in 3D, heterogeneously integrated formats. *Adv. Mater.* **2018**, *30*, 1704955.

[230] Li, W. H.; Liu, Q.; Zhang, Y.; Li, C. A.; He, Z. F.; Choy, W. C. H.; Low, P. J.; Sonar, P.; Kyaw, A. K. K. Biodegradable materials and green processing for green electronics. *Adv. Mater.* **2020**, *32*, 2001591.

[231] Shin, J.; Yan, Y.; Bai, W. B.; Xue, Y. G.; Gamble, P.; Tian, L. M.; Kandela, I.; Haney, C. R.; Spees, W.; Lee, Y. et al. Bioresorbable pressure sensors protected with thermally grown silicon dioxide for the monitoring of chronic diseases and healing processes. *Nat. Biomed. Eng.* **2019**, *3*, 37–46.

[232] Choi, Y. S.; Hsueh, Y. Y.; Koo, J.; Yang, Q. S.; Avila, R.; Hu, B. W.; Xie, Z. Q.; Lee, G.; Ning, Z.; Liu, C. et al. Stretchable, dynamic covalent polymers for soft, long-lived bioresorbable electronic stimulators designed to facilitate neuromuscular regeneration. *Nat. Commun.* **2020**, *11*, 5990.

[233] Shin, J.; Liu, Z. H.; Bai, W. B.; Liu, Y. H.; Yan, Y.; Xue, Y. G.; Kandela, I.; Pezhouh, M.; MacEwan, M. R.; Huang, Y. G. et al. Bioresorbable optical sensor systems for monitoring of intracranial pressure and temperature. *Sci. Adv.* **2019**, *5*, eaaw1899.

[234] Yang, Q. S.; Liu, T. L.; Xue, Y. G.; Wang, H. L.; Xu, Y. M.; Emon, B.; Wu, M. Z.; Rountree, C.; Wei, T.; Kandela, I. et al. Ecoresorbable and bioresorbable microelectromechanical systems. *Nat. Electron.* **2022**, *5*, 526–538.

[235] Chen, X.; Park, Y. J.; Kang, M.; Kang, S. K.; Koo, J.; Shinde, S. M.; Shin, J.; Jeon, S.; Park, G.; Yan, Y. et al. CVD-grown monolayer MoS_2 in bioabsorbable electronics and biosensors. *Nat. Commun.* **2018**, *9*, 1690.

[236] Han, W. B.; Lee, J. H.; Shin, J. W.; Hwang, S. W. Advanced materials and systems for biodegradable, transient electronics. *Adv. Mater.* **2020**, *32*, 2002211.

[237] Li, C. M.; Guo, C. C.; Fitzpatrick, V.; Ibrahim, A.; Zwierstra, M. J.; Hanna, P.; Lechtig, A.; Nazarian, A.; Lin, S. J.; Kaplan, D. L. Design of biodegradable, implantable devices towards clinical translation. *Nat. Rev. Mater.* **2020**, *5*, 61–81.

[238] Wang, D. P.; Zhao, S. F.; Yin, R. Y.; Li, L. L.; Lou, Z.; Shen, G. Z. Recent advanced applications of ion-gel in ionic-gated transistor. *npj Flexible Electron.* **2021**, *5*, 13.

[239] Wang, L. L.; Wang, K.; Lou, Z.; Jiang, K.; Shen, G. Z. Plant-based modular building blocks for "green" electronic skins. *Adv. Funct. Mater.* **2018**, *28*, 1804510.

[240] Won, S. M.; Koo, J.; Crawford, K. E.; Mickle, A. D.; Xue, Y. G.; Min, S.; McIlvried, L. A.; Yan, Y.; Kim, S. B.; Lee, S. M. et al. Natural wax for transient electronics. *Adv. Funct. Mater.* **2018**, *28*, 1801819.

[241] Cui, Y. J.; Zhang, F.; Chen, G.; Yao, L.; Zhang, N.; Liu, Z. Y.; Li, Q. S.; Zhang, F. L.; Cui, Z. Q.; Zhang, K. Q. et al. A stretchable and transparent electrode based on PEGylated silk fibroin for *in vivo* dual-modal neural-vascular activity probing. *Adv. Mater.* **2021**, *33*, 2100221.

[242] Chen, G.; Matsuhisa, N.; Liu, Z. Y.; Qi, D. P.; Cai, P. Q.; Jiang, Y.; Wan, C. J.; Cui, Y. J.; Leow, W. R.; Liu, Z. J. et al. Plasticizing silk protein for on-skin stretchable electrodes. *Adv. Mater.* **2018**, *30*, 1800129.

[243] Zarei, M.; Lee, G.; Lee, S. G.; Cho, K. Advances in biodegradable electronic skin: Material progress and recent applications in sensing, robotics, and human-machine interfaces. *Adv. Mater.*, in press, https://doi.org/10.1002/adma.202203193.

[244] Matsuhisa, N.; Chen, X. D.; Bao, Z. N.; Someya, T. Materials and structural designs of stretchable conductors. *Chem. Soc. Rev.* **2019**, *48*, 2946–2966.

[245] Wang, H. L.; Wang, Y.; Ni, Z. J.; Turetta, N.; Gali, S. M.; Peng, H. J.; Yao, Y. F.; Chen, Y. S.; Janica, I.; Beljonne, D. et al. 2D MXene-molecular hybrid additive for high-performance ambipolar polymer field-effect transistors and logic gates. *Adv. Mater.* **2021**, *33*, 2008215.

[246] Liu, J.; McKeon, L.; Garcia, J.; Pinilla, S.; Barwich, S.; Möbius, M.; Stamenov, P.; Coleman, J. N.; Nicolosi, V. Additive manufacturing of Ti_3C_2-MXene-functionalized conductive polymer hydrogels for electromagnetic-interference shielding. *Adv. Mater.* **2022**, *34*, 2106253.

[247] Han, Q. F.; Pang, J. B.; Li, Y. F.; Sun, B. J.; Ibarlucea, B.; Liu, X. Y.; Gemming, T.; Cheng, Q. L.; Zhang, S.; Liu, H. et al. Graphene biodevices for early disease diagnosis based on biomarker detection. *ACS Sens.* **2021**, *6*, 3841–3881.

[248] Zhang, S.; Pang, J. B.; Li, Y. F.; Ibarlucea, B.; Liu, Y.; Wang, T.; Liu, X. Y.; Peng, S. A.; Gemming, T.; Cheng, Q. L. et al. An effective formaldehyde gas sensor based on oxygen-rich three-dimensional graphene. *Nanotechnology* **2022**, *33*, 185702.

[249] Ibrahim, I.; Kalbacova, J.; Engemaier, V.; Pang, J. B.; Rodriguez, R. D.; Grimm, D.; Gemming, T.; Zahn, D. R. T.; Schmidt, O. G.; Eckert, J. et al. Confirming the dual role of etchants during the enrichment of semiconducting single wall carbon nanotubes by chemical vapor deposition. *Chem. Mater.* **2015**, *27*, 5964–5973.

[250] Pang, J. B.; Bachmatiuk, A.; Fu, L.; Mendes, R. G.; Libera, M.; Placha, D.; Martynková, G. S.; Trzebicka, B.; Gemming, T.; Eckert, J. et al. Direct synthesis of graphene from adsorbed organic solvent molecules over copper. *RSC Adv.* **2015**, *5*, 60884–60891.

[251] Pang, J. B.; Bachmatiuk, A.; Ibrahim, I.; Fu, L.; Placha, D.; Martynkova, G. S.; Trzebicka, B.; Gemming, T.; Eckert, J.; Rümmeli, M. H. CVD growth of 1D and 2D sp² carbon nanomaterials. *J. Mater. Sci.* **2016**, *51*, 640–667.

[252] Martynková, G. S.; Becerik, F.; Plachá, D.; Pang, J. B.; Akbulut, H.; Bachmatiuk, A.; Rummeli, M. H. Effect of milling and annealing on carbon-silver system. *J. Nanosci. Nanotechnol.* **2019**, *19*, 2770–2774.

[253] Guo, Z. J.; Sun, C. H.; Yang, H. R.; Gao, H. Y.; Liang, N.; Wang, J.; Hu, S.; Ren, N.; Pang, J. B.; Wang, J. G. et al. Regulation of neural differentiation of ADMSCs using graphene-mediated wireless-localized electrical signals driven by electromagnetic induction. *Adv. Sci.* **2022**, *9*, 2104424.

[254] Sengwa, R. J.; Dhatarwal, P.; Choudhary, S. A comparative study of different metal oxide nanoparticles dispersed PVDF/PEO blend matrix-based advanced multifunctional nanodielectrics for flexible electronic devices. *Mater. Today Commun.* **2020**, *25*, 101380.

[255] Mishra, S.; Sahoo, R.; Unnikrishnan, L.; Ramadoss, A.; Mohanty, S.; Nayak, S. K. Enhanced structural and dielectric behaviour of PVDF-PLA binary polymeric blend system. *Mater. Today Commun.* **2021**, *26*, 101958.

[256] Zhang, H. Y.; Yin, F. F.; Shang, S.; Li, Y.; Qiu, Z. C.; Lin, Q. H.; Wei, X.; Li, S. L.; Kim, N. Y.; Shen, G. Z. A high-performance, biocompatible, and degradable piezoresistive-triboelectric hybrid device for cross-scale human activities monitoring and self-powered smart home system. *Nano Energy* **2022**, *102*, 107687.

[257] Wang, L. L.; Lou, Z.; Wang, K.; Zhao, S. F.; Yu, P. C.; Wei, W.; Wang, D. Y.; Han, W.; Jiang, K.; Shen, G. Z. Biocompatible and biodegradable functional polysaccharides for flexible humidity sensors. *Research (Wash. D C)* **2020**, *2020*, 8716847.

[258] Han, S. W.; Chen, D.; Wang, J.; Liu, Z.; Liu, F.; Chen, Y. K.; Ji, Y. C.; Pang, J. B.; Liu, H.; Wang, J. G. Assembling Sn_3O_4 nanostructures on a hydrophobic PVDF film through metal-F coordination to construct a piezotronic effect-enhanced Sn_3O_4/PVDF hybrid photocatalyst. *Nano Energy* **2020**, *72*, 104688.

[259] Cheng, Y.; Xu, Y.; Qian, Y.; Chen, X.; Ouyang, Y. M.; Yuan, W. E. 3D structured self-powered PVDF/PCL scaffolds for peripheral nerve regeneration. *Nano Energy* **2020**, *69*, 104411.

[260] Chen, J. L.; Rong, C. Y.; Lin, T. T.; Chen, Y. H.; Wu, J. L.; You, J. C.; Wang, H. T.; Li, Y. J. Stable co-continuous PLA/PBAT blends compatibilized by interfacial stereocomplex crystallites: Toward full biodegradable polymer blends with simultaneously enhanced mechanical properties and crystallization rates. *Macromolecules* **2021**, *54*, 2852–2861.

[261] Wang, L. L.; Lou, Z.; Jiang, K.; Shen, G. Z. Bio-multifunctional smart wearable sensors for medical devices. *Adv. Intell. Syst.* **2019**, *1*, 1900040.

[262] Luo, Y. F.; Wang, M.; Wan, C. J.; Cai, P. Q.; Loh, X. J.; Chen, X. D. Devising materials manufacturing toward lab-to-fab translation of flexible electronics. *Adv. Mater.* **2020**, *32*, 2001903.

[263] He, X.; Ni, Y. X.; Li, Y. X.; Sun, H. H.; Lu, Y.; Li, H. X.; Yan, Z. H.; Zhang, K.; Chen, J. An MXene-based metal anode with stepped sodiophilic gradient structure enables a large current density for rechargeable $Na-O_2$ batteries. *Adv. Mater.* **2022**, *34*, 2106565.

[264] Tang, J. Y.; Peng, X. Y.; Lin, T. E.; Huang, X.; Luo, B.; Wang, L. Z. Confining ultrafine tin monophosphide in $Ti_3C_2T_x$ interlayers for rapid and stable sodium ion storage. *eScience* **2021**, *1*, 203–211.

[265] He, X.; Jin, S.; Miao, L. C.; Cai, Y. C.; Hou, Y. P.; Li, H. X.; Zhang, K.; Yan, Z. H.; Chen, J. A 3D hydroxylated MXene/carbon nanotubes composite as a scaffold for dendrite-free sodium-metal electrodes. *Angew. Chem., Int. Ed.* **2020**, *59*, 16705–16711.

[266] Yu, Y.; Zhang, Q.; Chen, J.; Sun, S. G. Virtual special issue of recent research advances in China: Batteries and energy storage. *Energy Fuels* **2021**, *35*, 10945–10948.

[267] Wang, W. X.; Xiong, F. Y.; Zhu, S. H.; Chen, J. H.; Xie, J.; An, Q. Y. Defect engineering in molybdenum-based electrode materials for energy storage. *eScience* **2022**, *2*, 278–294.

[268] Shuck, C. E.; Gogotsi, Y. Taking MXenes from the lab to commercial products. *Chem. Eng. J.* **2020**, *401*, 125786.

[269] Feng, X.; Shi, X. Y.; Ning, J.; Wang, D.; Zhang, J. C.; Hao, Y.; Wu, Z. S. Recent advances in micro-supercapacitors for AC line-filtering performance: From fundamental models to emerging applications. *eScience* **2021**, *1*, 124–140.

[270] Lethien, C.; Le Bideau, J.; Brousse, T. Challenges and prospects of 3D micro-supercapacitors for powering the internet of things. *Energy Environ. Sci.* **2019**, *12*, 96–115.

[271] Robert, K.; Douard, C.; Demortière, A.; Blanchard, F.; Roussel, P.; Brousse, T.; Lethien, C. On chip interdigitated micro-supercapacitors based on sputtered bifunctional vanadium nitride thin films with finely tuned inter- and intracolumnar porosities. *Adv. Mater. Technol.* **2018**, *3*, 1800036.

[272] Boretti, A.; Castelletto, S. MXenes in polymer electrolyte membrane hydrogen fuel and electrolyzer cells. *Ceram. Int.*, in press, https://doi.org/10.1016/j.ceramint.2022.08.345.

[273] Zhang, T.; Zhang, L.; Hou, Y. L. MXenes: Synthesis strategies and lithium-sulfur battery applications. *eScience* **2022**, *2*, 164–182.

[274] Zhang, C. Y.; Zhang, C. Q.; Pan, J. L.; Sun, G. W.; Shi, Z. D.; Li, C. H.; Chang, X. Q.; Sun, G. Z.; Zhou, J. Y.; Cabot, A. Surface strain-enhanced MoS_2 as a high-performance cathode catalyst for lithium-sulfur batteries. *eScience* **2022**, *2*, 405–415.

[275] Ye, S. F.; Wang, L. F.; Liu, F. F.; Shi, P. C.; Yu, Y. Integration of homogeneous and heterogeneous nucleation growth via 3D alloy framework for stable Na/K metal anode. *eScience* **2021**, *1*, 75–82.

[276] Peng, M. K.; Wang, L.; Li, L. B.; Peng, Z. Y.; Tang, X. N.; Hu, T.; Yuan, K.; Chen, Y. W. Molecular crowding agents engineered to make bioinspired electrolytes for high-voltage aqueous supercapacitors. *eScience* **2021**, *1*, 83–90.

[277] Li, X.; Zhao, R. X.; Fu, Y. Z.; Manthiram, A. Nitrate additives for lithium batteries: Mechanisms, applications, and prospects. *eScience* **2021**, *1*, 108–123.

[278] Cheng, W. X.; Fu, J. M.; Hu, H. B.; Ho, D. Interlayer structure engineering of MXene-based capacitor-type electrode for hybrid micro-supercapacitor toward battery-level energy density. *Adv. Sci.* **2021**, *8*, 2100775.

[279] Ouendi, S.; Robert, K.; Stievenard, D.; Brousse, T.; Roussel, P.; Lethien, C. Sputtered tungsten nitride films as pseudocapacitive electrode for on chip micro-supercapacitors. *Energy Storage Mater.* **2019**, *20*, 243–252.

[280] Zhai, Y. J.; Han, P.; Yun, Q. B.; Ge, Y. Y.; Zhang, X.; Chen, Y.; Zhang, H. Phase engineering of metal nanocatalysts for electrochemical CO$_2$ reduction. *eScience* **2022**, *2*, 467–485.

[281] Xiao, X. X. The direct use of enzymatic biofuel cells as functional bioelectronics. *eScience* **2022**, *2*, 1–9.

[282] Sun, Z. Y.; Wen, X.; Wang, L. M.; Ji, D. X.; Qin, X. H.; Yu, J. Y.; Ramakrishna, S. Emerging design principles, materials, and applications for moisture-enabled electric generation. *eScience* **2022**, *2*, 32–46.

[283] Wang, S. L.; Wang, P. Y.; Chen, B. B.; Li, R. J.; Ren, N. Y.; Li, Y. C.; Shi, B.; Huang, Q.; Zhao, Y.; Grätzel, M. et al. Suppressed recombination for monolithic inorganic perovskite/silicon tandem solar cells with an approximate efficiency of 23%. *eScience* **2022**, *2*, 339–346.

[284] Shuck, C. E.; Sarycheva, A.; Anayee, M.; Levitt, A.; Zhu, Y. Z.; Uzun, S.; Balitskiy, V.; Zahorodna, V.; Gogotsi, O.; Gogotsi, Y. Scalable synthesis of Ti$_3$C$_2$T$_x$ MXene. *Adv. Eng. Mater.* **2020**, *22*, 1901241.

[285] Zheng, X. H.; Yao, L.; Qiu, Y. P.; Wang, S. R.; Zhang, K. Core−sheath porous polyaniline nanorods/graphene fiber-shaped supercapacitors with high specific capacitance and rate capability. *ACS Appl. Energy Mater.* **2019**, *2*, 4335–4344.

[286] Huang, L. Z.; Ding, L.; Wang, H. H. MXene-based membranes for separation applications. *Small Sci.* **2021**, *1*, 2100013.

[287] Zhao, Q.; Seredych, M.; Precetti, E.; Shuck, C. E.; Harhay, M.; Pang, R.; Shan, C. X.; Gogotsi, Y. Adsorption of uremic toxins using Ti$_3$C$_2$T$_x$ MXene for dialysate regeneration. *ACS Nano* **2020**, *14*, 11787–11798.

[288] Meng, F. Y.; Seredych, M.; Chen, C.; Gura, V.; Mikhalovsky, S.; Sandeman, S.; Ingavle, G.; Ozulumba, T.; Miao, L.; Anasori, B. et al. MXene sorbents for removal of urea from dialysate: A step toward the wearable artificial kidney. *ACS Nano* **2018**, *12*, 10518–10528.

[289] Sun, J. L.; Chang, Y.; Dong, L.; Zhang, K. K.; Hua, Q. L.; Zang, J. H.; Chen, Q. S.; Shang, Y. Y.; Pan, C. F.; Shan, C. X. MXene enhanced self-powered alternating current electroluminescence devices for patterned flexible displays. *Nano Energy* **2021**, *86*, 106077.

[290] Wang, J. Q.; Liu, L.; Jiao, S. L.; Ma, K. J.; Lv, J.; Yang, J. J. Hierarchical carbon Fiber@MXene@MoS$_2$ core-sheath synergistic microstructure for tunable and efficient microwave absorption. *Adv. Funct. Mater.* **2020**, *30*, 2002595.

[291] Lou, Z.; Wang, L. L.; Shen, G. Z. Recent advances in smart wearable sensing systems. *Adv. Mater. Technol.* **2018**, *3*, 1800444.

[292] Wang, L. L.; Jiang, K.; Shen, G. Z. Wearable, implantable, and interventional medical devices based on smart electronic skins. *Adv. Mater. Technol.* **2021**, *6*, 2100107.

[293] Chen, D.; Jiang, K.; Huang, T. T.; Shen, G. Z. Recent advances in fiber supercapacitors: Materials, device configurations, and applications. *Adv. Mater.* **2020**, *32*, 1901806.

[294] Jia, R.; Shen, G. Z.; Qu, F. Y.; Chen, D. Flexible on-chip micro-supercapacitors: Efficient power units for wearable electronics. *Energy Storage Mater.* **2020**, *27*, 169–186.

[295] Zhao, K.; Yang, J. H.; Zhong, M. Z.; Gao, Q.; Wang, Y.; Wang, X. T.; Shen, W. F.; Hu, C. G.; Wang, K. Y.; Shen, G. Z. et al. Direct polarimetric image sensor and wide spectral response based on quasi-1D Sb$_2$S$_3$ nanowire. *Adv. Funct. Mater.* **2021**, *31*, 2006601.

[296] Fang, J. Z.; Zhou, Z. Q.; Xiao, M. Q.; Lou, Z.; Wei, Z. M.; Shen, G. Z. Recent advances in low-dimensional semiconductor nanomaterials and their applications in high-performance photodetectors. *InfoMat* **2020**, *2*, 291–317.

[297] Cosson, M.; David, B.; Arzel, L.; Poizot, P.; Rhallabi, A. Modelling of photovoltaic production and electrochemical storage in an autonomous solar drone. *eScience* **2022**, *2*, 235–241.

[298] Zhang, Y. P.; Wang, L. L.; Zhao, L. J.; Wang, K.; Zheng, Y. Q.; Yuan, Z. Y.; Wang, D. Y.; Fu, X. Y.; Shen, G. Z.; Han, W. Flexible self-powered integrated sensing system with 3D periodic ordered black phosphorus@MXene thin-films. *Adv. Mater.* **2021**, *33*, 2007890.

[299] Guo, Z. L.; Gao, L. G.; Xu, Z. H.; Teo, S.; Zhang, C.; Kamata, Y.; Hayase, S.; Ma, T. L. High electrical conductivity 2D MXene serves as additive of perovskite for efficient solar cells. *Small* **2018**, *14*, 1802738.

[300] Cao, W. Z.; Li, Q.; Yu, X. Q.; Li, H. Controlling Li deposition below the interface. *eScience* **2022**, *2*, 47–78.

[301] Sun, C.; Wu, C. P.; Gu, X. X.; Wang, C.; Wang, Q. H. Interface engineering via Ti$_3$C$_2$T$_x$ MXene electrolyte additive toward dendrite-free zinc deposition. *Nano-Micro Lett.* **2021**, *13*, 89.

[302] Chen, D.; Lou, Z.; Jiang, K.; Shen, G. Z. Device configurations and future prospects of flexible/stretchable lithium-ion batteries. *Adv. Funct. Mater.* **2018**, *28*, 1805596.

[303] Huang, C.; Wang, Q. F.; Zhang, D. H.; Shen, G. Z. Coupling N-doping and rich oxygen vacancies in mesoporous ZnMn$_2$O$_4$ nanocages toward advanced aqueous zinc ion batteries. *Nano Res.* **2022**, *15*, 8118–8127.

[304] Shen, G. Z. Recent advances of flexible sensors for biomedical applications. *Prog. Nat. Sci. :Mater. Int.* **2021**, *31*, 872–882.

[305] Yuan, Z. Q.; Shen, G. Z.; Pan, C. F.; Wang, Z. L. Flexible sliding sensor for simultaneous monitoring deformation and displacement on a robotic hand/arm. *Nano Energy* **2020**, *73*, 104764.

[306] Wei, X.; Li, H.; Yue, W. J.; Gao, S.; Chen, Z. X.; Li, Y.; Shen, G. Z. A high-accuracy, real-time, intelligent material perception system with a machine-learning-motivated pressure-sensitive electronic skin. *Matter* **2022**, *5*, 1481–1501.

[307] Yuan, Z. Q.; Du, X. Y.; Niu, H. D.; Li, N. W.; Shen, G. Z.; Li, C. J.; Wang, Z. L. Motion recognition by a liquid filled tubular triboelectric nanogenerator. *Nanoscale* **2019**, *11*, 495–503.

[308] Wang, W. L.; Pang, J. B.; Su, J.; Li, F. J.; Li, Q.; Wang, X. X.; Wang, J. G.; Ibarlucea, B.; Liu, X. Y.; Li, Y. F. et al. Applications of nanogenerators for biomedical engineering and healthcare systems. *InfoMat* **2022**, *4*, e12262.

[309] Lou, Z.; Wang, L. L.; Jiang, K.; Shen, G. Z. Programmable three-dimensional advanced materials based on nanostructures as building blocks for flexible sensors. *Nano Today* **2019**, *26*, 176–198.

[310] Zhang, Y. T.; Poddar, S.; Huang, H.; Gu, L. L.; Zhang, Q. P.; Zhou, Y.; Yan, S.; Zhang, S. F.; Song, Z. T.; Huang, B. L. et al. Three-dimensional perovskite nanowire array-based ultrafast resistive RAM with ultralong data retention. *Sci. Adv.* **2021**, *7*, eabg3788.

[311] Wang, Y. Q.; Wang, W. X.; Zhang, C. W.; Kan, H.; Yue, W. J.; Pang, J. B.; Gao, S.; Li, Y. A digital-analog integrated memristor based on a ZnO NPs/CuO NWs heterostructure for neuromorphic computing. *ACS Appl. Electron. Mater.* **2022**, *4*, 3525–3534.

[312] Guo, Y. J.; Wei, X.; Gao, S.; Yue, W. J.; Li, Y.; Shen, G. Z. Recent advances in carbon material-based multifunctional sensors and their applications in electronic skin systems. *Adv. Funct. Mater.* **2021**, *31*, 2104288.

[313] Cai, G. F.; Ciou, J. H.; Liu, Y. Z.; Jiang, Y.; Lee, P. S. Leaf-inspired multiresponsive MXene-based actuator for programmable smart devices. *Sci. Adv.* **2019**, *5*, eaaw7956.

[314] Qu, X. C.; Liu, Z.; Tan, P. C.; Wang, C.; Liu, Y.; Feng, H. Q.; Luo, D.; Li, Z.; Wang, Z. L. Artificial tactile perception smart finger for material identification based on triboelectric sensing. *Sci. Adv.* **2022**, *8*, eabq2521.

[315] Seo, D. G.; Lee, Y.; Go, G. T.; Pei, M. Y.; Jung, S.; Jeong, Y. H.; Lee, W.; Park, H. L.; Kim, S. W.; Yang, H. et al. Versatile neuromorphic electronics by modulating synaptic decay of single organic synaptic transistor: From artificial neural networks to neuro-prosthetics. *Nano Energy* **2019**, *65*, 104035.

[316] Li, S.; Ma, L.; Zhou, M.; Li, Y. Q.; Xia, Y.; Fan, X.; Cheng, C.; Luo, H. R. New opportunities for emerging 2D materials in bioelectronics and biosensors. *Curr. Opin. Biomed. Eng.* **2020**, *13*, 32–41.

[317] Li, P. J.; Ali, H. P. A.; Cheng, W.; Yang, J. Y.; Tee, B. C. K. Bioinspired prosthetic interfaces. *Adv. Mater. Technol.* **2020**, *5*, 1900856.

[318] Niu, H. S.; Zhang, H. Y.; Yue, W. J.; Gao, S.; Kan, H.; Zhang, C. W.; Zhang, C. C.; Pang, J. B.; Lou, Z.; Wang, L. L. et al. Micronano processing of active layers in flexible tactile sensors via template methods: A review. *Small* **2021**, *17*, 2100804.

[319] Xia, G. T.; Huang, Y. N.; Li, F. J.; Wang, L. C.; Pang, J. B.; Li, L. W.; Wang, K. A thermally flexible and multi-site tactile sensor for remote 3D dynamic sensing imaging. *Front. Chem. Sci. Eng.* **2020**, *14*, 1039–1051.

[320] Shi, J. L.; Jie, J. S.; Deng, W.; Luo, G.; Fang, X. C.; Xiao, Y. L.; Zhang, Y. J.; Zhang, X. J.; Zhang, X. H. A fully solution-printed photosynaptic transistor array with ultralow energy consumption for artificial-vision neural networks. *Adv. Mater.* **2022**, *34*, 2200380.

[321] Chang, T. H.; Li, K. R.; Yang, H. T.; Chen, P. Y. Multifunctionality and mechanical actuation of 2D materials for skin-mimicking capabilities. *Adv. Mater.* **2018**, *30*, 1802418.

[322] Berco, D.; Ang, D. S. Recent progress in synaptic devices paving the way toward an artificial cogni-retina for bionic and machine vision. *Adv. Intell. Syst.* **2019**, *1*, 1900003.

[323] Alpala, L. O.; Quiroga-Parra, D. J.; Torres, J. C.; Peluffo-Ordóñez, D. H. Smart factory using virtual reality and online multi-user: Towards a metaverse for experimental frameworks. *Appl. Sci.* **2022**, *12*, 6258.

[324] Zhou, Y. H.; Xiao, X.; Chen, G. R.; Zhao, X.; Chen, J. Self-powered sensing technologies for human Metaverse interfacing. *Joule* **2022**, *6*, 1381–1389.

[325] Tang, F. X.; Chen, X. H.; Zhao, M.; Kato, N. The roadmap of communication and networking in 6G for the metaverse. *IEEE Wirel. Commun.*, in press, https://doi.org/10.1109/MWC.019.2100721.

[326] Bibri, S. E. The social shaping of the metaverse as an alternative to the imaginaries of data-driven smart Cities: A study in science, technology, and society. *Smart Cities* **2022**, *5*, 832–874.

[327] Yang, Q.; Zhang, F.; Zhang, N. Y.; Zhang, H. Few-layer MXene $Ti_3C_2T_x$ (T = F, O, or OH) saturable absorber for visible bulk laser. *Opt. Mater. Express* **2019**, *9*, 1795–1802.

[328] Bharathan, G.; Xu, L. Y.; Jiang, X. T.; Zhang, H.; Li, Z. Q.; Chen, F.; Fuerbach, A. MXene and $PtSe_2$ saturable absorbers for all-fibre ultrafast mid-infrared lasers. *Opt. Mater. Express* **2021**, *11*, 1898.

[329] Ma, C. Y.; Huang, W. C.; Wang, Y. Z.; Adams, J.; Wang, Z. H.; Liu, J.; Song, Y. F.; Ge, Y. Q.; Guo, Z. Y.; Hu, L. P. et al. MXene saturable absorber enabled hybrid mode-locking technology: A new routine of advancing femtosecond fiber lasers performance. *Nanophotonics* **2020**, *9*, 2451–2458.

[330] Wu, Q.; Jin, X.; Chen, S.; Jiang, X.; Hu, Y.; Jiang, Q.; Wu, L.; Li, J.; Zheng, Z.; Zhang, M. et al. MXene-based saturable absorber for femtosecond mode-locked fiber lasers. *Opt. Express* **2019**, *27*, 10159–10170.

[331] Hao, Q. Q.; Liu, J. J.; Zhang, Z.; Zhang, B.; Zhang, F.; Yang, J. M.; Liu, J.; Su, L. B.; Zhang, H. Mid-infrared Er: CaF_2-SrF_2 bulk laser Q-switched by MXene $Ti_3C_2T_x$ absorber. *Appl. Phys. Express* **2019**, *12*, 085506.

[332] Feng, T. C.; Li, X. H.; Guo, P. L.; Zhang, Y.; Liu, J. S.; Zhang, H. MXene: Two dimensional inorganic compounds, for generation of bound state soliton pulses in nonlinear optical system. *Nanophotonics* **2020**, *9*, 2505–2513.

[333] Wu, Q.; Wang, Y. Z.; Huang, W. C.; Wang, C.; Zheng, Z.; Zhang, M.; Zhang, H. MXene-based high-performance all-optical modulators for actively Q-switched pulse generation. *Photonics Res.* **2020**, *8*, 1140–1147.

[334] Wu, L. M.; Jiang, X. T.; Zhao, J. L.; Liang, W. Y.; Li, Z. J.; Huang, W. C.; Lin, Z. T.; Wang, Y. Z.; Zhang, F.; Lu, S. B. et al. MXene-based nonlinear optical information converter for all-optical modulator and switcher. *Laser Photonics Rev.* **2018**, *12*, 1800215.

[335] Wu, Q.; Chen, S.; Wang, Y. Z.; Wu, L. M.; Jiang, X. T.; Zhang, F.; Jin, X. X.; Jiang, Q. Y.; Zheng, Z.; Li, J. Q. et al. MZI-based all-optical modulator using MXene $Ti_3C_2T_x$ (T = F, O, or OH) deposited microfiber. *Adv. Mater. Technol.* **2019**, *4*, 1800532.

[336] Song, Y. F.; Chen, Y. X.; Jiang, X. T.; Ge, Y. Q.; Wang, Y. Z.; You, K. X.; Wang, K.; Zheng, J. L.; Ji, J. H.; Zhang, Y. P. et al. Nonlinear few-layer MXene-assisted all-optical wavelength conversion at telecommunication band. *Adv. Opt. Mater.* **2019**, *7*, 1801777.

[337] Jiang, X. T.; Li, W. J.; Hai, T.; Yue, R.; Chen, Z. W.; Lao, C. S.; Ge, Y. Q.; Xie, G. Q.; Wen, Q.; Zhang, H. Inkjet-printed MXene micro-scale devices for integrated broadband ultrafast photonics. *npj 2D Mater. Appl.* **2019**, *3*, 34.

[338] Wang, C.; Xu, J. W.; Wang, Y. Z.; Song, Y. F.; Guo, J.; Huang, W. C.; Ge, Y. Q.; Hu, L. P.; Liu, J.; Zhang, H. MXene (Ti_2NT_x): Synthesis, characteristics and application as a thermo-optical switcher for all-optical wavelength tuning laser. *Sci. China Mater.* **2021**, *64*, 259–265.

[339] Shi, Z.; Khaledialidusti, R.; Malaki, M.; Zhang, H. MXene-based materials for solar cell applications. *Nanomaterials* **2021**, *11*, 3170.

[340] Zhu, J.; Ha, E. N.; Zhao, G. L.; Zhou, Y.; Huang, D. S.; Yue, G. Z.; Hu, L. S.; Sun, N.; Wang, Y.; Lee, L. Y. S. et al. Recent advance in MXenes: A promising 2D material for catalysis, sensor and chemical adsorption. *Coord. Chem. Rev.* **2017**, *352*, 306–327.

[341] Zhang, Y. J.; Wang, L.; Zhang, N. N.; Zhou, Z. J. Adsorptive environmental applications of MXene nanomaterials: A review. *RSC Adv.* **2018**, *8*, 19895–19905.

[342] Sinha, A.; Dhanjai; Zhao, H. M.; Huang, Y. J.; Lu, X. B.; Chen, J. P.; Jain, R. MXene: An emerging material for sensing and biosensing. *TrAC Trends Anal. Chem.* **2018**, *105*, 424–435.

[343] Gao, L. F.; Chen, H. L.; Zhang, F.; Mei, S.; Zhang, Y.; Bao, W. L.; Ma, C. Y.; Yin, P.; Guo, J.; Jiang, X. T. et al. Ultrafast relaxation dynamics and nonlinear response of few-layer niobium carbide MXene. *Small Methods* **2020**, *4*, 2000250.

[344] Wang, Y. D.; Wang, Y. W.; Chen, K. Q.; Qi, K.; Xue, T. Y.; Zhang, H.; He, J.; Xiao, S. Niobium carbide MXenes with broad-band nonlinear optical response and ultrafast carrier dynamics. *ACS Nano* **2020**, *14*, 10492–10502.

[345] Wang, C.; Wang, Y. Z.; Jiang, X. T.; Xu, J. W.; Huang, W. C.; Zhang, F.; Liu, J. F.; Yang, F. M.; Song, Y. F.; Ge, Y. Q. et al. MXene $Ti_3C_2T_x$: A promising photothermal conversion material and application in all-optical modulation and all-optical information loading. *Adv. Opt. Mater.* **2019**, *7*, 1900060.

[346] Jiang, X. T.; Liu, S. X.; Liang, W. Y.; Luo, S. J.; He, Z. L.; Ge, Y. Q.; Wang, H. D.; Cao, R.; Zhang, F.; Wen, Q. et al. Broadband nonlinear photonics in few-layer MXene $Ti_3C_2T_x$ (T = F, O, or OH). *Laser Photonics Rev.* **2018**, *12*, 1700229.

[347] Huang, W. C.; Ma, C. Y.; Li, C.; Zhang, Y.; Hu, L. P.; Chen, T. T.; Tang, Y. F.; Ju, J. F.; Zhang, H. Highly stable MXene (V_2CT_x)-based harmonic pulse generation. *Nanophotonics* **2020**, *9*, 2577–2585.

[348] Gao, L. F.; Chen, H. L.; Kuklin, A. V.; Wageh, S.; Al-Ghamdi, A. A.; Ågren, H.; Zhang, H. Optical properties of few-layer Ti_3CN MXene: From experimental observations to theoretical calculations. *ACS Nano* **2022**, *16*, 3059–3069.

[349] Gogotsi, Y.; Huang, Q. MXenes: Two-dimensional building blocks for future materials and devices. *ACS Nano* **2021**, *15*, 5775–5780.

[350] Chen, J. J.; Jin, Q. Q.; Li, Y. B.; Shao, H.; Liu, P. C.; Liu, Y.; Taberna, P. L.; Huang, Q.; Lin, Z. F.; Simon, P. Molten salt-shielded synthesis (MS_3) of MXenes in air. *Energy Environ. Mater.*, in press, https://doi.org/10.1002/eem2.12328.

[351] Wan, S. J.; Li, X.; Chen, Y.; Liu, N. N.; Du, Y.; Dou, S. X.; Jiang, L.; Cheng, Q. F. High-strength scalable MXene films through bridging-induced densification. *Science* **2021**, *374*, 96–99.

[352] Li, Y. B.; Shao, H.; Lin, Z. F.; Lu, J.; Liu, L. Y.; Duployer, B.; Persson, P. O. Å.; Eklund, P.; Hultman, L.; Li, M. et al. A general Lewis acidic etching route for preparing MXenes with enhanced electrochemical performance in non-aqueous electrolyte. *Nat. Mater.* **2020**, *19*, 894–899.

[353] Li, X. L.; Li, N.; Huang, Z. D.; Chen, Z.; Zhao, Y. W.; Liang, G. J.; Yang, Q.; Li, M.; Huang, Q.; Dong, B. B. et al. Confining aqueous Zn-Br halide redox chemistry by $Ti_3C_2T_x$ MXene. *ACS Nano* **2021**, *15*, 1718–1726.

[354] Fang, W.; Du, C. F.; Kuang, M.; Chen, M. X.; Huang, W. J.; Ren,

H.; Xu, J. W.; Feldhoff, A.; Yan, Q. Y. Boosting efficient ambient nitrogen oxidation by a well-dispersed Pd on MXene electrocatalyst. *Chem. Commun.* **2020**, *56*, 5779–5782.

[355] Du, C. F.; Dinh, K. N.; Liang, Q. H.; Zheng, Y.; Luo, Y. B.; Zhang, J. L.; Yan, Q. Y. Self-assemble and *in situ* formation of $Ni_{1-x}Fe_xPS_3$ nanomosaic-decorated MXene hybrids for overall water splitting. *Adv. Energy Mater.* **2018**, *8*, 1801127.

[356] Du, C. F.; Sun, X. L.; Yu, H.; Liang, Q. H.; Dinh, K. N.; Zheng, Y.; Luo, Y. B.; Wang, Z. G.; Yan, Q. Y. Synergy of Nb doping and surface alloy enhanced on water-alkali electrocatalytic hydrogen generation performance in Ti-based MXene. *Adv. Sci.* **2019**, *6*, 1900116.

[357] Du, C. F.; Sun, X. L.; Yu, H.; Fang, W.; Jing, Y.; Wang, Y. H.; Li, S. Q.; Liu, X. H.; Yan, Q. Y. $V_4C_3T_x$ MXene: A promising active substrate for reactive surface modification and the enhanced electrocatalytic oxygen evolution activity. *InfoMat* **2020**, *2*, 950–959.

[358] Yu, H.; Wang, Y. H.; Jing, Y.; Ma, J. M.; Du, C. F.; Yan, Q. Y. Surface modified MXene-based nanocomposites for electrochemical energy conversion and storage. *Small* **2019**, *15*, 1901503.

[359] Du, C. F.; Yang, L.; Tang, K. W.; Fang, W.; Zhao, X. Y.; Liang, Q. H.; Liu, X. H.; Yu, H.; Qi, W. H.; Yan, Q. Y. Ni nanoparticles/$V_4C_3T_x$ MXene heterostructures for electrocatalytic nitrogen fixation. *Mater. Chem. Front.* **2021**, *5*, 2338–2346.

[360] Xu, C.; Wang, L. B.; Liu, Z. B.; Chen, L.; Guo, J. K.; Kang, N.; Ma, X. L.; Cheng, H. M.; Ren, W. C. Large-area high-quality 2D ultrathin Mo_2C superconducting crystals. *Nat. Mater.* **2015**, *14*, 1135–1141.

[361] Sahare, S.; Ghoderao, P.; Yin, P.; Saleemi, A. S.; Lee, S. L.; Chan, Y.; Zhang, H. An assessment of MXenes through scanning probe microscopy. *Small Methods* **2022**, *6*, 2101599.

[362] Li, X. L.; Li, Q.; Hou, Y.; Yang, Q.; Chen, Z.; Huang, Z. D.; Liang, G. J.; Zhao, Y. W.; Ma, L. T.; Li, M. et al. Toward a practical Zn powder anode: $Ti_3C_2T_x$ MXene as a lattice-match electrons/ions redistributor. *ACS Nano* **2021**, *15*, 14631–14642.

[363] Li, X. L.; Li, M.; Luo, K.; Hou, Y.; Li, P.; Yang, Q.; Huang, Z. D.; Liang, G. J.; Chen, Z.; Du, S. Y. et al. Lattice matching and halogen regulation for synergistically induced uniform zinc electrodeposition by halogenated Ti_3C_2 MXenes. *ACS Nano* **2022**, *16*, 813–822.

[364] Li, X. L.; Ma, X. Y.; Hou, Y.; Zhang, Z. H.; Lu, Y.; Huang, Z. D.; Liang, G. J.; Li, M.; Yang, Q.; Ma, J. L. et al. Intrinsic voltage plateau of a Nb_2CT_x MXene cathode in an aqueous electrolyte induced by high-voltage scanning. *Joule* **2021**, *5*, 2993–3005.

[365] Li, X. L.; Li, N.; Huang, Z. D.; Chen, Z.; Liang, G. J.; Yang, Q.; Li, M.; Zhao, Y. W.; Ma, L. T.; Dong, B. B. et al. Enhanced redox kinetics and duration of aqueous I_2/I^- conversion chemistry by MXene confinement. *Adv. Mater.* **2021**, *33*, 2006897.

[366] Wang, L.; Song, P.; Lin, C. T.; Kong, J.; Gu, J. W. 3D shapeable, superior electrically conductive cellulose nanofibers/$Ti_3C_2T_x$ MXene aerogels/epoxy nanocomposites for promising EMI shielding. *Research (Wash. D C)* **2020**, *2020*, 4093732.

[367] Cheng, Y.; Li, X. Y.; Qin, Y. X.; Fang, Y. T.; Liu, G. L.; Wang, Z. Y.; Matz, J.; Dong, P.; Shen, J. F.; Ye, M. X. Hierarchically porous polyimide/$Ti_3C_2T_x$ film with stable electromagnetic interference shielding after resisting harsh conditions. *Sci. Adv.* **2021**, *7*, eabj1663.

[368] Li, X. L.; Li, M. H.; Li, X.; Fan, X. M.; Zhi, C. Y. Low infrared emissivity and strong stealth of Ti-based MXenes. *Research (Wash. D C)* **2022**, *2022*, 9892628.

[369] Iqbal, A.; Sambyal, P.; Koo, C. M. 2D MXenes for electromagnetic shielding: A review. *Adv. Funct. Mater.* **2020**, *30*, 2000883.

[370] Cao, M. S.; Cai, Y. Z.; He, P.; Shu, J. C.; Cao, W. Q.; Yuan, J. 2D MXenes: Electromagnetic property for microwave absorption and electromagnetic interference shielding. *Chem. Eng. J.* **2019**, *359*, 1265–1302.

[371] Lu, X. F.; Zhang, Q. H.; Liao, J. C.; Chen, H. Y.; Fan, Y. C.; Xing, J. J.; Gu, S. J.; Huang, J. L.; Ma, J. X.; Wang, J. C. et al. High-efficiency thermoelectric power generation enabled by homogeneous incorporation of MXene in $(Bi, Sb)_2Te_3$ matrix. *Adv. Energy Mater.* **2020**, *10*, 1902986.

[372] Diao, J. L.; Yuan, J.; Cai, Z. H.; Xia, L.; Cheng, Z.; Liu, X. Y.; Ma, W. L.; Wang, S. F.; Huang, Y. High-performance electromagnetic interference shielding and thermoelectric conversion derived from multifunctional $Bi_2Te_{2.7}Se_{0.3}$/MXene composites. *Carbon* **2022**, *196*, 243–252.

[373] Sarikurt, S.; Çakır, D.; Keçeli, M.; Sevik, C. The influence of surface functionalization on thermal transport and thermoelectric properties of MXene monolayers. *Nanoscale* **2018**, *10*, 8859–8868.

[374] Fashandi, H.; Dahlqvist, M.; Lu, J.; Palisaitis, J.; Simak, S. I.; Abrikosov, I. A.; Rosen, J.; Hultman, L.; Andersson, M.; Spetz, A. L. et al. Synthesis of Ti_3AuC_2, $Ti_3Au_2C_2$ and Ti_3IrC_2 by noble metal substitution reaction in Ti_3SiC_2 for high-temperature-stable Ohmic contacts to SiC. *Nat. Mater.* **2017**, *16*, 814–818.

[375] Li, M.; Lu, J.; Luo, K.; Li, Y. B.; Chang, K. K.; Chen, K.; Zhou, J.; Rosen, J.; Hultman, L.; Eklund, P. et al. Element replacement approach by reaction with lewis acidic molten salts to synthesize nanolaminated MAX phases and MXenes. *J. Am. Chem. Soc.* **2019**, *141*, 4730–4737.

[376] Zhang, X.; Zhang, M. T.; Deng, Y. C.; Xu, M. Q.; Artiglia, L.; Wen, W.; Gao, R.; Chen, B. B.; Yao, S. Y.; Zhang, X. C. et al. A stable low-temperature H_2-production catalyst by crowding Pt on α-MoC. *Nature* **2021**, *589*, 396–401.

[377] Hong, Y. L.; Liu, Z. B.; Wang, L.; Zhou, T. Y.; Ma, W.; Xu, C.; Feng, S.; Chen, L.; Chen, M. L.; Sun, D. M. et al. Chemical vapor deposition of layered two-dimensional $MoSi_2N_4$ materials. *Science* **2020**, *369*, 670–674.

[378] Salim, O.; Mahmoud, K. A.; Pant, K. K.; Joshi, R. K. Introduction to MXenes: Synthesis and characteristics. *Mater. Today Chem.* **2019**, *14*, 100191.

[379] Park, G. S.; Ho, D. H.; Lyu, B. Z.; Jeon, S.; Ryu, D. Y.; Kim, D. W.; Lee, N.; Kim, S.; Song, Y. J.; Jo, S. B. et al. Comb-type polymer-hybridized MXene nanosheets dispersible in arbitrary polar, nonpolar, and ionic solvents. *Sci. Adv.* **2022**, *8*, eabl5299.

[380] Pang, J. B.; Chang, B.; Liu, H.; Zhou, W. J. Potential of MXene-based heterostructures for energy conversion and storage. *ACS Energy Lett.* **2022**, *7*, 78–96.

[381] Wang, L.; Zhang, M. Y.; Yang, B.; Tan, J. J.; Ding, X. Y.; Li, W. W. Recent advances in multidimensional (1D, 2D, and 3D) composite sensors derived from MXene: Synthesis, structure, application, and perspective. *Small Methods* **2021**, *5*, 2100409.

[382] Pang, J. B.; Mendes, R. G.; Bachmatiuk, A.; Zhao, L.; Ta, H. Q.; Gemming, T.; Liu, H.; Liu, Z. F.; Rummeli, M. H. Applications of 2D MXenes in energy conversion and storage systems. *Chem. Soc. Rev.* **2019**, *48*, 72–133.

[383] Liu, N.; Li, Q. Q.; Wan, H. J.; Chang, L. B.; Wang, H.; Fang, J. H.; Ding, T. P.; Wen, Q. Y.; Zhou, L. J.; Xiao, X. High-temperature stability in air of $Ti_3C_2T_x$ MXene-based composite with extracted bentonite. *Nat. Commun.* **2022**, *13*, 5551.

[384] Chen, H. L.; Gao, L. F.; Al-Hartomy, O. A.; Zhang, F.; Al-Ghamdi, A.; Guo, J.; Song, Y. F.; Wang, Z. H.; Algarni, H.; Wang, C. et al. Tailoring the ultrafast and nonlinear photonics of MXenes through elemental replacement. *Nanoscale* **2021**, *13*, 15891–15898.

[385] Yue, Y.; Liu, N. S.; Liu, W. J.; Li, M.; Ma, Y. N.; Luo, C.; Wang, S. L.; Rao, J. Y.; Hu, X. K.; Su, J. et al. 3D hybrid porous Mxene-sponge network and its application in piezoresistive sensor. *Nano Energy* **2018**, *50*, 79–87.

[386] Nasrin, K.; Sudharshan, V.; Subramani, K.; Sathish, M. Insights into 2D/2D MXene heterostructures for improved synergy in structure toward next-generation supercapacitors: A review. *Adv. Funct. Mater.* **2022**, *32*, 2110267.

[387] Lu, Y.; Qu, X. Y.; Zhao, W.; Ren, Y. F.; Si, W. L.; Wang, W. J.; Wang, Q.; Huang, W.; Dong, X. C. Highly stretchable, elastic, and sensitive MXene-based hydrogel for flexible strain and pressure sensors. *Research (Wash. D C)* **2020**, *2020*, 2038560.

[388] Zhang, S.; Pang, J. B.; Li, Y. F.; Yang, F.; Gemming, T.; Wang, K.; Wang, X.; Peng, S. A.; Liu, X. Y.; Chang, B. et al. Emerging Internet of Things driven carbon nanotubes-based devices. *Nano Res.* **2022**, *15*, 4613–4637.

[389] Pang, J. B.; Bachmatiuk, A.; Yang, F.; Liu, H.; Zhou, W. J.; Rümmeli, M. H.; Cuniberti, G. Applications of carbon nanotubes in the internet of things era. *Nano-Micro Lett.* **2021**, *13*, 191.

[390] Sreenilayam, S. P.; Ul Ahad, I.; Nicolosi, V.; Brabazon, D. MXene materials based printed flexible devices for healthcare, biomedical and energy storage applications. *Mater. Today* **2021**, *43*, 99–131.

[391] Ahmed, A.; Sharma, S.; Adak, B.; Hossain, M.; LaChance, A. M.; Mukhopadhyay, S.; Sun, L. Y. Two-dimensional MXenes: New frontier of wearable and flexible electronics. *InfoMat* **2022**, *4*, e12295.

[392] Ma, C.; Ma, M. G.; Si, C. L.; Ji, X. X.; Wan, P. B. Flexible MXene-based composites for wearable devices. *Adv. Funct. Mater.* **2021**, *31*, 2009524.

[393] Simon, P.; Gogotsi, Y. Perspectives for electrochemical capacitors and related devices. *Nat. Mater.* **2020**, *19*, 1151–1163.

[394] Ling, J.; Kunwar, R.; Li, L. L.; Peng, S. J.; Misnon, I. I.; Rahim, M. H. A.; Yang, C. C.; Jose, R. Self-rechargeable energizers for sustainability. *eScience* **2022**, *2*, 347–364.

[395] Ding, G. L.; Zeng, K. L.; Zhou, K.; Li, Z. X.; Zhou, Y.; Zhai, Y. B.; Zhou, L.; Chen, X. L.; Han, S. T. Configurable multi-state non-volatile memory behaviors in Ti_3C_2 nanosheets. *Nanoscale* **2019**, *11*, 7102–7110.

[396] Gong, Y.; Xing, X. C.; Wang, Y.; Lv, Z. Y.; Zhou, Y.; Han, S. T. Emerging MXenes for functional memories. *Small Sci.* **2021**, *1*, 2100006.

[397] Ding, G. L.; Yang, B. D.; Chen, R. S.; Zhou, K.; Han, S. T.; Zhou, Y. MXenes for memristive and tactile sensory systems. *Appl. Phys. Rev.* **2021**, *8*, 011316.

[398] Wang, Y.; Gong, Y.; Yang, L.; Xiong, Z. Y.; Lv, Z. Y.; Xing, X. C.; Zhou, Y.; Zhang, B.; Su, C. L.; Liao, Q. F. et al. MXene-ZnO memristor for multimodal in-sensor computing. *Adv. Funct. Mater.* **2021**, *31*, 2100144.

[399] Guo, L. C.; Mu, B. Y.; Li, M. Z.; Yang, B. D.; Chen, R. S.; Ding, G. L.; Zhou, K.; Liu, Y. H.; Kuo, C. C.; Han, S. T. et al. Stacked two-dimensional MXene composites for an energy-efficient memory and digital comparator. *ACS Appl. Mater. Interfaces* **2021**, *13*, 39595–39605.

[400] Wang, S. Y.; Chen, X. Z.; Huang, X. H.; Zhang, D. W.; Zhou, P. Neuromorphic engineering for hardware computational acceleration and biomimetic perception motion integration. *Adv. Intel. Syst.* **2020**, *2*, 2000124.

[401] Yan, X. B.; Wang, K. Y.; Zhao, J. H.; Zhou, Z. Y.; Wang, H.; Wang, J. J.; Zhang, L.; Li, X. Y.; Xiao, Z. A.; Zhao, Q. L. et al. A new memristor with 2D $Ti_3C_2T_x$ MXene flakes as an artificial bio-synapse. *Small* **2019**, *15*, 1900107.

[402] Bian, J. H.; Cao, Z. Y.; Zhou, P. Neuromorphic computing: Devices, hardware, and system application facilitated by two-dimensional materials. *Appl. Phys. Rev.* **2021**, *8*, 041313.

[403] Huang, M. N.; Gu, Z. Y.; Zhang, J. G.; Zhang, D.; Zhang, H.; Yang, Z. G.; Qu, J. L. MXene and black phosphorus based 2D nanomaterials in bioimaging and biosensing: Progress and perspectives. *J. Mater. Chem. B* **2021**, *9*, 5195–5220.

[404] Xing, C. Y.; Chen, S. Y.; Liang, X.; Liu, Q.; Qu, M. M.; Zou, Q. S.; Li, J. H.; Tan, H.; Liu, L. P.; Fan, D. Y. et al. Two-dimensional MXene (Ti_3C_2)-integrated cellulose hydrogels: Toward smart three-dimensional network nanoplatforms exhibiting light-induced swelling and bimodal photothermal/chemotherapy anticancer activity. *ACS Appl. Mater. Interfaces* **2018**, *10*, 27631–27643.

[405] Xu, Y. J.; Wang, Y. W.; An, J.; Sedgwick, A. C.; Li, M. L.; Xie, J. L.; Hu, W. B.; Kang, J. L.; Sen, S.; Steinbrueck, A. et al. 2D-ultrathin MXene/DOXjade platform for iron chelation chemo-photothermal therapy. *Bioact. Mater.* **2022**, *14*, 76–85.

[406] Dang, S. S.; Mo, Y. M.; Zeng, J. Q.; Xu, Y. J.; Xie, Z. J.; Zhang, H.; Zhang, B.; Nie, G. H. Three birds with one stone: Oxygen self-supply engineering palladium nanocluster/titanium carbide hybrid for single-NIR laser-triggered synergistic photodynamic-photothermal therapy. *Nanophotonics*, in press, https://doi.org/10.1515/nanoph-2022-0268.

[407] Xie, Z. J.; Chen, S. Y.; Duo, Y. H.; Zhu, Y.; Fan, T. J.; Zou, Q. S.; Qu, M. M.; Lin, Z. T.; Zhao, J. L.; Li, Y. et al. Biocompatible two-dimensional titanium nanosheets for multimodal imaging-guided cancer theranostics. *ACS Appl. Mater. Interfaces* **2019**, *11*, 22129–22140.

[408] Lin, H.; Chen, Y.; Shi, J. L. Insights into 2D MXenes for versatile biomedical applications: Current advances and challenges ahead. *Adv. Sci.* **2018**, *5*, 1800518.

[409] Hao, S. Y.; Han, H. C.; Yang, Z. Y.; Chen, M. T.; Jiang, Y. Y.; Lu, G. X.; Dong, L.; Wen, H. L.; Li, H.; Liu, J. R. et al. Recent advancements on photothermal conversion and antibacterial applications over MXenes-based materials. *Nano-Micro Lett.* **2022**, *14*, 178.

[410] Liu, L.; Zhu, M. H.; Ma, Z. W.; Xu, X. D.; Seraji, S. M.; Yu, B.; Sun, Z. Q.; Wang, H.; Song, P. A. A reactive copper-organophosphate-MXene heterostructure enabled antibacterial, self-extinguishing and mechanically robust polymer nanocomposites. *Chem. Eng. J.* **2022**, *430*, 132712.

[411] Iravani, S.; Varma, R. S. MXenes and MXene-based materials for tissue engineering and regenerative medicine: Recent advances. *Mater. Adv.* **2021**, *2*, 2906–2917.

[412] Tang, Z. M.; Xiao, Y. F.; Kong, N.; Liu, C.; Chen, W.; Huang, X. G.; Xu, D. Y.; Ouyang, J.; Feng, C.; Wang, C. et al. Nano-bio interfaces effect of two-dimensional nanomaterials and their applications in cancer immunotherapy. *Acta Pharm. Sin. B* **2021**, *11*, 3447–3464.

[413] Khan, K.; Tareen, A. K.; Iqbal, M.; Mahmood, A.; Mahmood, N.; Shi, Z.; Yin, J. D.; Qing, D.; Ma, C. Y.; Zhang, H. Recent development in graphdiyne and its derivative materials for novel biomedical applications. *J. Mater. Chem. B* **2021**, *9*, 9461–9484.

[414] Duo, Y. H.; Xie, Z. J.; Wang, L. D.; Abbasi, N. M.; Yang, T. Q.; Li, Z. H.; Hu, G. X.; Zhang, H. Borophene-based biomedical applications: Status and future challenges. *Coord. Chem. Rev.* **2021**, *427*, 213549.

[415] Kong, N.; Ji, X. Y.; Wang, J. Q.; Sun, X. N.; Chen, G. Q.; Fan, T. J.; Liang, W. Y.; Zhang, H.; Xie, A. Y.; Farokhzad, O. C. et al. ROS-mediated selective killing effect of black phosphorus: Mechanistic understanding and its guidance for safe biomedical applications. *Nano Lett.* **2020**, *20*, 3943–3955.

[416] Tang, Z. M.; Kong, N.; Ouyang, J.; Feng, C.; Kim, N. Y.; Ji, X. Y.; Wang, C.; Farokhzad, O. C.; Zhang, H.; Tao, W. Phosphorus science-oriented design and synthesis of multifunctional nanomaterials for biomedical applications. *Matter* **2020**, *2*, 297–322.

[417] Xie, Z. J.; Wang, D.; Fan, T. J.; Xing, C. Y.; Li, Z. J.; Tao, W.; Liu, L. P.; Bao, S. Y.; Fan, D. Y.; Zhang, H. Black phosphorus analogue tin sulfide nanosheets: Synthesis and application as near-infrared photothermal agents and drug delivery platforms for cancer therapy. *J. Mater. Chem. B* **2018**, *6*, 4747–4755.

[418] Yang, X.; Zhang, C. Q.; Deng, D. W.; Gu, Y. Q.; Wang, H.; Zhong, Q. F. Multiple stimuli-responsive MXene-based hydrogel as intelligent drug delivery carriers for deep chronic wound healing. *Small* **2022**, *18*, 2104368.

[419] Cui, D.; Kong, N.; Ding, L.; Guo, Y. C.; Yang, W. R.; Yan, F. H. Ultrathin 2D titanium carbide MXene ($Ti_3C_2T_x$) nanoflakes activate WNT/HIF-1α-mediated metabolism reprogramming for periodontal regeneration. *Adv. Healthc. Mater.* **2021**, *10*, 2101215.

[420] Rafieerad, A.; Yan, W. A.; Alagarsamy, K. N.; Srivastava, A.; Sareen, N.; Arora, R. C.; Dhingra, S. Fabrication of smart tantalum carbide MXene quantum dots with intrinsic immunomodulatory properties for treatment of allograft vasculopathy. *Adv. Funct. Mater.* **2021**, *31*, 2106786.

[421] Pan, S. S.; Yin, J. H.; Yu, L. D.; Zhang, C. Q.; Zhu, Y. F.; Gao, Y. S.; Chen, Y. 2D MXene-integrated 3D-printing scaffolds for augmented osteosarcoma phototherapy and accelerated tissue reconstruction. *Adv. Sci.* **2020**, *7*, 1901511.

[422] Fan, T. J.; Yan, L.; He, S. L.; Hong, Q. C.; Ai, F. J.; He, S. Q.; Ji, T.; Hu, X.; Ha, E. N.; Zhang, B. et al. Biodistribution, degradability and clearance of 2D materials for their biomedical applications. *Chem. Soc. Rev.* **2022**, *51*, 7732–7751.

[423] Umrao, S.; Tabassian, R.; Kim, J.; Nguyen, V. H.; Zhou, Q. T.; Nam, S.; Oh, I. K. MXene artificial muscles based on ionically cross-linked $Ti_3C_2T_x$ electrode for kinetic soft robotics. *Sci. Robot.* **2019**, *4*, eaaw7797.